FRIEDRICH-SCHILLER-
UNIVERSITÄT
JENA

TOWARD QUANTUM CONTROL IN DISCRETE-TIME QUANTUM WALKS

DISSERTATION

zur Erlangung des akademischen Grades

doctor rerum naturalium (Dr. rer. nat.)

vorgelegt dem Rat der

Physikalisch-Astronomischen Fakultät

der

Friedrich-Schiller-Universität Jena

von

M. Sc. Shahram Panahiyan

geboren am 12.03.1989 in Shiraz

GUTACHTER:

1. Prof. Dr. Stephan Fritzsche (Friedrich-Schiller-Universität Jena)

2. Prof. Dr. Sandro Wimberger (Università di Parma)

3. Dr. Andrea Alberti (Universität Bonn)

TAG DER DISPUTATION: 14. Juni 2021

Dedicated to my father and mother.

ABSTRACT

Discrete-time quantum walks are among the branches of quantum information and computation. They are platforms for developing quantum algorithms necessary for quantum computers. In addition, due to their universal primitive nature, discrete-time quantum walks have been used to simulate other quantum systems and phenomena that are observed in physics and chemistry. To fully utilize the potentials that the discrete-time quantum walks hold in their applications, control over the discrete-time quantum walks and their properties becomes essential.

In this dissertation, we propose two models for attaining a high level of control over the discrete-time quantum walks. In the first one, we incorporate a dynamical nature for the unitary operator performing the quantum walks. This enables us to readily control the properties of the walker and produce diverse behaviors for it. In fact, we show that with our proposal, the important properties of the discrete-time quantum walks such as variance would indeed improve.

To explore the potential of this proposal, we apply it in the simulations of topological phases that are observed in condensed matter physics. We show that with our proposal, we can control the simulations and determine the type of topological phenomena that should be simulated. In addition, we confirm the simulations of topological phases and boundary states that can be observed in one-, two- and three-dimensional systems. Finally, we also report the emergence of exotic phase structures in form of cell-like structures that contain all types of topological phases and boundary states of certain classes.

In our second proposal, we take advantage of resources available in quantum mechanics, absent in classical mechanics, namely quantum entanglement and entangled qubits. In this proposal, we use entangled qubits in the structure of a discrete-time quantum walk and show that by tuning the initial entanglement between these qubits and/or how these qubits are modified through the walk, one is able to produce diverse behaviors for the discrete-time quantum walk and control its behavior.

ZUSAMMENFASSUNG

Zeitdiskrete Quantum Walks gehören zu den Bereichen der Quanteninformation und -berechnung. Sie sind Plattformen für die Entwicklung von Quantenalgorithmen, die für Quantencomputer erforderlich sind. Aufgrund ihrer universellen primitiven Natur wurden zeitdiskrete Quantum Walks außerdem verwendet, um andere Quantensysteme und Phänomene zu simulieren, die in der Physik und Chemie beobachtet werden. Um das Potential, das die zeitdiskreten Quantum Walks in ihren Anwendungen haben, vollständig auszuschöpfen, ist die Kontrolle über die zeitdiskreten Quantum Walks und ihre Eigenschaften unerlässlich.

In dieser Dissertation schlagen wir zwei Modelle vor, um ein hohes Maß an Kontrolle über die zeitdiskreten Quantum Walks zu erreichen. Im ersten beziehen wir eine dynamische Natur für den unitären Operator ein, der die Quantum Walks durchführt. Dies ermöglicht es uns, die Eigenschaften des sogenannten Walkers leicht zu kontrollieren und verschiedene Verhaltensweisen für ihn zu erzeugen. Tatsächlich zeigen wir, dass sich mit unserem Vorschlag die wichtigen Eigenschaften der zeitdiskreten Quantum Walks wie die Varianz tatsächlich verbessern würden.

Um das Potenzial dieses Vorschlags zu untersuchen, wenden wir ihn auf die Simulation topologischer Phasen an, die in der Physik der kondensierten Materie beobachtet werden. Wir zeigen, dass wir mit unserem Vorschlag die Simulationen steuern und die Art der topologischen Phänomene bestimmen können, die simuliert werden sollen. Darüber hinaus bestätigen wir die Simulationen topologischer Phasen und Grenzzustände, die in ein-, zwei- und dreidimensionalen Systemen beobachtet werden können. Schließlich berichten wir auch über die Entstehung exotischer Phasenstrukturen in Form von zellähnlichen Strukturen, die alle Arten von topologischen Phasen und Grenzzuständen bestimmter Klassen enthalten.

In unserem zweiten Vorschlag nutzen wir die in der Quantenmechanik verfügbaren Ressourcen, die in der klassischen Mechanik fehlen, nämlich Quantenverschränkung und verschränkte Qubits. In diesem Vorschlag verwenden wir verschränkte Qubits in der Struktur eines zeitdiskreten Quantum Walks und zeigen, dass man durch Einstellen der anfänglichen Verschränkung zwischen diesen Qubits und / oder die Art wie diese Qubits während des Walks modifiziert werden, verschiedene Verhaltensweisen für den zeitdiskreten Quantum Walk erzeugen und sein Verhalten kontrollieren kann.

PUBLICATIONS

The materials presented in this thesis were contributed to the following publications:

- *Controlling quantum random walk with a step-dependent coin*
  S. Panahiyan and S. Fritzsche
  New. J. Phys. **20**, 083028 (2018).

- *Simulation of the multiphase configuration and phase transitions with quantum walks utilizing a step-dependent coin*
  S. Panahiyan and S. Fritzsche
  Phys. Rev. A **100**, 062115 (2019).

- *One-dimensional quantum walks driven by two-entangled-qubit coins*
  S. Panahiyan and S. Fritzsche
  Phys. Lett. A **384**, 126673 (2020).

- *Simulation of novel cell-like topological structures with quantum walk*
  S. Panahiyan and S. Fritzsche
  Eur. Phys. J. Plus **135**, 626 (2020).

- *Controllable simulation of topological phases and edge states with quantum walk*
  S. Panahiyan and S. Fritzsche
  Phys. Lett. A **384**, 126828 (2020).

- *Fidelity susceptibility near topological phase transitions in quantum walks*
  S. Panahiyan, W. Chen and S. Fritzsche
  Phys. Rev. B **102**, 134111 (2020).

- *Toward simulation of topological phenomena with one-, two- and three-dimensional quantum walks*
  S. Panahiyan and S. Fritzsche
  Phys. Rev. A **103**, 012201 (2021).

ACKNOWLEDGMENTS

The production of the present dissertation has become possible due to the supports that I have received over the years from different sources. First of all, I would like to express my thanks to *Prof. Dr. Stephan Fritzsche* for providing me with the possibility of working on this topic. I am also grateful for the discussions, questions, and supervision that he has provided me over the years.

I would also like to thank my colleagues in the Atomic Theory Group in Jena during my Ph.D. time as well as my friends. Specifically, I would like to thank *Dr. Birger Böning* and *Valeriia Kosheleva* for their help in proofreading the dissertation and improving it.

Finally, I would like to thank my brother, sisters, and specially my father and mother for their never-ending help and supports for as long as I have lived. The present standing of my academic career was possible only because of their attention, care, and supports.

CONTENTS

LIST OF FIGURES

LIST OF TABLES

1

INTRODUCTION

The 20th century was a booming era for new fields of science, from which we can highlight physics, information theory, and computer science. Physics was revolutionized by introductions of new branches known as quantum mechanics and general relativity. Quantum mechanics gave a counterintuitive picture regarding the mechanical behavior of quantum-like particles by using the probabilistic methods. Computer science arguably came to existence by the introduction and implementation of the Turing machine. Information theory is older than computer science, and it started to mix up with computer science in the early stage of the development of computers and networks.

The technological development of computers and computer science are based on using classical mechanics and electrodynamics. The quantum-mechanical counterparts were ignored mainly due to complexity or lack of proper machinery. The necessity for having a quantum computer was pointed out by Feynman's pioneering work on quantum computing (Feynman, 1982). In this work, he reported his observations of the simulation of quantum systems with classical computers. He concluded that simulation of the quantum-mechanical systems is rather a hard task for a classical computer. A quantum computer can provide a better platform. Following this work, in 1986, he introduced a Hamiltonian that can implement any quantum circuit (Feynman, 1985).

Feynman's paper in 1986 inspired a new line of view for applications of quantum mechanics. Instead of using quantum mechanics as a tool to describe phenomena observed in nature, one can employ its principles to design systems for specific purposes. This means that instead of looking for systems in nature, we create our quantum systems. This is the cornerstone of quantum computers and quantum technologies. Feynman's paper also motivated a series of studies into the possibility and efficiency of quantum computers and quantum information. These studies turned out to be quite fruitful. In 1997, Shor introduced a quantum algorithm for factorization which was proven to solve the problem of factorization in polynomial time (Shor, 1997). This is in contrast to any classical algorithm which takes super-

polynomial time to perform the factorization. Therefore, it is indeed crucial to have fully operational quantum computers.

Any computer has different building blocks. Algorithms are among these blocks that play central roles in the efficiency of a computer tackling a problem. In classical computers, a series of algorithms were developed using classical random walks. In brief, a classical random walk is a stochastic process that describes the random movement of a walker in a position space. In building quantum computers, it is inevitable to have quantum algorithms for performing the tasks. Otherwise, the quantum computer would not be as efficient as it is expected. The question would arise then whether we are able to find a counterpart of the classical random walk in the framework of quantum mechanics? The answer is yes.

Historically speaking, the origins of the quantum random walk are rooted in investigations of dynamics of quantum diffusion (Feynman et al., 1964). In the late 80s, Gudder, Grossing, and Zeilinger conducted a series of studies addressing the quantum dynamics via a discrete time step (Gudder, 1988; Grössing and Zeilinger, 1988). Aharonov et al. were the first ones to publish a paper titled "quantum random walk" with its main focus on the quantum random walk as an independent field of study (Aharonov et al., 1993). It took almost a decade for the community to start to take more interest in quantum random walks. The interest was sparked by a prominent work of Farhi and Gutmann which laid the foundation for continuous-time quantum walks (Farhi and Gutmann, 1998) and followed by a series of investigations by Aharonov et al. and Ambainis et al. studying discrete-time quantum random walks (Aharonov et al., 2001; Ambainis et al., 2001).

For developing algorithms with the quantum random walk, Venegas-Andraca outlined three criteria (Venegas-Andraca, 2012): I) Choosing unitary Hamiltonians or operators for both continuous- and discrete-time quantum walks to produce desirable end results on quantum hardware. II) Proper measurement mechanism and operators to find the walker's position or internal state. III) Noise or decoherence to modify and control the properties of the walker, specifically its probability density distribution. The last criterion turns out to be fatal for quantum computers and quantum computation. In fact, the noise/decoherence is one of the central obstacles to build large-scale quantum computers (Harper et al., 2020). To overcome this issue, it becomes rather crucial to find the proposals for noise-free quantum random walks that can produce diverse behaviors and one can readily modify the state of the walker with them. Motivated by this, in the present dissertation, we introduce two proposals for the discrete-time quantum random walk.

In the first proposal, we incorporate a dynamical nature for the unitary operator of the discrete-time quantum random walk. This provides us with a high level of the

control over walker's properties. The power of this proposal becomes eminent in the application of the discrete-time quantum random walk for simulating topological phases that are observed in condensed matter. In the second proposal, we introduce the discrete-time quantum random walk with entangled qubits. We show that by tuning the entanglement between the qubits and how these qubits are modified, one can steer the walker's behavior significantly. These two proposals are without any decoherence, hence providing noiseless unitary operations that are required for quantum computers.

In the next chapter, we first briefly introduce the stochastic processes and show their specific properties that make them effective platforms for modeling other systems 2.1. Next, we review the classical random walk and highlight its important features 2.2. This is necessary to contrast the classical and quantum random walks.

In Chap. 3, we present the details for the discrete-time quantum random walk in a one-dimensional position space. We show how the end results of the discrete-time quantum random walk significantly differ from its classical counterpart. To fully explore our proposal, we will investigate the applications of the discrete-time quantum random walk in simulating the topological phases observed in condensed matter. Therefore, we review how the discrete-time quantum random walks can be utilized for simulating topological phenomena.

Next, we incorporate our first proposal in the unitary operator of the discrete-time quantum random walk in Chap. 4. We confirm several issues including better variance for our proposed discrete-time quantum random walk and, diverse and controllable behaviors for our walker. This makes our proposal ideal in the context of state engineering and transfer which are crucial for quantum algorithms. Then, we apply our proposal to simulate topological phases. We confirm that our proposal can simulate different classes of topological phases that are observed in arbitrary dimensions. Due to the dynamical nature of our proposal, we are able to control the simulated topological phenomena as well. We also report on exotic phenomena such as formations of cell-like structures in phase space, multiphase configuration, and multicriticality.

Lastly, we explore our second proposal to highlight the level of control that we can wield over the walker's properties in Chap. 5. To this end, we study the long term behavior of the discrete-time quantum random walk as a function of initial entanglement between the qubits as well as how the qubits are affected by the unitary operator of the discrete-time quantum walk. We confirm that by tuning the initial entanglement between the qubits, we can control the most probable place to find the walker. In addition, we are able to produce different behaviors for the walker which brings us to our goal of finding controllable discrete-time quantum random walks.

2

RANDOM WALKS

2.1 STOCHASTIC PROCESSES

Random walks, irrespective of their types, are stochastic processes. The word *stochastic* stands for random or randomness presents in a system or phenomena. A stochastic process is a mathematical tool used to describe a random system or phenomena which probabilistically evolves in time. Therefore, a stochastic process is simply a process that develops in time according to probabilistic rules. This definition unfolds two aspects of stochastic processes:

- Our main tool in the investigation of the stochastic processes is the theory of probability, hence time-dependent probability density distributions which parametrize the likeliness of the occurrences of events in time.
- The randomness plays a central role in the process and we can attain it by undergoing the system through chance fluctuation.

In a more mathematical framework, a stochastic process is a family of random variables, $X(t), t \in T$, in which $X(t)$ measures the aspect of the system we are interested in. t is a point in space T. If $T \in [0, \infty)$, the process would be continuous. This indicates that the changes in the system occur instantly. In contrast, for $T \in \mathbb{N}$, the changes are done discretely and the process is a discrete-time stochastic process. The probability density is established by $p(x, t) = \mathrm{Prob}[X(t) = x]$ which measures the probability of $X(t)$ attaining x at time t. This probability density is called single time probability and provides the probability when there is no knowledge about the previous time.

A simple example of a stochastic process is a modification in the number of customers that are in the line to receive services in a coffee shop. In this case, $X(t)$ is the number of customers that are in the line at time t. The customers arrive and leave which results in $X(t)$ changing. The value of $X(t)$ increases by one unit due to the arrival of a customer and decreases similarly by the departure of a customer. We can observe this process continuously over time or at unit intervals, say once per hour.

To fully specify a stochastic process, we need the joint probability distributions (or the joint densities) of the random variables. The joint probability distribution is probability distributions for observations at several times $p(x_1, t_1; ...; x_n, t_n)$ which represents the probability to observe value close to $x(t_1), ..., x(t_n)$ at respective times. In the presence of the finite joint probability densities $p(x_1, t_1; ...; x_n, t_n)$ for any n, we can marginalize the joint density over one of the random variables resulting into Chapman-Kolmogorov Equation of

$$p(x_1, t_1; ...; x_{n-1}, t_{n-1}) = \int p(x_1, t_1; ...; x_n, t_n) dX_n, \tag{2.1}$$

in which for discrete variables, the integral would be replaced by a sum. Based on this definition, we can introduce characterizations of the properties to classify the stochastic processes. A stochastic process is called independent if we can characterize it by completely independent events. This indicates that for $s < t$, $X(t)$ is independent of $X(s)$. Therefore, the joint probability density will reduce to

$$p(x_1, t_1; ...; x_{n-1}, t_{n-1}) = p(x_1, t_1)p(x_2, t_2)...p(x_n, t_n). \tag{2.2}$$

Stationary stochastic processes are processes in which the probabilistic rules do not change with time. Examples of such stochastic processes are white noise and a Bernoulli scheme. For the white noise, the mean value and the variance are always fixed and independent of the time.

One of the well known stochastic processes is Markov process named after Russian probabilist Andrei Andreyevich Markov. A process called Markov if it possesses Markov property which assumes that prediction of the future requires present knowledge and it is independent of the past. In mathematical language, for an interval of $t_1 < t_1 < ... < t_n$, the conditional probability reduces to a translational probability between the last two states

$$p(x_n, t_n|x_1, t_1; ...; x_{n-1}, t_{n-1}) = p(x_n, t_n|x_{n-1}, t_{n-1}), \tag{2.3}$$

which indicates that the future (X_n) is independent of the past $(X_{n-2}, X_{n-3}, ..., X_1)$ and it can be determined only by present X_{n-1}. Consequently, we can express the joint probability density as translational probabilities with an initial probability

$$p(x_1, t_1; ...; x_{n-1}, t_{n-1}) = p(x_n, t_n|x_{n-1}, t_{n-1})...p(x_2, t_2|x_1, t_1)p(x_1, t_1). \tag{2.4}$$

The Markov property is referred to as the lack of memory property. Markov processes are much easier to analyze than general stochastic processes. In fact, in modeling by the stochastic processes, the Markov property is a common assumption.

It should be noted that although such modeling assumptions often do not hold exactly, they frequently allow a good compromise between accuracy and tractability of models.

The Markov processes have been used to predict traffic flows, communication networks, genetic issues, cellular processes at the macromolecular level, and enzyme activity. In addition, they are the basis for Markov chain Monte Carlo methods, a class of algorithms for sampling based on a specific probability distribution and Bayesian statistics. The Markov processes have been widely used in different branches of physics to model phenomena and processes.

The Markov processes classify into different sub-classes. For example, Brownian motion and the Poisson process are continuous-time Markov processes, while random walks in discrete time are discrete-time Markov processes. There is also a bigger sub-class of Markov processes known as Markov chains. Among these sub-classes, the random walks are the simplest and yet one of the most productive stochastic Markov processes in modeling other systems and phenomena including those in physics.

2.2 RANDOM WALK

Random walk is a field of study that lies in neighboring of probability, potential theory, harmonic analysis, geometry, graph theory, and algebra. Historically speaking, the term "*random walk*" was introduced by Karl Pearson, a mathematician and biostatistician, in 1905. To formally put it, a random walk is a stochastic process that resulted from the summation of independent, identically distributed random variables. To make it simpler, we consider an object that in a step moves a specific distance in a random direction. By doing the same procedure through successive equal time steps, we obtain a random walk. The dimensionality of the random walk varies from one to three. This indicates that the random walk can take place on a line, lattice, plane or graphs. We have certain flexibility regarding the movement of the walker. We can put down rules for the movement so with a probability the walker remains in its place as well.

One of the most famous examples of a two-dimensional random walk is a drunkard that wanders through pubs that are in different corners of a city. He visits a pub, gets drunk and then decides to go to another pub. Since he has no preferences for the next pub, he would randomly choose between the pubs that are the closest to him. After finishing in the second pub, he goes to another one which could be the previous pub or a new one that is the closest to him. Therefore, our drunkard moves

around in a two-dimensional plane, preferably a square one. It should be noted that our drunkard could go back to the same pub and drink again, given his condition of drunkenness.

Random walks are rather simple and easy to analyze by mathematical methods. They are Markov processes and could be Markov chains as well. They are non-stationary stochastic processes. They have been excessively used in ecology, psychology, computer science, physics, chemistry, biology, economics and sociology for applications such as the development of stochastic algorithms, image segmentation, modeling earthquake, genomic distance from DNA sequence location, and enzymes. Like all other stochastic processes, random walks can be categorized into continuous-time and discrete-time random walks.

The walker in a random walk can be any kind of object ranging to subatomic particles. This indicates the existence of two distinct branches of the random walks based on two branches of physics describing the motion of an object (classical and quantum mechanics). Therefore, we have two types of random walks labeled by classical random walk and quantum random walk. In what follows, we briefly introduce the discrete-time classical random walk and its properties. Then we move on to the discrete-time quantum random walk and describe it. From now onwards, we omit the *discrete-time random* from our notations for the sake of brevity unless it is necessary.

The classical walk is the most studied and investigated branches of the random walks. In the classical walk, the rules governing the movement of the objects come from classical mechanics. The walk can be done in different environments including graphs, on a real line, in a plane, higher-dimensional vector spaces, and on curved surfaces or higher-dimensional Riemannian manifolds. The example of the drunkard that we gave previously is a classical walk on a two-dimensional plane.

The simplest example of a classical walk is a walk on a one-dimensional lattice. Assume that we are standing in the middle of this lattice and consider our standing point as the origin. We take out a coin and toss it. If the result of the coin toss is head, then we move one lattice to the right. If the result is tail, we move one unit to the left. We repeat the same process of coin tossing and moving for an arbitrary but fixed number of times and then we mark the place that we are at the end. This is the simplest and yet one of the strongest examples of the classical walk. The coin toss provides us with randomness in the classical walk and our movement is a conditional one determined by the result of the coin toss. The type of the walk is indeed discrete-time and unbiased since there is a fifty-fifty chance for the result of the coin toss.

To put in a more mathematical framework, the classical walk includes a single

walker that moves along an axis with unit steps at a unit interval. The probabilities of the movement to the right- and left-hand sides are given by N and $1-N$, respectively. If the walker start from the origin, we obtain the probability of finding the walker at position k after T times step as

$$p(x=k,T)=\begin{cases}\binom{T}{\frac{1}{2}(k+T)}N^{\frac{1}{2}(k+T)}(1-N)^{\frac{1}{2}(k+T)}, & \frac{1}{2}(k+T)\in\mathbb{N}\cup 0\\ 0 & \text{otherwise}\end{cases}, \tag{2.5}$$

which is a binomial distribution (see Fig. 2.1). If we remove the positions with zero probability densities, the resultant probability density distribution would be a Gaussian distribution. It should be noted that the Gaussian stems from a limiting process starting from binomial. It is straightforward to find the variance of the walker's probability density distribution as

$$\sigma^2=O(T), \tag{2.6}$$

which indicates that the variance of the classical walk grows linearly over time, therefore the classical walk is diffusive.

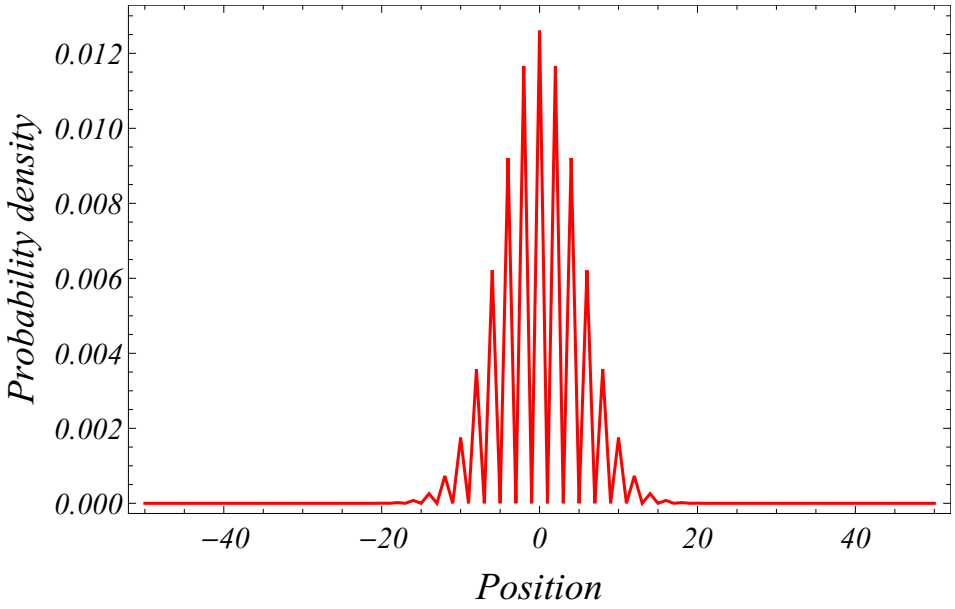

Figure 2.1: Probability density distribution of the classical walk after 50 steps. If we remove the positions with zero probability densities, we have a Gaussian probability density distribution for the classical walk.

To find the results of our earlier example regarding the coin toss and moving on a line, we should set $N=\frac{1}{2}$ in (2.5) giving us the probability density distribution as

$$p(x=k,T)=\begin{cases}\binom{T}{\frac{1}{2}(k+T)}\frac{1}{2^T}, & \frac{1}{2}(k+T)\in\mathbb{N}\cup 0\\ 0 & otherwise\end{cases}, \tag{2.7}$$

which by using the Stirling's approximation ($T!\approx\sqrt{2\pi T}(\frac{T}{e})^T$), we can find

$$p(x=k,T)\approx\sqrt{\frac{2T}{\pi^2(T^2-k^2)}}\frac{T^T}{(T+k)^{\frac{T+k}{2}}(T-k)^{\frac{T-k}{2}}}. \tag{2.8}$$

Here, it is useful to define hitting time as a means to better understand the properties of the classical walk and make a contrast between the classical and quantum walks. The hitting time denotes the expected number of steps that takes to reach lattice j starting from lattice i. The expected hitting time is found by inverting the probability density distribution.

For the unbiased classical walk, since the shape of the probability density distribution is Gaussian and the walk is diffusive, we consider two specific limits to investigate hitting time. The case $k\ll T$ corresponds to the region under the bell-shape part of the distribution. The case $k\approx T$ consists of the regions along the tails of the distribution. For the first case, the probability density distribution reduces to

$$p(x=k,T)\approx\sqrt{\frac{2}{\pi^2 T}}, \tag{2.9}$$

which indicates that the hitting time would be the square root of the step number, hence time. In contrast, for the second case, the probability density distribution yields

$$p(x=k,T)\approx\frac{1}{2^T}\sqrt{\frac{2T}{\pi(T^2-k^2)(T-k)^{T-k}}}, \tag{2.10}$$

in which T^2-k^2 and $T-k$ are small numbers and since 2^T grows faster than $\sqrt{T}$, we can conclude that the hitting time for this case would be exponential. The end results indicate that if the lattice is placed under the bell-shaped part of the distribution, it takes $\sqrt{T}$ number of steps to reach it from the origin whereas if the lattice is placed at the tail of the distribution, it takes 2^T number of steps to reach it. In summary, we find the followings for our unbiased one-dimensional classical walk:

- The probability density distribution of the classical walk on a one-dimensional lattice is binomial or Gaussian.

- The behavior of the walker is diffusive, indicating that the square of the variance of the classical walk grows over time linearly.
- It takes $\sqrt{T}$ to reach a lattice provided the lattice is the under bell-shape of the distribution.

The generalization to higher dimensions is a straightforward work. It is also possible to change from discrete-time to continuous-time classical walk. In fact, by such a simple setup and generalization of the walk to three-dimensional position space or other platforms, the cornerstone for developing algorithms based on the classical walk was obtained. From then on, the classical walk has been used for the introduction of algorithms for image segmentation and developing algorithms to uncover various types of structural properties of networks. Of other applications of the classical walk, we can point out to locomotion and foraging of animals (Viswanathan et al., 1999; Codling et al., 2008), decision-making in the brain (Gold and Shadlen, 2007), polymer chains (Fisher, 1966), the evolution of research interests (Jia et al., 2017), dimension reduction and feature extraction from high-dimensional data (Coifman et al., 2005), and even sports statistics (Clauset et al., 2015).

The algorithms developed by classical walks are used in classical computers, computations, and information. Recent years witnessed the emergence of similar fields of studies that instead use the principals of quantum mechanics as their building blocks. The hint was given by Feynman in one of his seminal works in 1986 in which he proposed a Hamiltonian that can implement any quantum circuit (Feynman, 1985). This resulted in the fields that we know as quantum computation, communication, networks, information, and so on. The development of quantum computers is one of the milestones that has been pursued by these fields. And for any computer to work properly, we need algorithms and for quantum computers, we need quantum algorithms. Therefore, it is natural and straightforward to try and find the quantum counterparts of the classical walks and use them similarly to develop algorithms required for quantum computers.

3

THE DISCRETE-TIME QUANTUM WALK

3.1 ONE-DIMENSIONAL QUANTUM WALK

In nutshell, the quantum walk is the counterpart of the classical walk. This indicates that the walker is no longer a classical object rather a quantum-like one and the laws governing the walker's movement are dictated by principles of quantum mechanics. This definition gives three guidelines regarding quantum walks:

- The movement of the walker and the chance fluctuations required for randomness must be attained through quantum operators that are applied on the walker.

- In the quantum walk, contrary to the classical walk, one can not make measurements at each step. This is due to the principles of quantum mechanics which state upon the action of measurement, the wave function of the system collapses. Therefore, the integrity of the system as a quantum walker would be eliminated upon measurement and it is not possible to continue the walk.

- Quantum mechanics offers specific features that are absent in the classical systems. The most well known of these features is entanglement. In fact, we take advantage of the entanglement as a resource to produce significantly diverse properties for the quantum walk comparing to its classical counterpart. In addition, we use the superposition as an additional feature offered in the quantum walk to introduce novel properties that are absent in the classical walk.

The walker in the quantum walk could be neutral atoms (Karski et al., 2009), ions (Schmitz et al., 2009; Zähringer et al., 2010), photons (Schreiber et al., 2010; Bian et al., 2015; Barkhofen et al., 2018), Bose-Einstein condensation (Dadras et al., 2018), optical networks (Lorz et al., 2019) and etc. The quantum walk can be also implemented in electric (Genske et al., 2013) or magnetic fields (Sajid et al., 2019). Similar to the

classical walk, we have two types of continuous-time and discrete-time quantum walk. In what follows, we briefly talk about a one-dimensional quantum walk with two integral states.

3.1.1 *Theory*

The discrete-time quantum walk is the most studied model of the quantum walks. In the discrete-time quantum walk, the total Hilbert space of the walk consists of two sub-spaces ($\mathcal{H} = \mathcal{H}_P \otimes \mathcal{H}_C$). One of these sub-spaces is originated from the internal degrees of freedom of the walker. This sub-space is also known as coin space or internal states ($\mathcal{H}_C$). The other sub-space is the external degrees of freedom of the walker and is usually known as the position space ($\mathcal{H}_P$). Correspondingly, the evolution operator of the discrete-time quantum walk includes two operators:

- The coin operators which are explicitly applied on internal states of the walker. The application of the coin operators usually creates a superposition of the internal states. In fact, this superposition is one of the fundamental principles that diversifies the discrete-time quantum walk from its classical counterpart.
- The shift operators which displace the walker in position space. The shift operators are conditionalized based on the internal states of the walker. To put it simply, the shift operators move the walker according to its internal states. And due to the application of the coin operators and superposition of the internal states, the displacements of shift operators could amplify or reduce the probability of finding the walker in different positions at each step.

Chronologically, first a coin operator is applied on the walker and then followed by a shift operator. One time application of the evolution operator on the walker is one step of the walk and the generation of the quantum walk is the result of the successive application of the evolution operator for T times step on an initial state of the walker.

The evolution operator is also known as the protocol of the quantum walk. The numbers of coin and shift operators determine the type of protocol. In literature, two types of protocols have been used for the quantum walk (Kitagawa et al., 2010): I) Simple-step which has one coin and one shift operator (shift-coin), II) Split-step which consists of at least two different coin and two different shift operators (shift-coin-shift-coin).

To provide contrasts between the classical walk and quantum walk, we construct the coin toss and movement of the classical walk described in the previous section,

in the framework of the quantum walk. To do so, we should translate the operation in the classical system to its quantum counterpart. The walker in such a translation would be a quantum-like particle that has two internal states. This indicates that coin space is a two-dimensional Hilbert space spanned by $\{|\uparrow\rangle, |\downarrow\rangle\}$ in which

$$|\uparrow\rangle = \begin{pmatrix} 1 \\ 0 \end{pmatrix}, \quad |\downarrow\rangle = \begin{pmatrix} 0 \\ 1 \end{pmatrix}. \tag{3.1}$$

The walker has a one-dimensional position space as the external degree of freedom. Such a Hilbert space is spanned by $\{|x\rangle : x \in \mathbb{Z}\}$. In general, the walker is described by a wave function containing the combination of internal and external degrees of freedom. Next, we need proper translations for the coin toss and movement of the walker from classical mechanics to quantum mechanics. The coin toss in the classical walk is translated to a coin operator in quantum mechanics ($\widehat{C}$) which is a rotation matrix. Since we are interested to replicate the coin toss in the classical walk, we choose the coin operator as

$$\widehat{C} = \frac{1}{\sqrt{2}} \begin{pmatrix} 1 & 1 \\ 1 & -1 \end{pmatrix}, \tag{3.2}$$

which is the famous Hadamard gate. The application of the Hadamard gate on the two internal states results in

$$\widehat{C}\,|\uparrow\rangle = \frac{1}{\sqrt{2}}(|\uparrow\rangle + |\downarrow\rangle), \qquad \widehat{C}\,|\downarrow\rangle = \frac{1}{\sqrt{2}}(|\uparrow\rangle - |\downarrow\rangle), \tag{3.3}$$

which creates a superposition of the internal states with equal probabilities, hence replicating the coin toss of the classical walk. The displacement of the walker in the quantum walk is depicted by a conditional shift operator given by

$$\widehat{S}_{\uparrow\downarrow}(x) = |\uparrow\rangle\langle\uparrow| \otimes \sum_x |x+1\rangle\langle x| + |\downarrow\rangle\langle\downarrow| \otimes \sum_x |x-1\rangle\langle x|. \tag{3.4}$$

Depending on the internal states present in the state of the walker, the shift operator displaces the walker one unit to the right or left in position space. The evolution operator of the walk is then formulated by

$$\widehat{U} = \widehat{S}_{\uparrow\downarrow}(x)\widehat{C}, \tag{3.5}$$

and the final state of the walker is obtained if we apply T times this evolution operator on an initial state

$$|\psi\rangle_T = \widehat{U}^T |\psi\rangle_{ini.} = (\widehat{S}_{\uparrow\downarrow}(x)\widehat{C})^T |\psi\rangle_{ini.} . \tag{3.6}$$

One of the main differences between the classical walk and quantum walk is the dependency of the quantum walk on its initial state. Here, we consider three specific initial states for the walker

$$|\psi\rangle_{ini.} = |0,\uparrow\rangle , \tag{3.7}$$

$$|\psi\rangle_{ini.} = |0,\downarrow\rangle , \tag{3.8}$$

$$|\psi\rangle_{ini.} = \frac{1}{\sqrt{2}}(|0,\uparrow\rangle + |0,\downarrow\rangle), \tag{3.9}$$

where in the last one, we have used the principle of the superposition in quantum mechanics.

The end product of the quantum walk is a wave function. Similar to the classical walk, any calculation regarding the observables of this wave function would give us the probability of finding that observable. The observables in the quantum walk are two items: the position of the walker and its internal state. This indicates that if we want to find, for example, the probability of finding the walker in position x, we should project the walker's wave function to a state in position x and sum over all the internal states. The same can be done for the internal states as observables. In either case, since there is no decoherence in our system (pure final state), the sum over the probabilities of positions or internal states equals the unit.

The probability density distributions in position space for the initial states of Eqs. (3.7) and (3.8) are plotted in Fig. 3.1 with $T = 50$. In the context of probability density distribution in position space, we observe significantly different behavior for the quantum walk comparing to its classical counterpart. The symmetry of the distribution depends on the internal states considered in the initial state. The symmetrical distribution is resulted if the initial state contains the superposition of both internal states with equal probability densities. Otherwise, the distribution would be asymmetrical. While the classical walk has the Gaussian (binomial) probability density distribution, the quantum walk shows skewness feature for its probability density distribution. This indicates that in the classical walk, the walker is more likely to be found in its initial position, whereas in the quantum walk, the most probable place to find the walker step-dependently moves away from the initial position. This is rooted in the entanglement between the two sub-spaces of the walk and quantum interference due to the application of the shift-coin operator. That being said, in the initial position and around it, we observe a quasi-uniform behavior in the probability

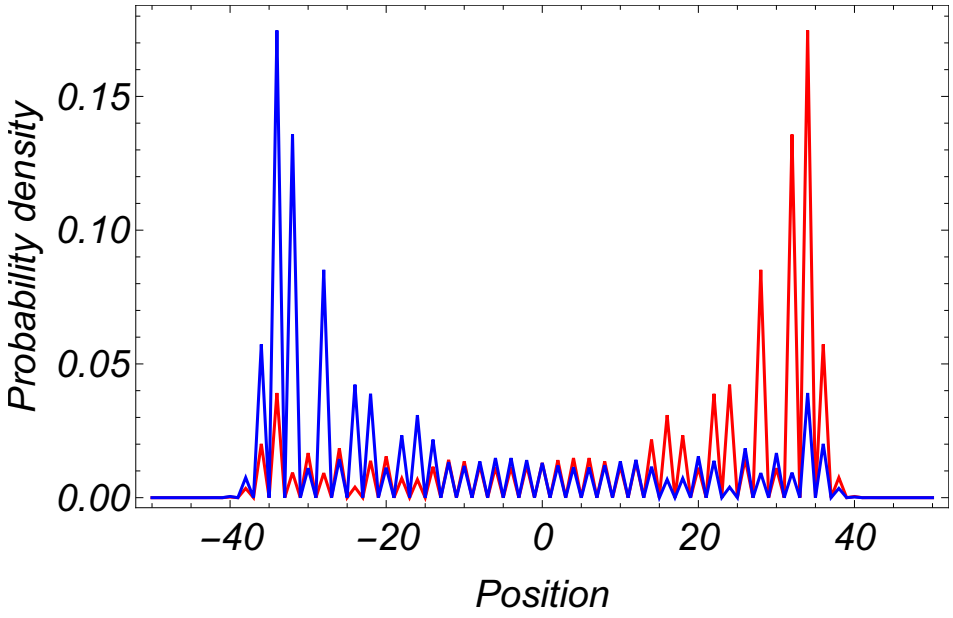

Figure 3.1: Probability density distributions of the quantum walks with the two initial states of (3.7) (red line) and (3.8) (blue line) for $T = 50$.

density distribution of the quantum walk. Finally and most importantly, the variance of the quantum walk can be estimated to

$$\sigma^2 = O(T^2), \tag{3.10}$$

which shows that the quantum walk has ballistic behavior and it reaches to certain point quadratically faster comparing to the classical walk (compare (3.10) with (2.6)). Therefore, the quantum walk has ballistic spread in its wave function comparing to the diffusive behavior of the classical walk. This is the cornerstone of the proposal that algorithms such as search algorithms developed using quantum walks can efficiently outperform their classical counterparts.

3.1.2 *Analytical description of the walk*

To study the asymptotic behavior of the quantum walk analytically, several methods have been developed. Among them, we can highlight two specific methods that are widely used: I) Combinatorial approach in which the amplitudes of a specific position are obtained by summing up the amplitudes of all the paths which start from the initial position and end up to that position. II) Schröodinger approach which Fourier transforms the spatial part of the wave function of the walker at a specific step and uses complex analysis to obtain the amplitudes at each position and internal state. This method was first used for the quantum walk by Ashwin Nayak

and Ashvin Vishwanath (Nayak and Vishwanath, 2000). In this dissertation, we use the latter method since the Fourier transformation also serves as a tool to use the quantum walk for simulation of the topological phases observed in condensed matter physics (Kitagawa et al., 2010).

Since our walker has two internal states, we can write the wave function of the walker as two-component vector amplitudes in the form of

$$|\psi(x)\rangle_T = \psi_\uparrow(x,T)\,|\uparrow\rangle + \psi_\downarrow(x,T)\,|\downarrow\rangle\,, \tag{3.11}$$

in which for the next step of the walk, the wave function of the walker at position x can be written as

$$\begin{aligned} |\psi(x)\rangle_{T+1} &= \begin{pmatrix} 0 & 0 \\ \frac{1}{\sqrt{2}} & -\frac{1}{\sqrt{2}} \end{pmatrix} |\psi(x-1)\rangle_T + \begin{pmatrix} \frac{1}{\sqrt{2}} & \frac{1}{\sqrt{2}} \\ 0 & 0 \end{pmatrix} |\psi(x+1)\rangle_T \\ &= M_+\,|\psi(x+1)\rangle_T + M_-\,|\psi(x-1)\rangle_T\,. \end{aligned} \tag{3.12}$$

The quantum walk described above has translational invariance which enables us to use the Fourier transformation and complex analysis to study its behavior and properties. The spatial Fourier transformation is given by

$$|k_x\rangle = \sum_x e^{ik_x x}\,|x\rangle\,, \tag{3.13}$$

which indicates that the wave function of the walker in the momentum space at step T can be obtained by

$$|\psi(k_x)\rangle_T = \sum_x e^{ik_x x}\,|\psi(x)\rangle_T\,. \tag{3.14}$$

This gives us the wave function of the walker at $T+1$ as

$$\begin{aligned} |\psi(k_x)\rangle_{T+1} &= \sum_x (M_+\,|\psi(x+1)\rangle_T + M_-\,|\psi(x-1)\rangle_T)e^{ik_x x} \\ &= (e^{ik_x}M_+ + e^{-ik_x}M_-)\,|\psi(k_x)\rangle_T = M\,|\psi(k_x)\rangle_T\,. \end{aligned} \tag{3.15}$$

The result enables us to have the mapping of $|\psi(k_x)\rangle_T = M^T\,|\psi(k_x)\rangle_0$ which reduces the problem to find M^T. To do so, we use the unitary nature of the M. According to principles of quantum mechanics, if M is unitary, we can calculate M^T by diagonalizing M and expressing it in terms of its eigenvalues and eigenstates. Since our operator is 2×2 and unitary, it is diagonalized. M can be rewritten as

$$M = \lambda_1\,|\phi\rangle_1\,\langle\phi|_1 + \lambda_2\,|\phi\rangle_2\,\langle\phi|_2\,, \tag{3.16}$$

where $|\phi\rangle_i$ and λ_i are eigenstates and eigenvalues of M, respectively and M^T is

$$M^T = \lambda_1^T |\phi\rangle_1 \langle\phi|_1 + \lambda_2^T |\phi\rangle_2 \langle\phi|_2 . \tag{3.17}$$

For the quantum walk with Hadamard gate and initial state of $|\psi(k_x)\rangle_0 = \begin{pmatrix} 1 \\ 0 \end{pmatrix}$, the eigenvalues of M are $\lambda_1 = e^{-i\omega_{k_x}}$ and $\lambda_1 = e^{i(\omega_{k_x}+\pi)}$ in which $\sin(\omega_{k_x}) = \frac{\sin(k_x)}{\sqrt{2}}$ and $\omega_{k_x} \in [-\frac{\pi}{2}, \frac{\pi}{2}]$. On the other hand, the eigenstates are obtained as

$$|\phi\rangle_1 = \frac{\begin{pmatrix} e^{-ik_x} \\ \sqrt{2}e^{-i\omega_{k_x}} - e^{-ik_x} \end{pmatrix}}{\sqrt{2(1+\cos^2(k_x)) - 2\cos(k_x)\sqrt{1+\cos^2(k_x)}}}, \tag{3.18}$$

$$|\phi\rangle_2 = \frac{\begin{pmatrix} e^{-ik_x} \\ -\sqrt{2}e^{i\omega_{k_x}} - e^{-ik_x} \end{pmatrix}}{\sqrt{2(1+\cos^2(k_x)) - 2\cos(k_x)\sqrt{1+\cos^2(k_x)}}}. \tag{3.19}$$

The results should be transformed back into real space. To do so, we use the following relation

$$|x\rangle = \frac{1}{2\pi}\int_{-\pi}^{\pi} e^{-ik_x x} |k_x\rangle \, dk_x, \tag{3.20}$$

which gives us

$$\psi_\uparrow(x,T) = \frac{1+(-1)^{x+T}}{2}\int_{-\pi}^{\pi}(1+\frac{\cos(k_x)}{\sqrt{1+\cos^2(k_x)}})e^{-i(\omega_k T + k_x X)}\frac{dk_x}{2\pi}, \tag{3.21}$$

$$\psi_\downarrow(x,T) = \frac{1+(-1)^{x+T}}{2}\int_{-\pi}^{\pi}\frac{e^{ik_x}}{\sqrt{1+\cos^2(k_x)}}e^{-i(\omega_k T + k_x X)}\frac{dk_x}{2\pi}. \tag{3.22}$$

The first consequence of the obtained results is the dependency of the amplitudes on the parity as it was observed. In other words, the amplitudes of the even positions at odd steps are zero and vice versa. The probability density of the position x at step T is found by $P(x,T) = |\psi_\uparrow(x,T)|^2 + |\psi_\downarrow(x,T)|^2$. To find the asymptotic properties of the wave function for large T, we use the method of the stationary phases developed in complex analysis (see appendix 7.1 for more details) which leads to

$$\psi_\uparrow(\alpha T, T) \sim \frac{1+(-1)^{(\alpha+1)T}}{\sqrt{2\pi T|\omega''_{k_\alpha}|}}(1-\alpha)\cos(\phi(k_\alpha,\alpha)T + \frac{\pi}{4}), \tag{3.23}$$

$$\psi_{\downarrow}(\alpha T, T) \sim \frac{1+(-1)^{(\alpha+1)T}}{\sqrt{2\pi T|\omega''_{k_\alpha}|}}\alpha\cos(\phi(k_\alpha,\alpha)T+\frac{\pi}{4})- \sqrt{1-\alpha^2}\sin(\phi(k_\alpha,\alpha)T+\frac{\pi}{4}), \tag{3.24}$$

in which α is limited to $[-1,1]$ and is a stationary point, $\phi(k_\alpha,\alpha)$ is given in (7.4). It is a matter of the calculation to find the probability density as

$$P(\alpha T,T)\sim\frac{1+(-1)^{(\alpha+1)T}}{\pi T|\omega''_{k_\alpha}|}(1-\alpha^2)\Big(\cos^2(\phi(k_\alpha,\alpha)T+\frac{\pi}{4})+\cos^2(\phi(k_\alpha,\alpha)T+\frac{\pi}{4},k_\alpha)\Big).$$

3.2 APPLICATIONS

The discrete-time quantum walk on its own is an interesting field of study since it provides an easy empirical method for implementation and testing of the quantum mechanics' principles. On the other hand, the quantum walk has been used for simulations of quantum phenomena observed in physics (Vakulchyk et al., 2019) and chemistry (Mohseni et al., 2008) as well as the development of quantum algorithms. In this section, we briefly review some of these applications.

3.2.1 *Quantum search algorithm*

Originally, the initial interest in the quantum walk was due to its possible applications in developing algorithms for quantum computers. This is stemmed from the development of efficient stochastic algorithms using the classical walk.

One of the first algorithms based on the quantum walk was introduced by Shenvi et al. as a search algorithm on a n-dimensional hypercube (Shenvi et al., 2003). The cube has 2^n nodes and each node is connected to n other nodes. The Hilbert space of the such system (the algorithm) is $\mathcal{H}=\mathcal{H}^n\otimes\mathcal{H}^{2^n}$. In such a Hilbert space, each state is characterized by a bit string ($\overrightarrow{x}$) and a direction ($\overrightarrow{d}$) which are the position on hypercube and internal state, respectively. The shift operator changes the bit string to $\overrightarrow{x}\oplus\overrightarrow{e_d}$. The coin operator is a $n\times n$ unitary operator which is built out of Grover diffusion operator and an identity operator. Shenvi et al. showed that a search with their proposed algorithm takes $T=\frac{\pi}{2}\sqrt{2^n}$ steps to complete which comparing to any classical algorithm (with the completion time of $T=2^n$), is quadratically faster.

Another quantum walk algorithm was proposed by Ambainis for element distinctness (Ambainis, 2004). This algorithm is also a search algorithm in which two

equal items among N items are found. The generalization of element distinctness algorithm addresses k equal items among N items. Aaronson and Shi showed that there is a lower bound for quantum algorithms developed for element distinctness which indicates that the quantum algorithm requires at least $O(N^{\frac{2}{3}})$ quantum queries (Aaronson and Shi, 2004). Buhrman et al. developed a quantum algorithm for element distinctness which violates the lower bound (Buhrman et al., 2005). In contrast, Ambainis' algorithm based on the quantum walk is an $O(N^{\frac{2}{3}})$ query quantum algorithm which improves the results. For the generalized element distinctness case, Ambainis' algorithm gives the result in order of $O(N^{\frac{k}{k+1}})$ which meets the lower bound criteria.

Except for the two cases pointed out here, there are several references that studied the algorithm application of the quantum walk. For instance, Magniez et al. presented an algorithm to detect marked elements (Magniez et al., 2007). Paparo and Martin-Delgado developed a quantum-mechanical version of Google's PageRank algorithm (Paparo and Martin-Delgado, 2012). Sampling via the quantum walk is yet another application of the quantum walk in the direction of developing algorithms and it was shown that decoherent in the quantum walk can be used as a means to achieve speedup (Richter, 2007). In ref. (Rohde et al., 2012), data security in the quantum network and computation using a quantum walk is discussed. It was shown that by the boson sampling and multiwalker quantum walk, it is possible to have a limited quantum homomorphic encryption.

3.2.2 *Universal computational primitive*

Child proved that the continuous-time quantum walk can be utilized as a universal computational tool (Childs, 2009). Later on, Lovett et al. applied the same idea for the discrete-time quantum walk (Lovett et al., 2010). In their proposal, they constructed a universal gate using the discrete-time quantum walk on a graph. The universal gate was built by a combination of phase and Hadamard gates. In their scheme, the quantum wires played the role of a quantum state. They showed that using their scheme, it is possible to have perfect state transfer. The end results indicate that the discrete-time quantum walk is indeed a universal primitive.

The universality points out to capability of simulating other phenomena and systems. This means that discrete-time quantum walks can be used as platforms to simulate other quantum systems and phenomena that are observed in different branches of science. This is highly a desirable feature for any protocol of quantum information and computation. In fact, this brings us to the question of what systems

can be simulated with discrete-time quantum walks? and how we can do so? Simulation of the topological phases observed in condensed matter is one of the manifestations of the universality of the discrete-quantum walks and answers this question.

3.2.3 *Simulation of the topological phases*

Recently, the quantum walk has been used as a simulator of the topological phases and boundary states that are observed and studied in condensed matter physics (Kitagawa et al., 2010; Kitagawa, 2012; Asbóth, 2012; Asbóth and Obuse, 2013; Tarasinski et al., 2014; Rakovszky and Asboth, 2015; Obuse et al., 2015; Ramasesh et al., 2017; Chen et al., 2018). In a pioneering work, Kitagawa et al. proposed a series of protocols for the quantum walk that could simulate all types of one- and two-dimensional topological phases that are observed in condensed matter (Kitagawa et al., 2010). Their inspiration was due to the similarity of Su-Schrieffer-Heeger (SSH) model of polyacetylene and quantum walks. In what follows, we briefly review general details concerning the topological phases. Then, we describe the SSH model, and afterward, we study the simulation of BDI class of topological phases with quantum walks.

Topological phases

Materials in nature are observed in different phases. A profound yet simple example of different phases of a matter is water in three forms (phases) of crystal, liquid, and vapor. The word "phase" refers to how the particles of a material are organized. Various properties of materials are originated from the type of organization which is called order. Therefore, different phases of the materials are recognized by different orders.

Landau developed the theory underlining different phases of matter based on their orders and phase transitions between them (Landau, 1937). His theory categorizes different phases of the materials based on the symmetries that are present in them and recognizes phase transitions as points where certain symmetries are broken/gained. To put it simply, the reason that we see different forms of the water is because of the presence or absence of a certain set of symmetries in that phase. The transition from one phase to another one is simply a symmetry or symmetries break(s) or emerge(s).

In the example of the water, in the crystal form, rotational and translational symmetries are absent while discrete symmetries are present. In the liquid form though, the rotational and translational symmetries are present. Therefore, at the phase transition

point where the liquid turns into the crystal, rotational and translational symmetries are broken. Another example of the different phases is ferromagnetic materials in which at a specific temperature, the global rotational symmetry would be broken and we would have magnets.

Landau's symmetry-breaking theory of the phases enables us to obtain the critical properties of the materials in their phase transition points. This theory has been the cornerstone of condensed matter physics. Despite its success, the discoveries of the fractional Hall effect (Tsui et al., 1982) and superconductors (Tsui et al., 1982) in the 1980s challenged the wholesomeness of Landau's paradigm. The existence of such phases is not predicted or allowed in Landau's theory. In fact, in the phase transition points for these materials, no symmetry is broken (Thouless et al., 1982; Bernevig et al., 2006; König et al., 2007; Fu and Kane, 2007; Qi et al., 2008; Fidkowski and Kitaev, 2011). These symmetry-preserving materials can be categorized by a global order which is known as the topological invariant (Hasan and Kane, 2010).

The topological invariant characterizes the global structure of the ground-state wave function of symmetry-preserving materials. In contrast to symmetry-breaking materials, the global order does not change continuously. The phase transition point in symmetry-preserving materials is recognized by a sudden change in topological invariant. The physical manifestation of the topological invariant varies from one material to another one. For example, the quantized Hall conductance in two dimensions is characterized by a topological invariant known as Chern number (Thouless et al., 1982; Niu et al., 1985). In one-dimensional superconductors, the presence of the Majorana fermions at the ends of the wire corresponds to the topological invariant (Kitaev, 2001; Lutchyn et al., 2010).

Different classes of the topological phases are defined based on two factors: dimensionality of the system under consideration and the symmetries that are present (Schnyder et al., 2008; Ryu et al., 2010; Kitaev, 2009; Chiu et al., 2016). The symmetries that we are concerned with are the time-reversal (TRS), particle-hole (PHS), and chiral (CHS) with their corresponding operators of $\widehat{\mathcal{T}}$, $\widehat{\mathcal{P}}$ and $\widehat{\Gamma}$, respectively. The presence of these symmetries are conditioned to

$$\widehat{\mathcal{P}}\widehat{H}\widehat{\mathcal{P}}^{-1} = -\widehat{H}, \tag{3.25}$$

$$\widehat{\Gamma}^{-1}\widehat{H}\widehat{\Gamma} = -\widehat{H}, \tag{3.26}$$

$$\widehat{\mathcal{T}}\widehat{H}\widehat{\mathcal{T}}^{-1} = \widehat{H}, \tag{3.27}$$

in which $\widehat{H}$ is the Hamiltonian. $\widehat{\mathcal{P}}$ and $\widehat{\mathcal{T}}$ are antiunitary operators, while $\widehat{\Gamma}$ is a unitary one. The square of the TRS and PHS could yield $\widehat{\mathcal{P}}^2 = \pm\widehat{I}$ and $\widehat{\mathcal{T}}^2 = \pm\widehat{I}$ whereas, for the CHS operator, we have $\widehat{\Gamma}^2 = \widehat{I}$. The presences of two of these symmetries

Topological Class	Symmetry $\widehat{\mathcal{P}}$	Symmetry $\widehat{\mathcal{T}}$	Symmetry $\widehat{\Gamma}$	Dimension 1D	Dimension 2D	Dimension 3D
A	0	0	0	0	$\mathbb{Z}$	0
AI	0	$+\widehat{\mathrm{I}}$	0	0	0	0
AII	0	$-\widehat{\mathrm{I}}$	0	0	$\mathbb{Z}_2$	$\mathbb{Z}_2$
AIII	0	0	$+\widehat{\mathrm{I}}$	$\mathbb{Z}$	0	$\mathbb{Z}$
BDI	$+\widehat{\mathrm{I}}$	$+\widehat{\mathrm{I}}$	$+\widehat{\mathrm{I}}$	$\mathbb{Z}$	0	0
C	$-\widehat{\mathrm{I}}$	0	0	0	$\mathbb{Z}$	0
CI	$-\widehat{\mathrm{I}}$	$+\widehat{\mathrm{I}}$	$+\widehat{\mathrm{I}}$	0	0	$\mathbb{Z}$
CII	$-\widehat{\mathrm{I}}$	$-\widehat{\mathrm{I}}$	$+\widehat{\mathrm{I}}$	$\mathbb{Z}$	0	$\mathbb{Z}_2$
D	$+\widehat{\mathrm{I}}$	0	0	$\mathbb{Z}_2$	$\mathbb{Z}$	0
DIII	$-\widehat{\mathrm{I}}$	$+\widehat{\mathrm{I}}$	$+\widehat{\mathrm{I}}$	$\mathbb{Z}_2$	$\mathbb{Z}_2$	$\mathbb{Z}$

Table 3.1: Different classes of topological phases observed in one (1D), two (2D), and three dimensions (3D). The presence of a symmetry is depicted by $\pm\widehat{\mathrm{I}}$ while the absence is given by 0. $+\widehat{\mathrm{I}}$ and $-\widehat{\mathrm{I}}$ specify whether the symmetry operator squares to $+\widehat{\mathrm{I}}$ and $-\widehat{\mathrm{I}}$ (e. g. $\widehat{\mathcal{P}}^2 = +\widehat{\mathrm{I}}$ or $-\widehat{\mathrm{I}}$). The class of the topological phases is determined by the dimensionality, available symmetries, and corresponding topological invariant which could be an integer, $\mathbb{Z}$, or a binary $\mathbb{Z}_2$.

guarantee the existence of the third one. For each class of the topological phases, the topological invariant and its value would be different. Table 3.1 gives a compact classification of topological phases based on the dimensionality, symmetries, and the square of the symmetries' operators.

Topological phases and Su-Schrieffer-Heeger model

The SSH model belongs to the one-dimensional BDI class of the topological phases. This model addresses the conductivity and insulation in terms of spinless fermions hopping on a one-dimensional lattice with staggered hopping amplitudes. A physical example of the materials described by the SSH model is polyacetylene molecules which are organic materials that could show conductivity and insulation properties.

The SSH model considers the electrons or fermions being spinless and located in or around the ground state at zero temperature and chemical potential. For a chain of polyacetylene molecules, we divide them into N unit cells each containing two carbons. Each of these two carbons belongs to two sub-lattices of A and B. The sub-lattices play the role of spin for us. Due to the absence of the onsite potential terms, each carbon provides one conducting electron. The interactions between the

electrons are neglected. The dynamic of each electron is described by the following Hamiltonian (Su et al., 1979)

$$\widehat{H} = v\sum_{m=1}^{N}(|m,B\rangle\langle m,A| + h.c) + w\sum_{m=1}^{N-1}(|m+1,A\rangle\langle m,B| + h.c), \tag{3.28}$$

in which h.c is Hermitian Conjugate, v and w are real and positive hopping amplitudes. The chain of the molecules has two ends which are known as "edges" and the rest of the chain is called "bulk". For now, we are mainly interested in the bulk part of the chain, as well as eigenstates and eigen energies of the Hamiltonian

$$\widehat{H}|\psi_n\rangle = E_n|\psi_n\rangle, \tag{3.29}$$

with $n \in 1, ..., 2N$. To simplify our calculations, we use Fourier transformation in the form of

$$|k\rangle = \frac{1}{\sqrt{N}}\sum_{m=1}^{N} e^{imk}|m\rangle, \tag{3.30}$$

for unit cells. k spans the first Brillouin zone. Such a transformation enables us to look for eigenstates in a plane wave form (Bloch's theorem). The state $|\psi_n\rangle$ would then be

$$|\psi_n\rangle = |k\rangle \otimes |u(k)\rangle, \tag{3.31}$$

in which $|u(k)\rangle$ is the eigenstate of the bulk Hamiltonian with form of $|u(k)\rangle = a_n|A\rangle + a'_n(k)|B\rangle$. The general form of the Hamiltonian of bulk momentum space is

$$\widehat{H} = d_0(k)\sigma_0 + \mathbf{d}(k)\cdot\boldsymbol{\sigma}, \tag{3.32}$$

in which σ_i are Pauli matrices. In the context of the SSH model, $d_0(k) = d_3(k) = 0$ and we have

$$d_1(k) = v + w\cos(k),\ d_2(k) = w\sin(k). \tag{3.33}$$

It is a matter of calculation to find the eigen energies as

$$E = \pm\sqrt{v^2 + w^2 + 2vw\cos(k)}, \tag{3.34}$$

in which the presence of the $\pm$ indicates two bands of energy. These two bands of energy are gaped with a width of $\triangle = |v - w|$. The conductivity of the molecules

is explained by this gap. As long as the hopping amplitudes are not equal, the SSH model describes (polyacetylene) insulator whereas for $v = w$ the energy bands become gapless and a conductor would be resulted. Here, we should be cautious though. From the energy point of view, in the staggered case ($v \neq w$), occupied states would have lower energy comparing to unoccupied states (non-staggered with $v = w$).

In the SSH model, the topological invariant is known as winding number. As the "winding" offers, it is a measurement of how many times $\mathbf{n} = \frac{\mathbf{d}(k)}{|\mathbf{d}(k)|}$ winds around the origin in Bloch sphere as k traverses the first Brillouin zone. The winding number is calculated by

$$\gamma = \frac{1}{2\pi}\int_{-\pi}^{\pi}\Big(\mathbf{n}\times\partial_k\mathbf{n}\Big)_k\,dk. \tag{3.35}$$

For polyacetylene molecules, if $v > w$ for staggering amplitudes, the winding number would be $\gamma = 0$ which indicates a trivial phase. In contrast, for $w > v$, the winding number is $\gamma = 1$ and we have a non-trivial phase. It should be noted that for $v = w$ (gapless energy bands), $\mathbf{n}$ would pass the origin of the Bloch sphere as k spans $[-\pi, \pi]$ and topological invariant is not well-defined. To change from a trivial phase to a non-trivial one, we should drag the $\mathbf{n}$ through the origin. The phase transition point is where topological invariant is ill-defined, hence a point in which energy bands are gapless. We call these phase transition points "boundary states" since they reside at the border of two different phases with well-defined topological invariants.

The procedure prescribed by the SSH model is significantly similar to the movement of a walker in the quantum walk. This similarity alongside the quantum walk being universal primitive inspired Kitagawa et al. to use the quantum walk for simulating topological phases described by the SSH model and other ones (Kitagawa et al., 2010).

Topological phases with quantum walks

The bridge to reach from the quantum walk to the SSH model is periodically driven systems or more precisely Floquet operators. A Floquet operator drives the system in time through one complete driving period. The Floquet operator is applied on the system over and over to move the system forward through discrete time steps. This makes the Floquet operator stroboscopic. Considering the definition of the quantum walk and its procedure, one can state that the protocol of the quantum walk is indeed a Floquet operator. Therefore, the protocol of the quantum walk realizes a periodic Floquet evolution that can be mapped to a dimensionless effective Hamiltonian

$$\hat{U} = e^{-i\hat{H}}, \tag{3.36}$$

in which we assumed $\hbar = 1$ and the time it takes for $\widehat{H}$ to be applied is 1. The effective Hamiltonian has a (quasi)energy dispersion, E, which spans $[-\pi, \pi]$. As we established in the last section for the SSH model, the effective Hamiltonian here can be expressed as

$$\widehat{H} = E\mathbf{n} \cdot \boldsymbol{\sigma}, \tag{3.37}$$

which by the mapping between the protocol of the quantum walk and the effective Hamiltonian, one can obtain the energy dispersion through

$$E = i \ln \Xi, \tag{3.38}$$

where Ξ is the eigenvalue of $\widehat{U}$. Since the effective Hamiltonian and energy are momentum dependent, the protocol of the discrete-time quantum walk and its eigenvalues should have a similar dependency. This requires the Fourier transformation (3.14) of the position space of the walk into the momentum space.

Due to our interest in the simulation of the SSH topological phases with the quantum walk, the spatial dimension of the walk would be one. The coin operator of the quantum walk is a generalized coin given by

$$\widehat{C}_\theta = \begin{pmatrix} \cos(\frac{\theta}{2}) & \sin(\frac{\theta}{2}) \\ \sin(\frac{\theta}{2}) & -\cos(\frac{\theta}{2}) \end{pmatrix} = e^{-\frac{i\theta}{2}\sigma_y}, \tag{3.39}$$

in which θ is the rotation angle around y axis that traverses $[0, 2\pi]$. The shift operator is given by Eq. (3.4) which by using Fourier transformation it would be transformed to

$$\widehat{S}_{\uparrow\downarrow}(x) = e^{ik_x\sigma_z}, \tag{3.40}$$

and it is diagonalized in momentum space. The protocol of the quantum walk in momentum space is

$$\widehat{U} = \begin{pmatrix} e^{ik_x\sigma_z}\cos(\frac{\theta}{2}) & e^{ik_x\sigma_z}\sin(\frac{\theta}{2}) \\ e^{ik_x\sigma_z}\sin(\frac{\theta}{2}) & -e^{ik_x\sigma_z}\cos(\frac{\theta}{2}) \end{pmatrix}. \tag{3.41}$$

It is a matter of calculation to find eigenvalues of the protocol and consequently obtain energy as

$$E = \pm \cos^{-1}\left[\cos(\frac{\theta}{2})\cos(k_x)\right]. \tag{3.42}$$

The results indicate the presence of two energy bands (due to $\pm$) that are gaped. These two bands of energy span $[-\pi, \pi]$. The gap between the energy bands could close. The gap-closure happens only for $E = 0$ and $\pm\pi$ at the rotation angles of

$$\theta_{E=\pi} = \pm 2\cos^{-1}[-\sec(k_x)] + 2\pi c, \tag{3.43}$$

$$\theta_{E=0} = \pm 2\cos^{-1}[\sec(k_x)] + 2\pi c, \tag{3.44}$$

where c is an integer. It should be noted that c can be chosen only in a way that θ lies within $[0, 2\pi]$. The obtained energy bands could have three distinctive behaviors (Fidkowski and Kitaev, 2011; Schnyder and Ryu, 2011; Chiu et al., 2016): I) They can be a linear function of the k_x and the gap-closure could happen linearly. This type of the boundary state is Dirac cone. II) They can be a nonlinear function of the k_x and the gap-closure could take place nonlinearly. This type of the boundary state is called Fermi arc. III) Finally, the energy bands can be independent of k_x which is called flat bands, irrespective of gap-closure happens or not.

For the quantum walk considered here, the gap-closure takes place linearly, hence Dirac cone type of boundary states are simulated by this quantum walk. The gapless points in k_x space are only at $k_x = 0$ and $k_x = \pm\pi$. It is a matter of calculation to find the flat bands with $E = \pm\frac{\pi}{2}$ as

$$\theta_{E=\pi/2} = 4\pi c \pm \pi. \tag{3.45}$$

Having energy bands, we are in a position to calculate the group velocity which is associated with the wave function of the walker

$$V(k_x) = \frac{dE}{dk_x} = \pm\frac{\cos(\frac{\theta}{2})\sin(k_x)}{\sqrt{1 - [\cos(\frac{\theta}{2})\cos(k_x)]^2}}. \tag{3.46}$$

For linear gap-closure, the walker around the gapless point has constant group velocity but with different signs. The boundary state or phase transition point can be detected via a sudden change of the sign of group velocity. In fact, at the gapless point, the group velocity becomes ill-defined. This is yet another means to detect phase transition points. For flat bands on other hand, the group velocity is zero which indicates that the walker is localized.

To find the topological invariant, we find $\mathbf{n}$ as

$$\mathbf{n} = \frac{1}{\sqrt{1 - [\cos(\frac{\theta}{2})\cos(k_x)]^2}} \begin{pmatrix} \sin(\frac{\theta}{2})\sin(k_x) \\ \sin(\frac{\theta}{2})\cos(k_x) \\ -\cos(\frac{\theta}{2})\sin(k_x) \end{pmatrix}, \tag{3.47}$$

which becomes ill-defined at the gapless points of energy bands. Before we calculate the topological invariant, we should check the symmetries that the system has. To this end, we use the following guidelines for checking the presences of certain symmetries and finding their operators:

- PHS: To check the presence of the PHS, we look at the matrix elements of the protocol of the quantum walk. If all the elements are real-valued, the complex conjugate of the protocol would be equal to itself ($\widehat{U}^* = \widehat{U}$). Consequently and in contrast, the effective Hamiltonian would admit $\widehat{H}^* = -\widehat{H}$ which means the presence of PHS. Following these arguments, one can state that if the coin operators in the protocol of the quantum walk rotate the walker's state in xy plane, the protocol would have the PHS. To break the PHS, we simply should consider the rotation axis of the coin in z plane.

- TRS: The presence of the TRS can be checked through the energy bands. For each k, we have two energy eigenvalues associated to two states by $\pm|E(k)|$. If the TRS is present, then we will have $|E(k)| = |E(-k)|$. The violation of this condition indicates the absence of the TRS.

- CHS: The existence of PHS and TRS guarantees the presence of the CHS. The presence of the CHS limits the $\mathbf{n}$ to lie on a great circle of a Bloch sphere. Therefore, if $\mathbf{n}$ does not lie on a plane that includes the origin of the Bloch sphere, the system does not have the CHS.

The protocol in Eq. (3.41) admits all three symmetries. Since $\widehat{H}^* = -\widehat{H}$, the PHS operator would be $\widehat{\mathcal{P}} = \widehat{K}$ in which $\widehat{K}$ is the complex conjugate operator. To find the CHS operator, we use the fact that $\mathbf{n}$ should lie in a plane containing origin in the Bloch sphere. We define a vector $\boldsymbol{A}$ as

$$\boldsymbol{A} = \begin{pmatrix} \sin(\frac{\theta}{2}) \\ 0 \\ -\cos(\frac{\theta}{2}) \end{pmatrix}, \tag{3.48}$$

which is perpendicular to $\mathbf{n}$ for arbitrary k_x. The CHS operator is then build by

$$\widehat{\Gamma} = \boldsymbol{A} \cdot \boldsymbol{\sigma}. \tag{3.49}$$

Finally, using the PHS and CHS operators, we can find the TRS operator as $\widehat{\mathcal{T}} = \widehat{\Gamma}\widehat{\mathcal{P}}$. The square of the all symmetry operators equal to $\widehat{\mathcal{P}}^2 = \widehat{\mathcal{T}}^2 = \widehat{\Gamma}^2 = +\widehat{I}$ which confirms that the effective Hamiltonian belongs to the SSH model and the protocol of the

quantum walk simulates topological phases of BDI class. The topological invariant is calculated as

$$\gamma = \int_{-\pi}^{\pi} \left(\mathbf{n} \times \frac{\partial \mathbf{n}}{\partial k_x} \right) \cdot \mathbf{A} \frac{dk_x}{2\pi} = -\sin(\frac{\theta}{2}) \sqrt{\csc(\frac{\theta}{2})}. \tag{3.50}$$

The resulted topological invariant indicates that the considered protocol of the quantum walk can simulate only non-trivial topological phases. To overcome this problem, Kitagawa et al. proposed to modify the simple-step protocol to a split-step one in the following form (Kitagawa et al., 2010)

$$\widehat{U} = \widehat{S}_{\uparrow}(x)\widehat{C}_{\alpha}\widehat{S}_{\downarrow}(x)\widehat{C}_{\beta}. \tag{3.51}$$

In the new protocol, a single step of the walk includes a rotation of internal states of the walker with $\widehat{C}_{\beta}$, a displacement of its position with $\widehat{S}_{\downarrow}$, the second rotation of internal states with $\widehat{C}_{\alpha}$ and finally, its displacement with $\widehat{S}_{\uparrow}$. The coin and shift operators are given by

$$\widehat{C}_{\alpha} = e^{-\frac{i\alpha}{2}\sigma_y}, \tag{3.52}$$

$$\widehat{C}_{\beta} = e^{-\frac{i\beta}{2}\sigma_y}, \tag{3.53}$$

$$\widehat{S}_{\uparrow}(x) = \sum_x [|\uparrow\rangle\langle\uparrow| \otimes |x+1\rangle\langle x| + |\downarrow\rangle\langle\downarrow| \otimes |x\rangle\langle x|], \tag{3.54}$$

$$\widehat{S}_{\downarrow}(x) = \sum_x [|\uparrow\rangle\langle\uparrow| \otimes |x\rangle\langle x| + |\downarrow\rangle\langle\downarrow| \otimes |x-1\rangle\langle x|], \tag{3.55}$$

which by using the Fourier transformation, we can rewrite the shift operators in diagonalized forms of $\widehat{S}_{\uparrow}(x) = e^{\frac{ik_x}{2}(\sigma_z - 1)}$ and $\widehat{S}_{\downarrow}(x) = e^{\frac{ik_x}{2}(\sigma_z + 1)}$. The rotation angles α and β span $[-\pi, \pi]$.

The first consequence of this modification in the protocol is the independency of the probability density on parity. In other words, with split-step protocol, in even (odd) steps, odd (even) positions have also non-zero probability densities. This is because in the split-step protocol, in each step, the walker can remain in its initial position. This is similar to the Hamiltonian of the SSH (3.28) in which the electron could stay in the same unit cell. The energy bands of the split-step protocol are obtained as

$$E = \pm \cos^{-1}\left[\cos(\frac{\alpha}{2})\cos(\frac{\beta}{2})\cos(k_x) - \sin(\frac{\alpha}{2})\sin(\frac{\beta}{2}) \right]. \tag{3.56}$$

It is a matter of calculation to find the group velocity and $\mathbf{n}$ as

$$V(k_x) = \pm \frac{\cos(\frac{\alpha}{2})\cos(\frac{\beta}{2})\sin(k_x)}{\sqrt{1-[\cos(\frac{\alpha}{2})\cos(\frac{\beta}{2})\cos(k_x)-\sin(\frac{\alpha}{2})\sin(\frac{\beta}{2})]^2}}, \tag{3.57}$$

$$\mathbf{n} = \frac{1}{\sin(E)}\begin{pmatrix} \cos(\frac{\alpha}{2})\sin(\frac{\beta}{2})\sin(k_x) \\ \sin(\frac{\alpha}{2})\cos(\frac{\beta}{2})+\cos(\frac{\alpha}{2})\sin(\frac{\beta}{2})\cos(k_x) \\ -\cos(\frac{\alpha}{2})\cos(\frac{\beta}{2})\sin(k_x) \end{pmatrix}, \tag{3.58}$$

which are ill-defined at the gapless points of the energy bands. The split-step protocol has all three symmetries. The PHS operator is the same as the one introduced for the simple-step protocol. In the case of CHS, we define $\mathbf{A}$ as

$$\mathbf{A} = \begin{pmatrix} \cos(\frac{\beta}{2}) \\ 0 \\ \sin(\frac{\beta}{2}) \end{pmatrix}, \tag{3.59}$$

which gives us the CHS operator in the form of

$$\widehat{\Gamma} = \begin{pmatrix} \sin(\frac{\beta}{2}) & \cos(\frac{\beta}{2}) \\ \cos(\frac{\beta}{2}) & -\sin(\frac{\beta}{2}) \end{pmatrix}. \tag{3.60}$$

The TRS operator is then similarly obtained with $\widehat{\mathcal{T}} = \widehat{\Gamma}\widehat{\mathcal{P}}$. Since the square of all the symmetry operators equal to $+\widehat{I}$, the protocol simulates topological phases of BDI class and specifically the SSH model. To find the phase structure of the simulated topological phases by the split-step protocol, we use the following relation

$$\begin{cases} \left|\frac{\tan(\frac{\alpha}{2})}{\tan(\frac{\beta}{2})}\right| < 1 \quad \gamma = 1 \text{ non-trivial phase} \\ \\ \left|\frac{\tan(\frac{\alpha}{2})}{\tan(\frac{\beta}{2})}\right| > 1 \qquad \gamma = 0 \text{ trivial phase} \end{cases}, \tag{3.61}$$

which is obtained by considering $k_x = c\pi$ and calculating the topological invariant. Contrary to simple-step protocol, the split-step protocol can simulate both trivial and non-trivial phases that are observed in the SSH model.

In order to simulate edge states with this quantum walk, Kitagawa et al. proposed a modification in the split-step protocol (Kitagawa et al., 2010). In their proposal, they suggested considering the rotation angle of the second coin in the split-step protocol to be position-dependent, $\alpha = \alpha(x)$. In such a case, one can create a phase

boundary in which the phases around it would be topologically distinct (trivial and non-trivial phases).

The position dependency of the second coin is then considered via $\alpha(x) = \frac{1}{2}(\alpha_+ + \alpha_-) + \frac{1}{2}(\alpha_+ - \alpha_-)\tanh(\frac{x}{3})$. With such a position dependency and proper choices for the rotation angles, one can create the phase boundary around $x = 0$ in which for $x < 0$, the observed phase is trivial with $\gamma = 0$ while for $x > 0$ the simulated phase has $\gamma = 1$. It should be noted that creation of the boundary depends on rotation angles of β, α_+, and α_-. It is possible to have a situation where for arbitrary x, there is no boundary state, and the simulation results in only a non-trivial or trivial phase.

Using the same principles, Kitagawa et al. introduced series of protocols for the quantum walk in one- and two-dimensional position space which could simulate all types of the topological phases that are observed in the same dimensions in condensed matter physics (Kitagawa et al., 2010). The periodic table of topological phases includes dimensions higher than two as well. Therefore, the proper protocols for the quantum walk in three-dimensional position space to simulate corresponding topological phases yet to be addressed. Another issue is the simulation of the different boundary states. The quantum walk would be a universal simulator of the topological phenomena only and only if it can simulate all types of the topological phases and boundary states together.

These two issues and attaining a high level of controllability over simulations motivate us to look for quantum walks that could address these issues. To this end, we propose two types of modification in the quantum walks: I) Using step-dependent coins in the protocol of quantum walks II) Considering entangled qubits and entanglement as tools to overcome these issues.

4

DISCRETE-TIME QUANTUM WALK WITH STEP-DEPENDENT COINS

In earlier studies of the quantum walks and the guidelines for developing algorithms based on the quantum walk, the decoherence was proposed as a tool to control the walker's behavior and its properties. While it sounds theoretically achievable, in experimental setups and specifically, in the applications of the quantum walks in quantum computers and computation, the presence of the decoherence could be fatal. This motivates us to look for possible proposals that would provide us with a high level of control over the quantum walks while keeping the state of walker pure (without resorting to decoherence). The first proposal is using step-dependent coins instead of the usual (step-independent) coins in the protocols of the quantum walks.

Parts of the material presented in this chapter were published previously in the following references:

Controlling quantum random walk with a step-dependent coin
S. Panahiyan and S. Fritzsche
New. J. Phys. **20**, 083028 (2018).

Simulation of the multiphase configuration and phase transitions with quantum walks utilizing a step-dependent coin
S. Panahiyan and S. Fritzsche
Phys. Rev. A **100**, 062115 (2019).

Controllable simulation of topological phases and edge states with quantum walk
S. Panahiyan and S. Fritzsche
Phys. Lett. A **384**, 126828 (2020).

Simulation of novel cell-like topological structures with quantum walk
S. Panahiyan and S. Fritzsche
Eur. Phys. J. Plus **135**, 626 (2020).

Fidelity susceptibility near topological phase transitions in quantum walks
S. Panahiyan, W. Chen and S. Fritzsche
Phys. Rev. B **102**, 134111 (2020).

Toward simulation of topological phenomena with one-, two- and three-dimensional quantum walks
S. Panahiyan and S. Fritzsche
Phys. Rev. A **103**, 012201 (2021).

4.1 SETUP OF THE WALK

In the quantum walk, compared to its classical counterpart, there is an entanglement between the internal (coin) space and position space. In fact, it is argued that the diverse results that are observed in the quantum walk are due to the interplay of the coin and walker, hence the entanglement between two sub-spaces of the walk. Such a contribution poses the question that whether the coin operator could play a more significant role in the behavior of the walker and its properties in the quantum walk?

To answer this question, we consider the coin operators in the protocols of the quantum walk to be step-dependent. This means that coins are no longer fixed operators through the evolution of the quantum walk and they change from one step to another one. There are rather different approaches to achieve step-dependency as a feature for the coins. Here, for this sake of simplicity, we propose to realize the coin operators for a quantum walk with two internal states in the following form (Panahiyan and Fritzsche, 2018)

$$\widehat{C}_\theta \;=\; \begin{pmatrix} \cos(T\theta) & \sin(T\theta) \\ \sin(T\theta) & -\cos(T\theta) \end{pmatrix}, \tag{4.1}$$

in which T refers to the number of the step and characterizes the step-dependency of the coin operator. Such a coin operator is unitary which alongside a unitary shift operator results in a Hermitian and unitary protocol for the quantum walk. It should be noted that since all of the operators in our consideration are unitary, one can build a reverse protocol that brings back the walker to its initial state.

To investigate the effects of the step-dependent coin on the quantum walk, we study a one-dimensional quantum walk with two internal states of $\{|\uparrow\rangle, |\downarrow\rangle\}$. The walker's position space is a one-dimensional Hilbert space spanned by $\{|x\rangle : x \in \mathbb{Z}\}$. The total Hilbert space of the walk is then given by the tensor product of the two sub-spaces of $\mathcal{H} = \mathcal{H}_P \otimes \mathcal{H}_C$. The shift operator is the same as the one given in Eq.

(3.4). For the quantum walk with step-dependent coins, the final state of the walker is obtained through slightly different successive application of the unitary protocol

$$|\psi\rangle_{fin} \;=\; |\psi\rangle_T \;=\; \prod_{m=1}^{T} \widehat{U}(m)\,|\psi\rangle_{int.} \;. \tag{4.2}$$

We consider the initial state to be in form of (3.7). The application of shift-coin operator with considered initial states results into

$$\begin{aligned}
&|\uparrow\rangle \otimes |0\rangle \\
&\xRightarrow{1th} \sin(\theta)\,|\downarrow\rangle \otimes |-1\rangle + \cos(\theta)\,|\uparrow\rangle \otimes |1\rangle \\
&\xRightarrow{2th} \cos(2\theta)\sin(\theta)\,|\downarrow\rangle \otimes |-2\rangle + \sin(2\theta)[\sin(\theta)\,|\uparrow\rangle + \cos(\theta)\,|\downarrow\rangle] \otimes |0\rangle + \cos(2\theta)\cos(\theta)\,|\uparrow\rangle \otimes |2\rangle \\
&... \\
&\xRightarrow{Tth} \left(\prod_{n=1}^{T} \cos(n\theta)\right) |\uparrow\rangle \otimes |T\rangle_P + ... + (-1)^{T+1} \left(\prod_{n=1}^{T} \frac{\cos(n\theta)}{\cos(\theta)}\right) \sin(\theta)\,|\downarrow\rangle \otimes |-T\rangle_P \,.
\end{aligned} \tag{4.3}$$

In general, the walker's wave function occupies $T+1$ positions after T steps which indicates a non-zero probability at $T+1$ positions. The parity dependency could also be observed here. In other words, for odd (even) steps, only the odd (even) positions have non-zero probability densities. For an arbitrary rotation angle, the walker occupies only positions within $[-T, T]$.

While they are different ways to categorize the probability density distributions in the position space of the quantum walk, we introduce the following categorization:

- Localized walk: as the title indicates the probability density distribution is whether concentrated in one position or a very limited number of different positions. Through the evolution of the walk, the place of concentration could change but irrespective of the step number and the relocation, the absence of the distribution in the wave function of the walker remains intact. To provide a further distinction, we can introduce two sub-classes for Localized walk; I) Free localized walk in which the walker shows a free particle behavior and at step T of the walk, the probability density at positions $\pm T$ would only be non-zero. II) Bounded localized walk or more precisely trapped walker in which through the evolution of the quantum walk, the walker spans only a limited number of the positions around the initial position. Careful examination confirms that usually, quantum walks in such a category present recurrence phenomena.

- Classical-like walk: the main characteristic of this class is the observation of the Gaussian or significantly close to Gaussian probability density distribution. This indicates smaller variance and slower speed of spread for the wave function

of the walker as the quantum walk proceeds. We can also divide this class into sub-classes of the compact classical walk, which has a rather smaller variance comparing to the classical walk with the distribution limited to several positions, and the usual classical walk which shows behaviors similar to classical-like behaviors.

- Semi classical/quantum-like walk: the characteristic behavior of the walker has similarity to both classical and quantum walks. For instance, there is a peak at the initial position in probability density distribution but other peaks are observed in the most left- or right-hand side positions. The probability density distribution has significant similarity to the quantum walk in the presence of decoherence.

- Quantum-like walk: in this class, we have the ballistic behavior and asymmetric probability density distribution. There are noticeable peaks at the most left- and right-hand side positions that step-dependently move away from the initial position. In addition, there is a uniform distribution around the initial position.

The main idea in such a categorization comes from the similarity that each distribution shows to already developed and studied cases in the literature. For example, in the case of the classical-like walk, we identify the probability density distribution that has Gaussian-like behavior belonging to this category. As for semi classical/quantum-like walk class, it refers to distributions that were observed for quantum walks with decoherence.

If we consider the initial state of (3.7), the quantum walk with step-dependent coin can present all the classes that we have pointed out (see Fig. 4.1): for $\theta = 0$, the walker shows free localized walk behavior while for $\theta = \pi/4$ and $\pi/2$, the walker has bounded localized walk. It should be noted that in the case of $\theta = \pi/4$, there is a 50-50 split in the walker's probability density distribution in two positions. By considering $\theta = \pi/12$ and $\theta = 3.59\pi/2$, we observe compact and recurrent classical-like probability density distributions. $\theta = 2\pi/5$ and $\pi/5$ mark two different cases of semi classical/quantum-like class while $\theta = \pi/3$ belongs to the quantum-like class. We have summarized these cases in a table 4.1. The justifications for our classification are provided in 7.2.

In order to fully comprehend the contributions of the step-dependent coins, we make a contrast between the cases that we have studied with their step-independent coins counterparts (see Fig. 4.2). For the localized walk with rotation angles of $\theta = 0$ and $\pi/2$, we observe identical behaviors for step-dependent and -independent cases with just a difference in the position of the localization. This indicates that observed behaviors are inherent for these rotation angles. For the quantum-like and semi

Classes	**Rotation angle** θ
Localized: free	0
Localized: bounded	$\pi/2$
Localized: bounded with periodic splitting	$\pi/4$, $\pi/6$
Compact classical-like	$\pi/12$, $3.59\pi/5$
Semi-classical/quantum-like	$\pi/5$, $2\pi/5$
Quantum-like	$\pi/3$

Table 4.1: Observed classes of the probability density distributions and their corresponding rotation angles for one-dimensional quantum walks with step-dependent coins.

classical/quantum-like cases, we detect larger variances for the probability density distributions in the case of step-dependent coins comparing to step-independent ones. Additionally, the probability of finding the walker at the initial position is larger for the quantum walks with step-dependent coins.

The differences between the step-dependent and -independent coins become pronounced in the case of the rotation angle of $\theta = \pi/4$. For step-independent coin, such a rotation angle results in the Hadamard walk that we discussed in previous sections. Whereas in the case of step-dependent coin, this rotation angle induces a trapped localized behavior with a periodic splitting in the probability density distribution. Similarly, for classical-like behaviors ($\theta = 3.59\pi/5$ or $\pi/12$), we observe significantly different variances in the probability density distribution of the quantum walks with step-independent coins comparing to the ones with step-dependent coins.

While we have outlined how the variances of quantum walks with step-dependent and -independent coins differ with plotted diagrams, we quantify this issue furthermore by studying the number of the positions occupied by the wave function of the walker, hence positions with non-zero probability densities (see Fig. 4.3). To this end, we consider positions with probability densities larger than 10^{-4} the occupied ones. The diagrams confirm that irrespective of the step number, the quantum-like and semi classical/quantum-like cases observed for step-dependent coins have a larger number of occupancy and hence are faster comparing to their counterparts with step-independent coins.

Finally, we study the entropy as the last factor to quantify the effects of step-dependent coins on quantum walks and compare them with their step-independent counterparts. Initially, entropy was introduced in thermodynamics as a tool to quantify the amount of the disorder in a thermodynamical system. Later on, the principle was adopted by other fields of physics and science. In information theory, quantum or classical, the entropy is associated with the amount of uncertainty that is present in the state of a physical system. The amount of uncertainty gives us

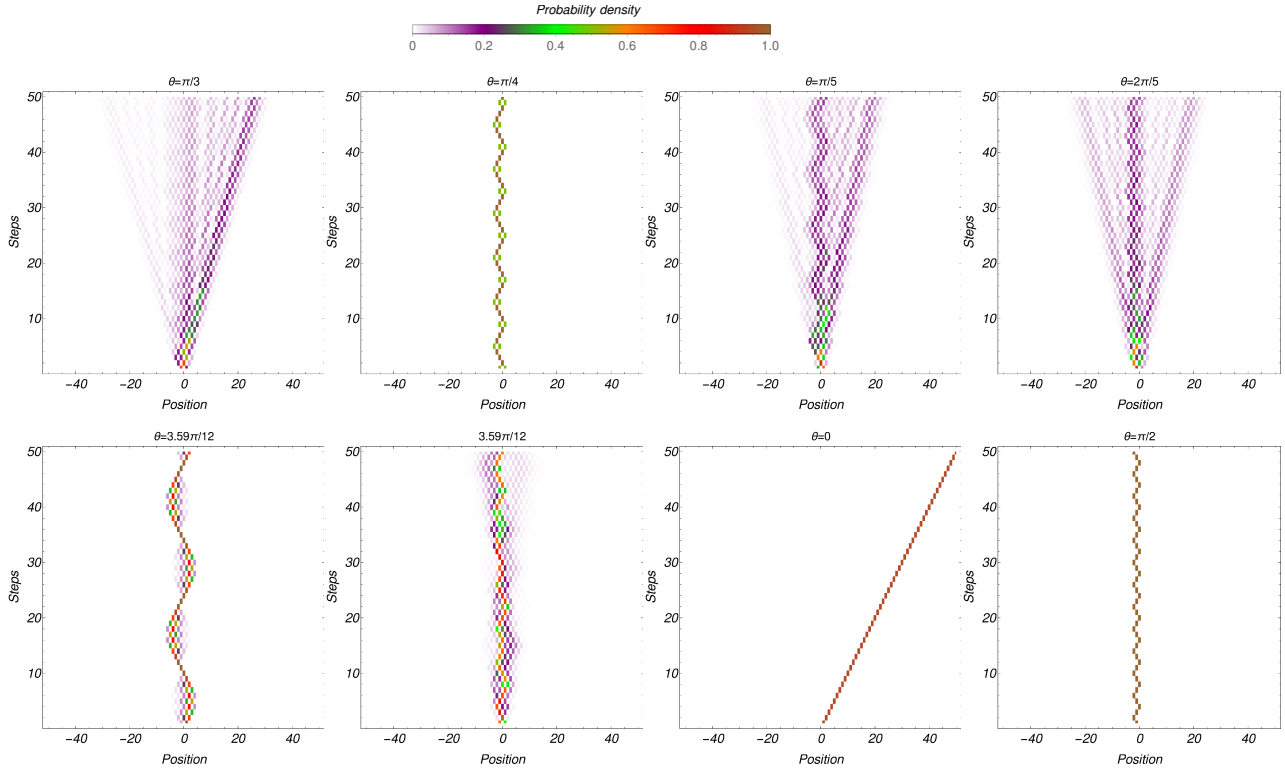

Figure 4.1: Different classes of probability density distributions in position space for the quantum walks with step-dependent coins. We observe diverse behaviors for the walker ranging from complete localization to ballistic spread.

direct access to assess the amount of information in the system. Higher uncertainty means that to describe the state of the system, we need more information. From another perspective, if we have an evolving system such as the quantum walk, smaller entropy indicates a deterministic behavior while higher entropy marks highly random behavior for the walker. The deterministic behavior for the walker in position space is considered as a destructive consequence for algorithm development and communication applications of the quantum walk (Keating et al., 2007).

For classical and quantum systems, different types of entropy are introduced. For classical systems, Shannon entropy, introduced by Claude Shannon in 1948, is used (Shannon, 1948). For quantum systems, von Neumann entropy is the tool to measure the entropy. The von Neumann approach to entropy uses the density matrix. This is expected since the quantum-mechanical systems are made of sub-spaces that are entangled and formalized with tensor products. For our quantum walk, the state of the system at step T of the walk is given by $|\psi\rangle_T$ which consequently gives us the density matrix at step T as

$$\hat{\rho}(T) \quad = \quad |\psi(x)\rangle_{T\,T}\langle\psi(x)|. \tag{4.4}$$

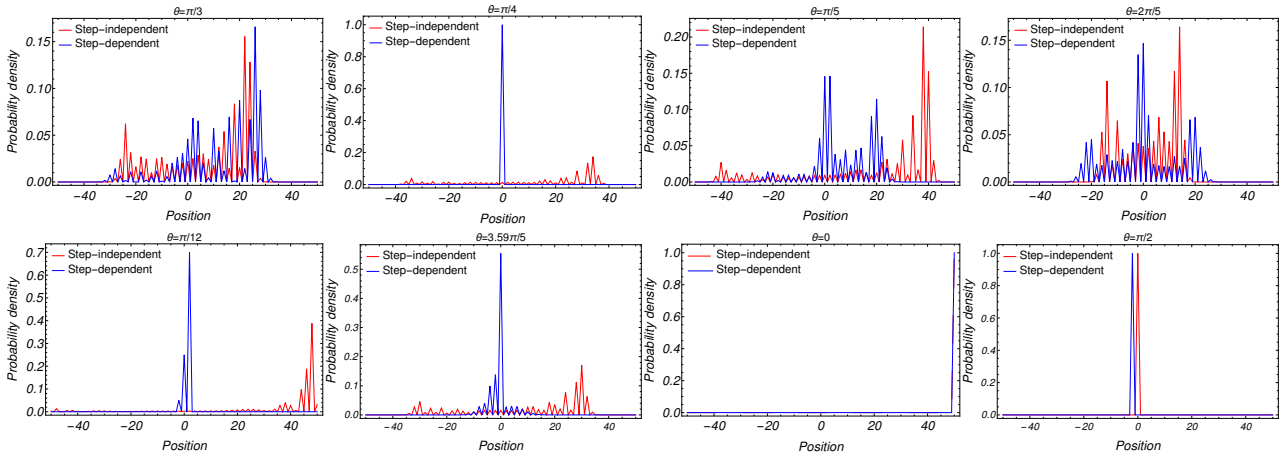

Figure 4.2: Probability density distributions of the quantum walks with step-dependent coins versus their step-independent counterparts. We observe highly different behaviors for these two types of walks while the step-dependent ones have rather diverse behaviors.

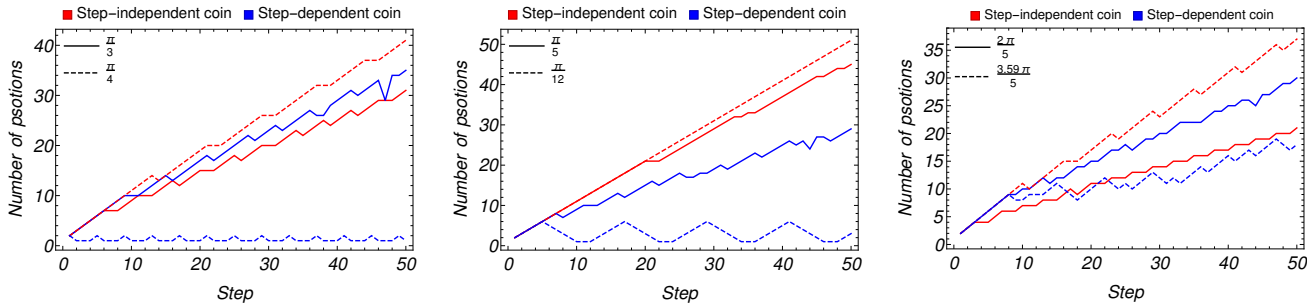

Figure 4.3: Variances of the quantum walks with step-dependent coins versus their step-independent counterparts. We observe a larger spread for quantum-like class of the quantum walk with step-dependent coin.

Since our quantum walk has two sub-spaces of coin and position spaces, one can find the entropy associating with these sub-spaces. To find the entropy of position space (S_P), one should trace the density matrix over coin space and find the reduced density matrix in the form of $\hat{\rho}^P(T) = Tr_C(\hat{\rho}(T))$, which gives the von Neumann entropy at time T by

$$S_P = -Tr(\hat{\rho}^P(T) Log \hat{\rho}^P(T)). \tag{4.5}$$

For our quantum walk with step-dependent coins, Eq. (4.5) reduces to

$$S_P = -\sum_n P_{n,T} Log P_{n,T}, \tag{4.6}$$

in which, $P_{n,T}$ are eigenvalues of Hermitian matrix with the element $\hat{\rho}^P(T)$. The obtained entropy in Eq. (4.6) is Shannon entropy. The reduction of the von Neumann entropy to Shannon entropy is due to the purity of the system. In other words, if the

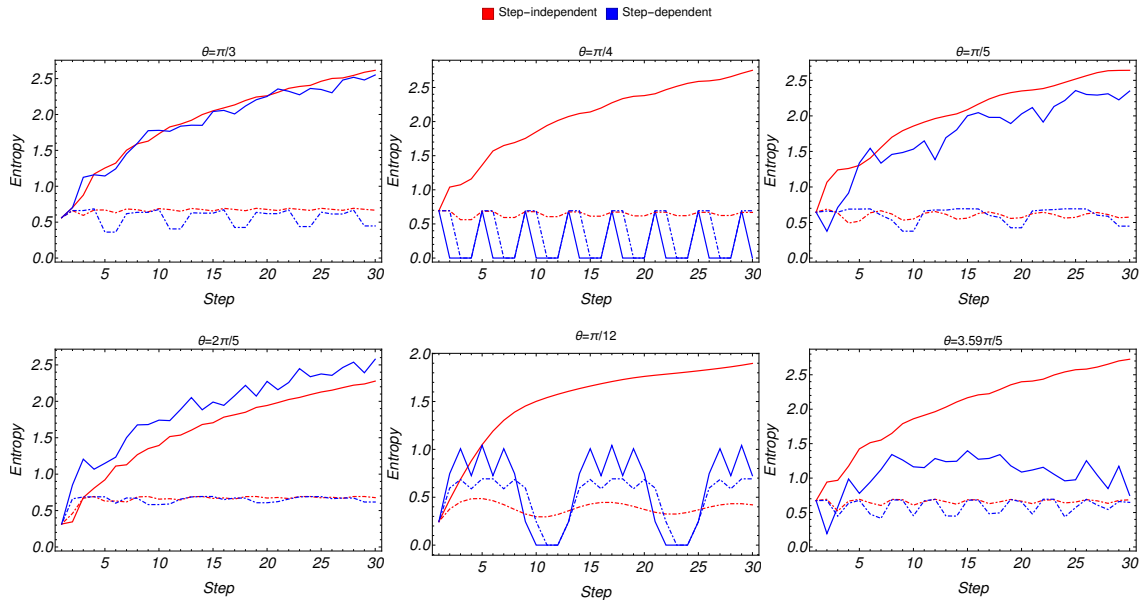

Figure 4.4: Entropy of position (solid lines) and coin (dashed lines) spaces for two cases of the quantum walks with step-dependent and step-independent coins.

state of a system after a process is pure, the von Neumann entropy becomes identical to Shannon entropy. Therefore, $P_{n,T}$ is the probability density of the position n at step T. The same can be done for finding the entropy of the coin space (S_C) provided the trace of the density matrix is done over position space.

The first consequence of the Eq. (4.6) is vanishing entropy of position or coin space for a fully localized walk whether in position or coin space. This is expected since to describe the position or internal state of the walker, we need the least amount of information. In contrast, the homogeneous quantum walk with equal probability densities over the maximum number of the positions or internal states has maximum entropy.

Quantum walks with step-independent coins do not show any diverse behavior. Therefore, the variances of the walks increase step-dependently which in return results in the entropy of position space being an increasing function of steps (see Fig. 4.4). In contrast, for quantum walks with step-dependent coins, we observe diverse behaviors that make the dependency of the entropy on step number a subject of the rotation angle of the coin.

In general, the entropy of the position space for quantum walks with step-dependent coins is smaller than its step-independent counterparts. Despite the increments in the variances of the probability density distributions for semi classical/quantum-like and quantum-like classes, their entropy is not always an increasing function of the steps. In fact, it could decrease in certain steps. This indicates that in these steps, the quantum walks gain a more deterministic nature in their wave functions.

In the case of the entropy of the coin space, since there are only two internal states, the entropy has an upper limit. The maximum entropy is achieved if the probability densities of the two internal states are equal. Generally, for quantum walks with step-independent coins, the entropy of the coin space has a damped oscillating behavior which indicates convergence of the entropy to a specific value. This specific value depends on the rotation angle of the coin. The convergence also points out to stabilization in probability density distribution in coin space as the walk proceeds. In contrast, the entropy of the coin space for quantum walks with step-dependent coins highly depends on the class. For semi classical/quantum-like and quantum-like walks, damped oscillation, the convergence of the entropy to a specific value, and stabilization are observed. Whereas, for localized class, periodic behavior is evident. In the case of the classical-like class, a random and irregular behavior emerges. Interestingly, it is possible to find steps where both the entropy of position and coin spaces are simultaneously zero in case of the localized walk. In this situation, a complete localization in all degrees of freedom of the walker takes place.

4.2 SIMULATION OF TOPOLOGICAL PHENOMENA

In the last section, we established the controllability over the walker's behavior and its properties by the inclusion of step-dependent coins in protocols of quantum walks. A question arises on how the controllable features would contribute to applications of the quantum walk? To address this issue, we take a look at simulations of the boundary states, topological phases, and edge states with step-dependent protocols. Before we do so, we introduce the following notations for the sake of brevity

$$\cos(\frac{Tj}{2}) = \kappa_j, \qquad \sin(\frac{Tj}{2}) = \lambda_j,$$

where j could only be θ, α, β, γ, λ and ζ which are rotation angles and span $[-\pi, \pi]$ provided that protocol is split-step. In the case of a simple-step protocol, the rotation angle would span $[0, 2\pi]$. It should be noted that for one-dimensional cases, we denote the topological invariant with γ which should not be mixed with rotation angle in the two- and three-dimensional cases. T is the positive-valued step number of the quantum walk and characterizes the step-dependency of the coins. The energy bands vary through $[-\pi, \pi]$ for all of the classes and irrespective of dimensionality. The group velocity, $\mathfrak{n}$, and topological invariant are all ill-defined at boundary states, hence phase transition points.

4.2.1 *Topological phenomena in one dimension*

There are four classes of the topological phases observed in one-dimensional systems including AIII, BDI, CII, and DIII. Here, we use step-dependent coins and introduce a series of protocols for the quantum walk to simulate all of them.

One-dimensional BDI class

The protocols of the quantum walk that simulate BDI class in one dimension are simple-step and split-step ones. With the simple-step protocol, we can only simulate non-trivial phases. In contrast, with the split-step protocol, we are able to simulate trivial and non-trivial phases. The simple-step protocol is given by (Panahiyan and Fritzsche, 2019)

$$\widehat{U} \;=\; \widehat{S}_{\uparrow\downarrow}(x)\widehat{C}_{\theta}, \tag{4.7}$$

where $\widehat{C}_{\theta} = e^{-\frac{iT\theta}{2}\sigma_y}$. The shift operator $\widehat{S}_{\uparrow\downarrow}(x)$ is provided in Eq. (3.4) which by using the Fourier transformation, it can be written as $\widehat{S}_{\uparrow\downarrow}(x) = e^{ik_x\sigma_z}$.

The protocol of the quantum walk is Hermitian and its determinant is 1. Consequently, the effective Hamiltonian related to this protocol is traceless. This results in symmetrical energy bands around $E = 0$. The eigenvalues of the protocol are obtained as $\Xi = \cos(k_x)\kappa_\theta \pm \sqrt{[\cos(k_x)\kappa_\theta]^2 - 1}$ which using them leads to two gaped energy bands in the forms of

$$E \;=\; \pm\cos^{-1}\Big[\kappa_\theta\cos(k_x)\Big]. \tag{4.8}$$

The energy bands close their gap at $E = 0$ and $\pm\pi$ provided that the rotation angle yields

$$\theta_{E=\pi} \;=\; \frac{\pm 2\cos^{-1}[-\sec(k_x)] + 4\pi c}{T} = \begin{cases} \frac{4\pi c}{T} & k_x = -\pi \\ \frac{\pm 2\pi + 4\pi c}{T} & k_x = 0 \\ \frac{4\pi c}{T} & k_x = \pi \end{cases}, \tag{4.9}$$

$$\theta_{E=0} \;=\; \frac{\pm 2\cos^{-1}[\sec(k_x)] + 4\pi c}{T} = \begin{cases} \frac{\pm 2\pi + 4\pi c}{T} & k_x = -\pi \\ \frac{4\pi c}{T} & k_x = 0 \\ \frac{\pm 2\pi + 4\pi c}{T} & k_x = \pi \end{cases}, \tag{4.10}$$

where c is an integer. The energy bands could be in form of the flat bands without any slope if the rotation angle is

$$\theta_{E=\pi/2} = \frac{\pm 4\pi c + \pi}{T}. \tag{4.11}$$

To obtain the topological invariant and study its behavior, we first find $\mathbf{n}$ in the form of

$$\mathbf{n} = \frac{1}{\sin(E)} \begin{pmatrix} \kappa_\theta \sin(k_x) \\ \lambda_\theta \cos(k_x) \\ -\kappa_\theta \sin(k_x) \end{pmatrix}. \tag{4.12}$$

Next, the vector $\mathbf{A}$, perpendicular to $\mathbf{n}$ for arbitrary k_x, is found as

$$\mathbf{A} = \begin{pmatrix} \kappa_\theta \\ 0 \\ \lambda_\theta \end{pmatrix}. \tag{4.13}$$

The effective Hamiltonian has three symmetries of CHS, PHS, and TRS. The CHS operator is obtained as

$$\widehat{\Gamma} = \begin{pmatrix} \lambda_\theta & \kappa_\theta \\ \kappa_\theta & -\lambda_\theta \end{pmatrix}. \tag{4.14}$$

The PHS operator is complex conjugate, $\widehat{K}$, and consequently, the TRS operator is $\widehat{\Gamma}\widehat{K}$. All three symmetry operators square to $+\widehat{I}$ which shows that this protocol indeed simulates BDI class of the topological phases. We find the topological invariant as

$$\gamma = -\lambda_\theta \sqrt{\csc(\frac{T\theta}{2})}. \tag{4.15}$$

The step-dependency of the Hamiltonian, the energy bands, and $\mathbf{n}$ indicate the topological phases and the boundary states (gap-closure) also depend on the step number of the quantum walk. If T is odd, then the gap-closure takes place $\frac{T+1}{2}$ times at both $E = 0$ and $\pm\pi$. Whereas for even number of steps, the energy gap closes $\frac{T}{2}$ times at $E = 0$ and $\frac{T+1}{2}$ times at $\pm\pi$. Therefore, there is a parity dependency of the gap-closure at $E = 0$ and $\pm\pi$ for odd and even steps. In addition, the interval between two boundary states (where the topological phases are) is a decreasing function of the steps. We call this interval the size of the phase and we notice that this size

shrinks and larger numbers of topological phases and boundary states are formed as the quantum walk proceeds. Therefore, we observe the formation of multiple topological phases (multiphase configuration) and their corresponding boundary states (multicriticality).

The obtained topological invariant in Eq. (4.15) confirms the simulation of the only non-trivial phases with the winding number of the $\gamma = \pm 1$. The positivity or negativity of γ is determined by the winding direction of the $\mathbf{n}$ as k_x traverses through the first Brillouin zone; $\gamma = 1$ is associated to the counterclockwise winding direction, while $\gamma = -1$ represents the clockwise winding direction. As we scan θ to investigate the type of the topological phases, we find that the first interval of topological phases has always $\gamma = -1$, irrespective of the step number. In general, if T is odd, then there are $\frac{T+1}{2}$ phases with winding number $\gamma = -1$ and $\frac{T-1}{2}$ phases with winding number $\gamma = 1$. In contrast, for even steps, the number of phases with $\gamma = -1$ and $\gamma = 1$ are equal and given by $\frac{T}{2}$.

In addition, we notice that if the interval of phase starts with a gapless point of $E = 0$ and ends with a gapless point of $E = \pm\pi$, the winding number of the interval of phase would be $\gamma = -1$. If the interval of phase has a start with gapless point $E = \pm\pi$ and end with gapless point $E = 0$, the winding number is $\gamma = 1$ for that interval. This can be used to indirectly measure the topological invariant just by studying the energy bands. Finally, from one phase to another one, the topological invariant changes. Therefore, we have a phase transition between two different non-trivial phases.

Due to obtained gapless points, the only possible way for the energy bands to close their gap is linearly in this protocol. Therefore, this simple-step protocol can only simulate Dirac cone boundary states and two non-trivial topological phases in BDI class. To detect the presence of the boundary states experimentally, one can use the method of the statistical moments (Cardano et al., 2016).

The split-step protocol that simulates trivial and non-trivial phases simultaneously is given by (Panahiyan and Fritzsche, 2020a)

$$\widehat{U} = \widehat{S}_{\uparrow}(x)\widehat{C}_{\alpha}\widehat{S}_{\downarrow}(x)\widehat{C}_{\beta}, \tag{4.16}$$

in which the coin and shift operators are

$$\widehat{C}_{\alpha} = e^{-\frac{iT\alpha}{2}\sigma_y}, \tag{4.17}$$

$$\widehat{C}_{\beta} = e^{-\frac{iT\beta}{2}\sigma_y}, \tag{4.18}$$

$$\widehat{S}_{\uparrow}(x) = e^{\frac{ik_x}{2}(\sigma_z - 1)}, \tag{4.19}$$

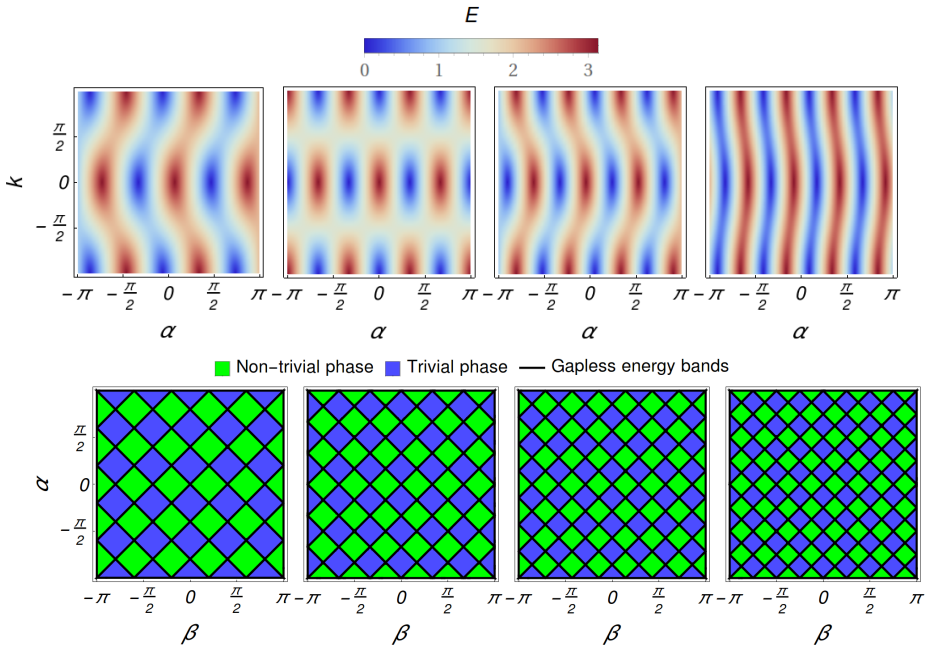

Figure 4.5: One-dimensional BDI class: Modification of energy (upper panel) as a function of momentum and rotation angle α ($\beta = \pi/3$), and C (lower panel) for subsequent steps of $T = 5, ..., 8$ from left to right. In the upper panel, each step contains only one type of boundary states. In the lower panel, the trivial (blue areas with $C > 1$), non-trivial (red areas with $C < 1$) phases, and boundary states (bold lines with $C = 1$) are marked. The places and numbers of topological phases and boundary states change step-dependently.

$$\widehat{S}_{\downarrow}(x) \quad = \quad e^{\frac{ik_x}{2}(\sigma_z+1)}. \tag{4.20}$$

It is a matter of calculation to find the eigenvalues of the protocol in Eq. (4.16) as

$$\Xi \quad = \quad \kappa_\alpha\kappa_\beta\cos(k_x) - \lambda_\alpha\lambda_\beta \pm \sqrt{[\kappa_\alpha\kappa_\beta\cos(k_x) - \lambda_\alpha\lambda_\beta]^2 - 1}, \tag{4.21}$$

and this gives us the energy bands as

$$E \quad = \quad \pm\cos^{-1}\left(\kappa_\alpha\kappa_\beta\cos(k_x) - \kappa_\alpha\kappa_\beta\right). \tag{4.22}$$

Generally speaking, the energy bands can close their gap in three ways of linearly, nonlinearly, and flatly provided the following conditions are admitted:

I) For $\sin(\frac{T\alpha}{2})\sin(\frac{T\beta}{2}) = 0$, the energy bands close their gap linearly, hence Dirac cone boundary states.

II) If $\cos(k_x)\cos(\frac{T\alpha}{2})\cos(\frac{T\beta}{2}) = 0$, the dependency of the energy bands on k_x would be eliminated. Therefore, we would have flat bands boundary states.

III) Finally, if the last two conditions are not satisfied and gap-closure happens, it would be nonlinearly, hence Fermi arc boundary states.

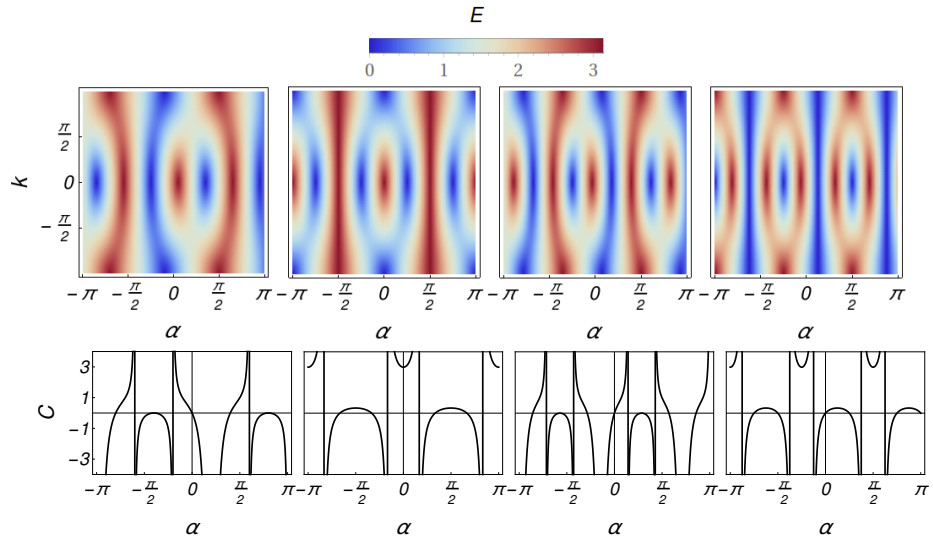

Figure 4.6: One-dimensional BDI class: Modification of energy (upper panel) as a function of momentum and rotation angle α ($\beta = (\alpha + \pi)/3$), and C (lower panel) for subsequent steps of $T = 5, ..., 8$ from left to right. In the upper panel, emergences of all three types of boundary states and cell-like structures are observed. The cells are recognized by two flat bands, two Fermi arcs, and a Dirac cone between them. In the lower panel, the trivial ($C > 1$), non-trivial ($C < 1$) phases, and boundary states are marked using C. The flat bands are located at non-zero maximums, Dirac cones at non-zero minimums, and Fermi arcs at divergent points. Another type of Fermi arc is recognized at $C = 1$.

Therefore, the three types of boundary states are simulable by the split-step protocol. If α and β are independent of each other, only one type of boundary state can be simulated in each step (see Fig. 4.5). By considering a linear relation between the rotation angles, $\beta = s_1\alpha + s_2$ with s_i being real numbers, we can simulate all three types of boundary states in a single step (see Fig. 4.6). Next, we calculate $\mathbf{n}$ as

$$\mathbf{n} = \frac{1}{\sin(E)} \begin{pmatrix} \kappa_\alpha \lambda_\beta \sin(k_x) \\ \lambda_\alpha \kappa_\beta + \kappa_\alpha \lambda_\beta \cos(k_x) \\ -\kappa_\alpha \kappa_\beta \sin(k_x) \end{pmatrix}. \tag{4.23}$$

To find CHS operator of the walk, we find $\mathbf{A} = (\kappa_\beta, 0, \lambda_\beta)$ which gives us the CHS operator in the form of

$$\widehat{\Gamma} = \begin{pmatrix} \lambda_\beta & \kappa_\beta \\ \kappa_\beta & -\lambda_\beta \end{pmatrix}. \tag{4.24}$$

To find the topological invariant, we use the Zak phase (Cardano et al., 2017). This indicates that the topological phases can be described by

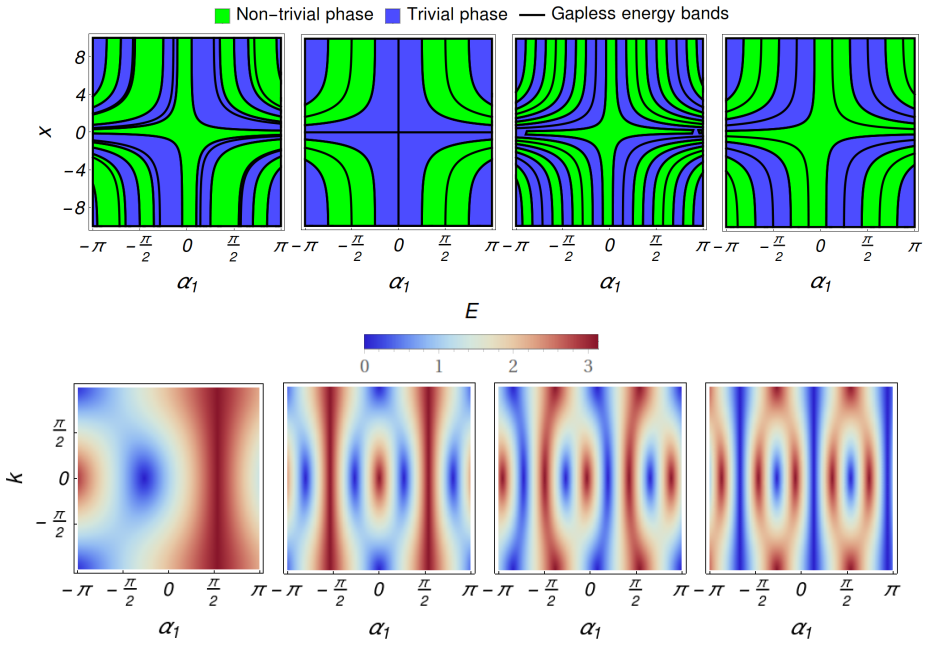

Figure 4.7: One-dimensional BDI class: In the upper panel, the trivial (blue areas with $C > 1$) and non-trivial (red area with $C < 1$) phases and boundary states (bold lines with $C = 1$) are plotted using C for subsequent steps of $T = 5, ..., 8$ from left to right with $\beta = (\alpha + \pi)/3$ and $\alpha = \alpha_1 \tanh(x/3)$. The boundary states host gapless edge states. As the step number increases, the place of edge states, and their numbers vary. In the lower panel, modification of energy as a function of momentum and rotation angle α_1 with $x = 5$ is presented. The formations of the cell-like structures are evident. The cells include all types of edge states.

$$C = \frac{\tan(\frac{T\alpha}{2})}{\tan(\frac{T\beta}{2})}, \tag{4.25}$$

if the rotation angles are linearly related. We recognize Dirac cones boundary states non-zero minimums, flat bands by non-zero maximums and Fermi arc by divergent points. There is another type of Fermi arc boundary states which occurs if $C = 1$. In case of $C > 1$, the phases are trivial whereas in case of $C < 1$, non-trivial phases are observable provided C. These cases are plotted in Fig. 4.6.

Alternatively, if the two rotation angles are independent of each other, the phase structure can be described by

$$C = \left|\frac{\tan(\frac{T\alpha}{2})}{\tan(\frac{T\beta}{2})}\right|, \tag{4.26}$$

in which for $C > 1$, the phases are trivial while for $C < 1$, the phases will be non-trivial ones (see Fig. 4.5). For $C = 1$, the energy bands close their gap. Finally, we find the group velocity as

$$V(k_x) \;=\; \pm\frac{\cos(\frac{T\alpha}{2})\cos(\frac{T\beta}{2})\sin(k_x)}{\sqrt{1-\gamma^2}}. \tag{4.27}$$

It should be noted that $n_z = -|V(k_x)|$ which indicates that the group velocity is limited to $[-1, 1]$. The group velocity characterizes the motion of a wave packet associating with the walker.

Chronologically, the coin operator $\widehat{C}_\beta$ is applied first in the split-step protocol. The CHS operator is given as a function of rotation angle β. Therefore, CHS symmetry and its properties are governed by the first coin operator that is applied on the internal states of the walker.

The emergence of $\sin(\frac{T\alpha}{2})\sin(\frac{T\beta}{2})$ term in obtained energy bands is the reason why the split-step protocol is able to simulate trivial phases as well as non-trivial ones. This term also plays a key role in the formation of different types of boundary states. Each boundary state has specific properties in the energy bands, group velocity, and its Bloch sphere presentation of $\mathbf{n}$ that distinguished it from the other boundary states (Panahiyan and Fritzsche, 2020c).

For Dirac cone boundary states, the gap-closure happens linearly. Therefore, the energy bands are linear functions of the k_x for this case. The group velocity of this boundary state is a constant function of ${}_xk$ around the gapless point and at the gapless point (see Fig. 4.8), its sign swaps from positive to negative (for $E = \pi$) or vice versa (for $E = 0$). As for the Bloch presentation of the $\mathbf{n}$ as k_x traverses $[-\pi, \pi]$, it will span the diameter of the sphere and passes the origin (see Fig. 4.9).

The Fermi arc boundary states indicate a nonlinear gap-closure, hence a nonlinear behavior for energy bands as functions of the k_x. The group velocity also presents a nonlinear behavior around the gapless point and depends on k_x. The sign of the group velocity swaps from positive to negative (for $E = \pi$) or vice versa (for $E = 0$) at gapless point (see Fig. 4.8). As for $\mathbf{n}$, it passes the origin and lies on half of the greatest circles on the Bloch sphere (see Fig. 4.9).

Finally, in the case of the flat bands, the energy bands are independent of the k_x, and therefore, the gap-closure does not just happen at one point in k_x space, rather an infinite number of points. The group velocity of this case is zero since the energy bands are independent of k_x (see Fig. 4.8). Looking at $\mathbf{n}$, it resides only in the origin of the Bloch sphere for flat bands (see Fig. 4.9).

In the split-step quantum walk, the two neighboring phases could be of the same type. In addition, two non-trivial phases with different winding numbers can not be in the neighboring of each other. Each type of boundary states has its specific phases around it which are different from the other types.

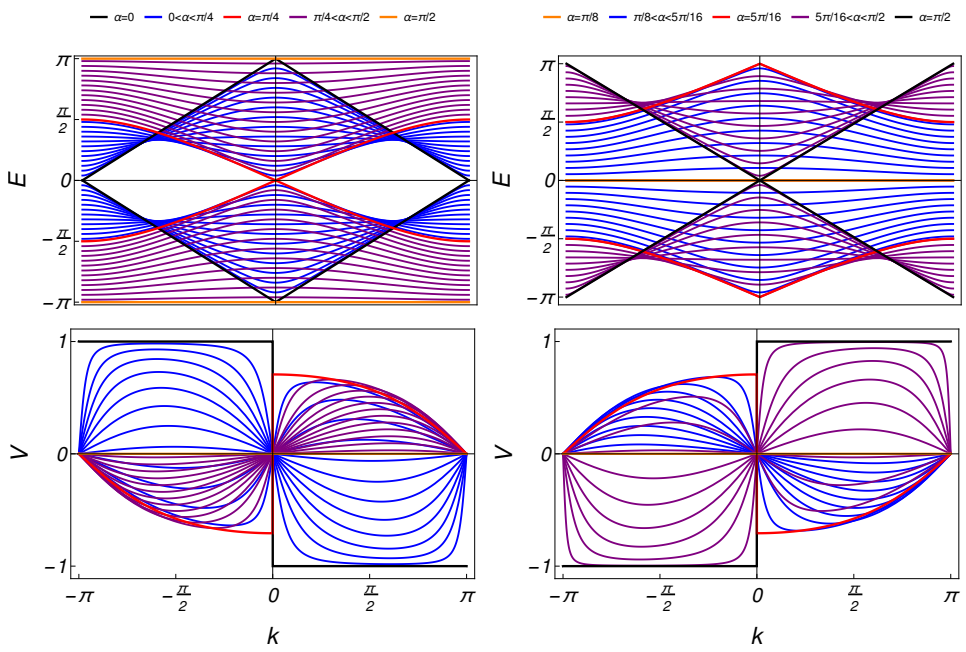

Figure 4.8: One-dimensional BDI class: Energy (upper panels) and group velocity (lower panels) for 6th (left panel) and 8th (right panel) steps with $\beta = (\alpha + \pi)/3$. The Dirac cone and Fermi arc boundary states have linear and nonlinear dispersive behaviors, respectively. The flat bands boundary states are dispersionless. Scanning α within $[0, \pi]$ confirms gap-closure through different types of boundary states.

For flat bands boundary states, the neighboring phases are non-trivial ones with the same winding number. In contrast, we observe that the Dirac cone boundary states reside at the border of two trivial phases. Finally, it is only the Fermi arc boundary states that separate two distinctive phases from one another. Therefore, the topological phase transitions in flat bands and Dirac cones are between two identical phases whereas, at Fermi arcs, we have a transition from one phase to another one.

If the rotation angles are independent of each other, only one type of boundary state can be simulated in each step. In contrast, if the two rotation angles are linearly related to each other, all three types of Dirac cone, Fermi arc, and flat bands for gapless energy bands emerge in a single step. In addition, cell-like structures start to form in specific steps (see Fig. 4.6). The cells are characterized by two flat bands boundary states acting as cell's walls. Inside these walls, we find two Fermi arcs with a Dirac cone between them. The phases inside each cell are two non-trivial phases with the winding number $+1$ and -1, and two trivial phases (see Fig. 4.9). Therefore, we observe a simulation of all three topological phases of the BDI class as well as all three types of boundary states available for one-dimensional systems in these cell-like structures.

The energy bands with Dirac cone boundary states are linearly dispersing. Whereas the Fermi arc boundary states have nonlinear dispersive behaviors. In the case of

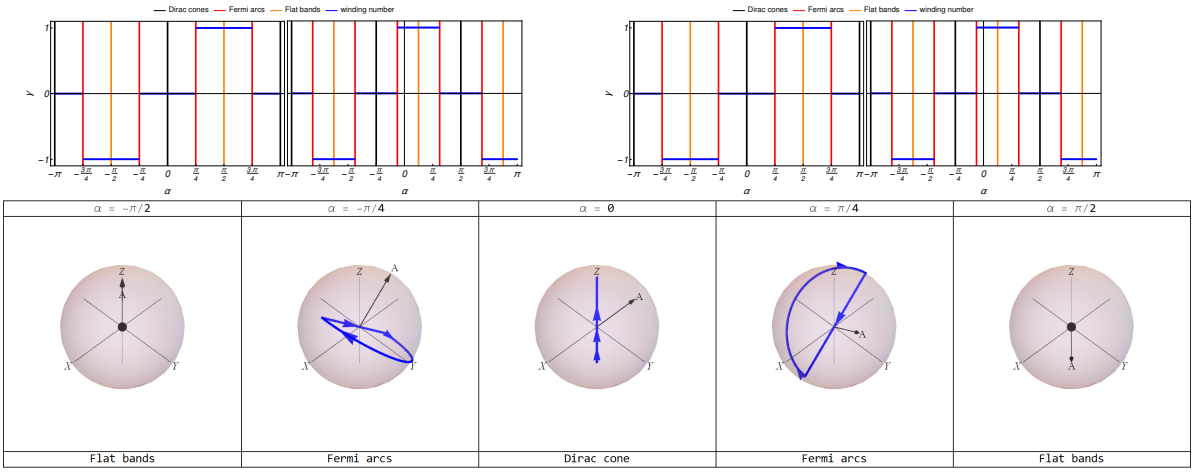

Figure 4.9: In upper left panel and upper right panel, the winding number (topological invariant) and boundary (edge) states for two cases of position-independent ($\beta = (\alpha + \pi)/3$) and position-dependent ($\alpha = \alpha_1 \tanh(x/3)$ with $x = 5$) rotation angle α are plotted. Only at neighboring of for Fermi arc boundary (edge) states, two distinct topological phases reside. In contrast, the phases around flat bands and Dirac cone boundary states are identical. The topological phases around flat bands are non-trivial ones while for Dirac cones, they are trivial ones. In lower panel, the Bloch sphere of $\mathbf{n}$ (blue curves) as k_x traverses the first Brillouin zone for 6th step with $\beta = (\alpha + \pi)/3$ is presented. For flat bands, $\mathbf{n}$ stays at the origin, for Dirac cone case, it spans the diameter of the sphere. In the case of Fermi arcs, it forms a closed loop passing the origin.

the flat bands, the energy bands are dispersionless. In fact, the group velocities that are independent of k_x are known as dispersionless transport and dependency on k_x indicates that we have dispersive transportation. The presence of flat bands indicates the existence of a macroscopic number of degenerate localized states.

The next issue is the creation of the edge states with this quantum walk. To do so, we use a position-dependent rotation angle for one of the coin operators. Such a consideration omits the translationally invariant of the quantum walk but all the three symmetries remain intact. The position dependency is considered via

$$\alpha = \frac{1}{2}(\alpha_1 + \alpha_2) + \frac{1}{2}(\alpha_1 - \alpha_2)\tanh(x/3), \tag{4.28}$$

in which we limit our study to $\alpha_2 = -\alpha_1$ giving us the position-dependent rotation angle as $\alpha = \alpha_1 \tanh(x/3)$. We consider a linear relation between the rotation angles in form of $\beta = (\alpha + \pi)/3$. This enables us to have an inhomogeneous quantum walk which can simulate topological phases with different topological invariants. We focus only on the edge states with $E = 0$ and $\pm\pi$.

We observe topologically distinct phases around boundary states in Fig. 4.9. This points out to the presence of a single localized state with energy 0 and $\pm\pi$ in the boundary state. Therefore, there are edge states with energy 0 and $\pm\pi$. In the

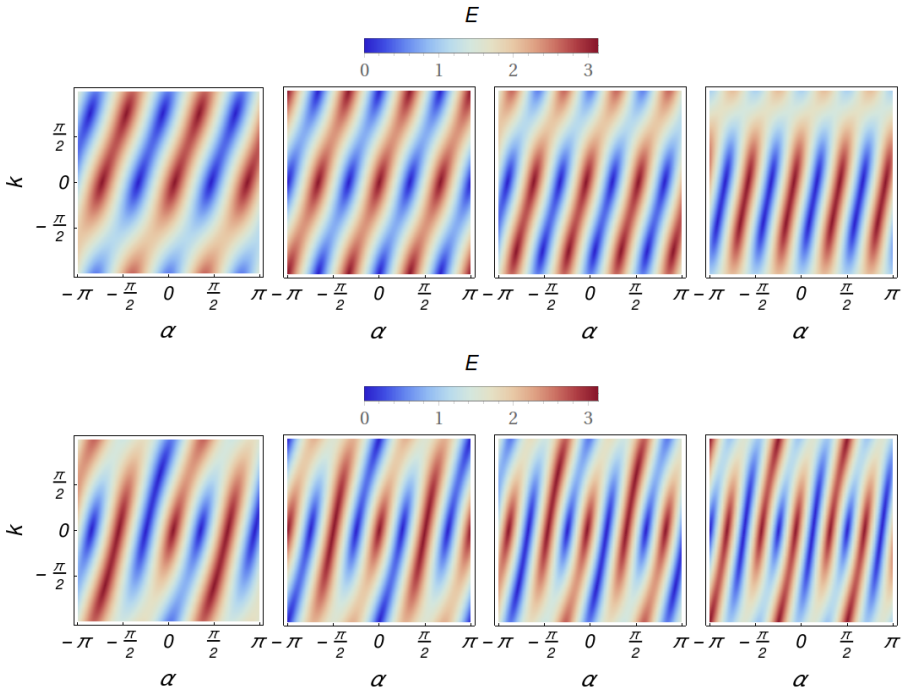

Figure 4.10: One-dimensional AIII class: Modification of energy as a function of momentum and rotation angle α for two cases of $\beta = \pi/3$ (upper panel) and $\beta = (\alpha + \pi)/3$ (lower panel). We observe a simulation of both Dirac cone and Fermi arc boundary states together. The gap-closure can happen for arbitrary values of the k_x. The numbers of the boundary states and topological phases change step-dependently.

inhomogeneous quantum walk, the position-dependent rotation angle induces the possibility of defining the topological invariant locally which could vary from one position to another one.

The question may arise whether we can simulate cell-like structures that we reported before for the inhomogeneous quantum walk in real space. To this end, we focus on a specific position ($x = 5$) and study the emergence of the cell-like structures. Plotted diagrams (Fig. 4.7) confirm the formation of these cell-like structures for the inhomogeneous quantum walk. These cells are identical to those observed before with the exception of shifting the whole structure to other values of the rotation angle (compare Figs. 4.6 and 4.7). The similarity indicates that we have a simulation of different topological phases of BDI family in real space. In addition, the created edge states could be in the forms of Fermi arc, Dirac cone, and flat bands.

One-dimensional AIII and CII classes

In AIII class, only the CHS is present. Therefore, we should build the protocol in a way that the PHS and TRS are broken. To break the PHS, we consider the rotation

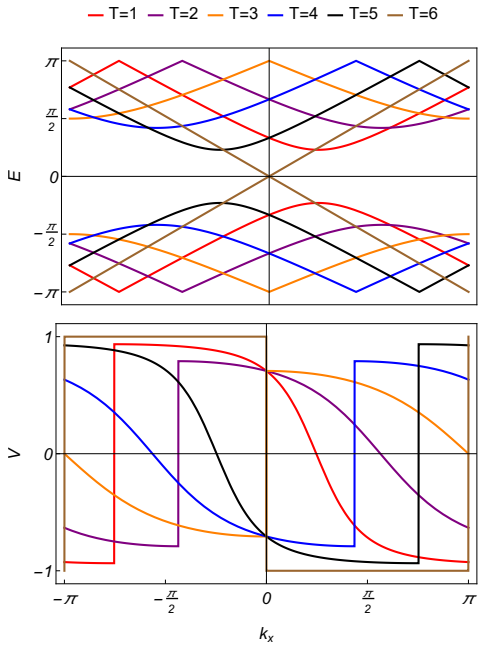

Figure 4.11: One-dimensional AIII class: Energy (up panel) and group velocity (down panel) with $\alpha = \beta = \pi/3$ for six steps. The formations of Fermi arcs happen for arbitrary values of k_x step-dependently.

angles being around a new axis of $\mathbf{\Phi} = \frac{1}{\sqrt{2}}(0, 1, 1)$. The protocol for such a walk is then given by

$$\widehat{U} = \widehat{S}_{\uparrow}(x)\widehat{C}_{\alpha}\widehat{S}_{\downarrow}(x)\widehat{C}_{\beta}, \tag{4.29}$$

in which $\widehat{C}_{\beta} = e^{-i\frac{T\beta}{2}\mathbf{\Phi}.\sigma}$ and likewise $\widehat{C}_{\alpha}$ are step-dependent coin operators around the new axis. The shift operators are exactly the same as those used in simulation of the BDI class, hence $\widehat{S}_{\downarrow}(x) = e^{\frac{ik_x}{2}(\sigma_z+1)}$ and $\widehat{S}_{\uparrow}(x) = e^{\frac{ik_x}{2}(\sigma_z-1)}$. The energy bands for the quantum walk with this protocol are found as

$$\begin{aligned} E = \pm\cos^{-1}\Bigg(& -\frac{1}{2}\lambda_{\alpha}\lambda_{\beta}[1+\cos(k_x)] + \kappa_{\alpha}\kappa_{\beta}\cos(k_x) + \\ & \frac{1}{\sqrt{2}}\sin(\frac{T\alpha}{2}+\frac{T\beta}{2})\sin(k_x)\Bigg). \end{aligned} \tag{4.30}$$

According to the obtained energy bands, we can highlight two issues:

I) If we set $\alpha = \beta = \pm(2c+1)\pi/T$, the energy bands would be nonlinear functions of the k_x, hence Fermi arc boundary states.

II) In case of $\alpha = \beta = \pm 2c\pi/T$, the energy bands reduce to $E = \pm k_x$, which indicates Dirac cone boundary states.

To find $\mathbf{n}$, we use the protocol of the quantum to find the components of $\mathbf{d}$ as

$$\begin{aligned} d_x &= \frac{\lambda_\beta}{2}[\sqrt{2}\kappa_\alpha \sin(k_x) + \lambda_\alpha(1-\cos(k_x))], \\ d_y &= \frac{\lambda_\alpha \kappa_\beta}{\sqrt{2}} + \frac{\lambda_\beta}{2}[\lambda_\alpha \sin(k_x) + \sqrt{2}\kappa_\alpha \cos(k_x)], \\ d_z &= \frac{1}{2}[\lambda_\alpha \lambda_\beta \sin(k_x) - 2\kappa_\alpha \kappa_\beta] + \frac{1}{\sqrt{2}} \sin(\frac{T(\alpha+\beta)}{2}) \cos(k_x). \end{aligned} \tag{4.31}$$

To Build the CHS operator, we find $\mathbf{A}$ perpendicular to $\mathbf{n}$ as

$$\mathbf{A} = \begin{pmatrix} \kappa_\beta \\ -\lambda_\beta/\sqrt{2} \\ \lambda_\beta/\sqrt{2} \end{pmatrix}. \tag{4.32}$$

The absence of the PHS and the presence of CHS enforce the TRS to be absent. This is because, if two of these symmetries are present, the existence of the third one is guaranteed. The group velocity for this quantum walk is obtained as $V(k_x) = \pm n_z(k_x)$.

To build the protocol simulating CII class, we use the AIII protocol and the method of doubling procedure. In the doubling procedure, we consider the walker with two internal states to have two additional internal states which we call flavor. We denote these flavors by indexes A and B. The protocol of the quantum walk for simulating CII class should be diagonal in the flavor index

$$\widehat{U} = \begin{pmatrix} \widehat{U}_b & 0 \\ 0 & \widehat{U}_b^t \end{pmatrix}, \tag{4.33}$$

in which $\widehat{U}_b$ is the protocol given in Eq. (4.29) for simulation of the AIII class. $\widehat{U}_b$ and $\widehat{U}_b^t$ acts on flavors A and B, respectively and t stands for transpose. The new protocol has three symmetries of CHS, PHS, and TRS. The CHS operator is obtained by CHS operator of the AIII protocol in form of $\widehat{\Gamma} = diag[\widehat{\Gamma}, \widehat{\Gamma}^*]$ and it squares to $+\widehat{I}$. The TRS operator is given by $\widehat{\mathcal{T}} = i\tau_y \widehat{K}$ in which τ_y is a Pauli matrix. It should be noted that τ_i are Pauli matrices acting on flavors A and B while Pauli matrices of σ_i act on the other two internal states. The TRS operator squares to $-\widehat{I}$. The PHS operator is then obtained by using the CHS and the TRS operators $\widehat{\mathcal{P}} = \widehat{\Gamma}\widehat{\mathcal{T}}$ and it squares to $-\widehat{I}$. Therefore, it is evident that Hamiltonian has the requirements to simulate topological phases of CII class in one dimension.

The first noticeable issue for the protocol of AIII is that gap-closure can happen at arbitrary values of the k_x (see Figs. 4.10 and 4.11). This is in contrast to the

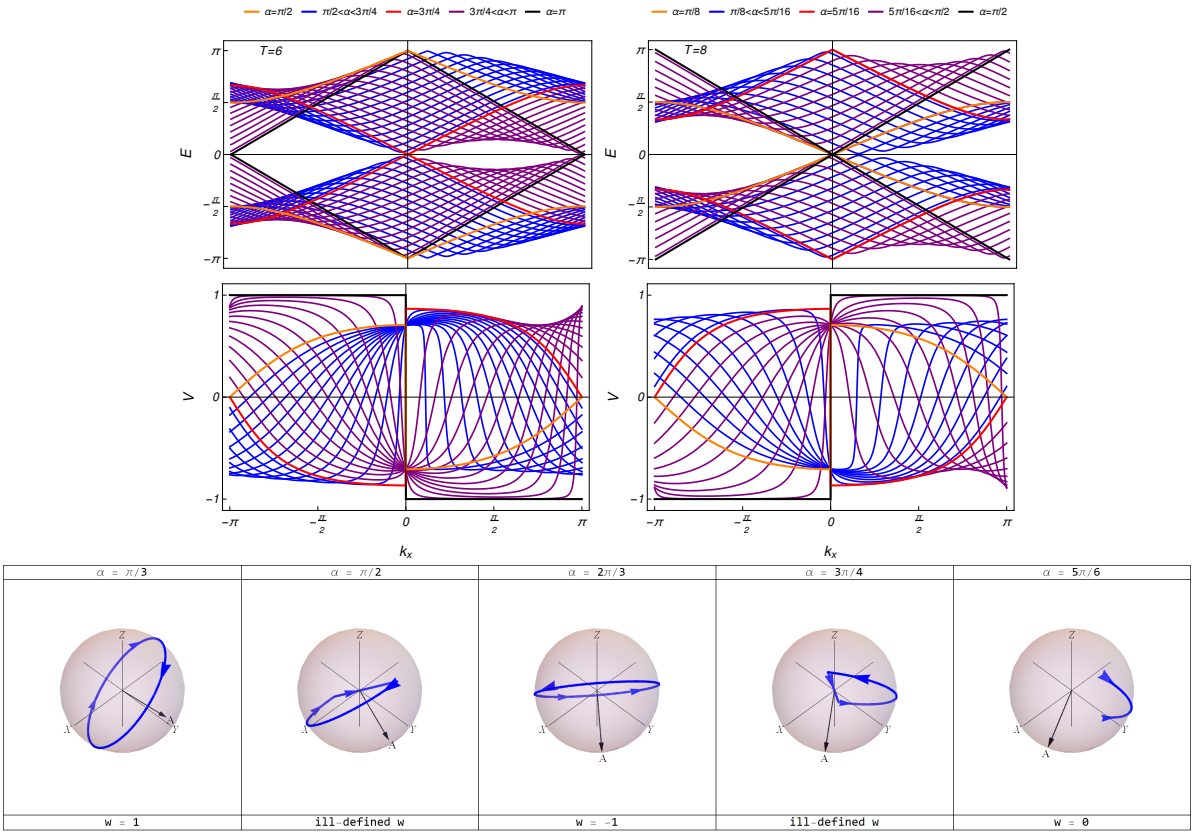

Figure 4.12: One-dimensional AIII class: Energy (up panels) and group velocity (middle panels) for $T = 6th$ (up left panel) and $8th$ (up right panel) with $\beta = (\alpha + \pi)/3$. In energy diagrams, we observe the phase structure as a function of the rotation angle. In group velocity diagrams, we observe nonlinear and linear modifications of group velocity for Fermi arc and Dirac cone boundary states, respectively. The swapping of the group velocity's sign to the opposite happens at gapless points of energy bands. In the lower panel, we have Bloch sphere presentation of $\mathbf{n}$ (blue curves) as k_x traverses the first Brillouin zone for $T = 6th$ with $\beta = (\alpha + \pi)/3$. The closed loops indicate non-trivial topological phases with the clockwise winding direction giving $\gamma = -1$ and counterclockwise $\gamma = 1$. Trivial phases have open loops and for the boundary states, $\mathbf{n}$ passes the origin.

protocols for BDI and D classes in which the gap-closure could happen in only a limited number of the k_x. The boundary states are in the forms of Dirac cone and Fermi arcs and the behavior of the group velocity for this protocol is similar to what we observed in the case of BDI class (see Fig. 4.12).

One-dimensional D and DIII classes

For the simulation of the one-dimensional D class topological phases, the Hamiltonian should retain only the PHS symmetry while the CHS and the TRS are absent. To ensure the presence of the PHS, we consider the coin operators to rotate internal states in the xy plane. To break the CHS, we include an additional shift operator

to the protocol. The protocol of the quantum walk for simulation of D class is then given by

$$\widehat{U} = \widehat{S}_{\uparrow}(x)\widehat{C}_{\alpha}\widehat{S}_{\downarrow}(x)\widehat{C}_{\beta}\widehat{S}_{\uparrow\downarrow}(x), \tag{4.34}$$

in which the presence of $\widehat{S}_{\uparrow\downarrow}(x)$ breaks the CHS. Using the protocol, it is a matter of calculation to find the energy bands in the form of

$$E = \pm\cos^{-1}\Big(\kappa_{\alpha}\kappa_{\beta}[\cos^2(k_x) - \sin^2(k_x)] - \cos(k_x)\lambda_{\alpha}\lambda_{\beta}\Big). \tag{4.35}$$

Three specific behaviors can be specified for energy bands:

I) If we consider $\alpha = \beta = \pm(2c+1)\pi/T$, the gap-closure happens linearly and simultaneously only at $k_x = 0$ and $\pm\pi$ (type one). On the other hand, for $\alpha = \beta = \pm 2c\pi/T$, the energy bands close their gap linearly and simultaneously at $k_x = 0$, $\pm\pi/2$ and $\pm\pi$ (type two). Therefore, we have two types of Dirac cone boundary states.

II) Provided that $\beta = \pm(2c+1)\pi/T$ and $\alpha = \pm 2c\pi/T$, energy bands become independent of k_x and constant, $E = \pm\pi/2$. Therefore, the energy bands are flat bands but not flat bands boundary states.

III) If the first condition is not admitted, the gap-closure will be nonlinearly, therefore, the boundary states would be in the form of Fermi arc. To find $\mathbf{n}$, we calculate the components of $\mathbf{d}$ as

$$\begin{aligned} d_x &= -\lambda_{\alpha}\kappa_{\beta}\sin(k_x), \\ d_y &= \lambda_{\alpha}\kappa_{\beta}\cos(k_x) + \kappa_{\alpha}\lambda_{\beta}, \\ d_z &= \sin(k_x)\lambda_{\alpha}\lambda_{\beta} - 2\kappa_{\alpha}\kappa_{\beta}\cos(k_x)\sin(k_x). \end{aligned} \tag{4.36}$$

The obtained $\mathbf{n}$ does not lie on a plane containing the origin of the Bloch sphere for variation of the k_x in the first Brillouin zone. Since the Hamiltonian does not have the CHS, one can conclude that the TRS is also absent for the effective Hamiltonian. The matrix of the protocol has real-valued elements, therefore, the PHS operator would be the complex conjugate operator, $\widehat{\mathcal{P}} = \widehat{K}$. Finally, the group velocity is calculated by

$$V(k_x) = \pm\frac{\sin(k_x)\lambda_{\alpha}\lambda_{\beta} - 4\kappa_{\alpha}\kappa_{\beta}\cos(k_x)\sin(k_x)}{\sqrt{1 - [\kappa_{\alpha}\kappa_{\beta}[\cos^2(k_x) - \sin^2(k_x)] - \cos(k_x)\lambda_{\alpha}\lambda_{\beta}]^2}}. \tag{4.37}$$

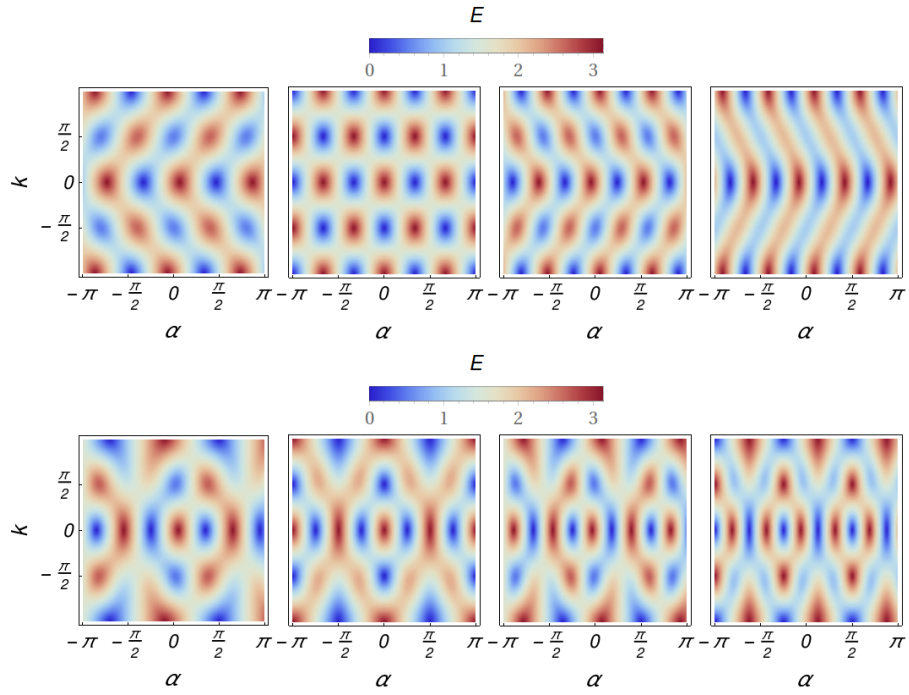

Figure 4.13: One-dimensional D class: Modification of energy as a function of momentum and rotation angle α for two cases of $\beta = \pi/3$ (upper panel) and $\beta = (\alpha+\pi)/3$ (lower panel). In the upper panel, only one type of boundary states (Dirac cone or Fermi arc) can be simulated in each step, while in the lower panel, we observe a simulation of the two types of boundary states together. There are two types of Dirac cone boundary states: the first type has gapless points at $k_x = 0$ and $\pm\pi$ while type two has additionally at $k_x = \pm\pi/2$. The size of topological phases step-dependently decreases, hence increasing numbers of topological phases and boundary states.

The method to build the protocol for simulating DIII is similar to the protocol of the CII. In other words, we use the protocol given in Eq. (4.34) for simulating D class with doubling procedure to obtain the protocol for DIII in the form of

$$\widehat{U} = \begin{pmatrix} \widehat{U}_a & 0 \\ 0 & \widehat{U}_a^t \end{pmatrix}, \tag{4.38}$$

in which $\widehat{U}_a$ is given by Eq. (4.34), $\widehat{U}_a$ and $\widehat{U}_a^t$ act on flavors A and B. The resultant protocol has the three symmetries of CHS, PHS and TRS with $\widehat{\mathcal{P}}^2 = \widehat{\Gamma}^2 = +\widehat{I}$ and $\widehat{\mathcal{T}}^2 = -\widehat{I}$ which are necessary conditions for simulation of the DIII class of topological phases in one dimension.

The protocol of the quantum walk with only PHS simulates only Dirac cone and Fermi arc boundary states. Similar to the split-step protocol of BDI class, if the rotation angles in D class are independent of each other, only one type of the boundary states would be observed for the simulation (see Fig. 4.13). Whereas, by

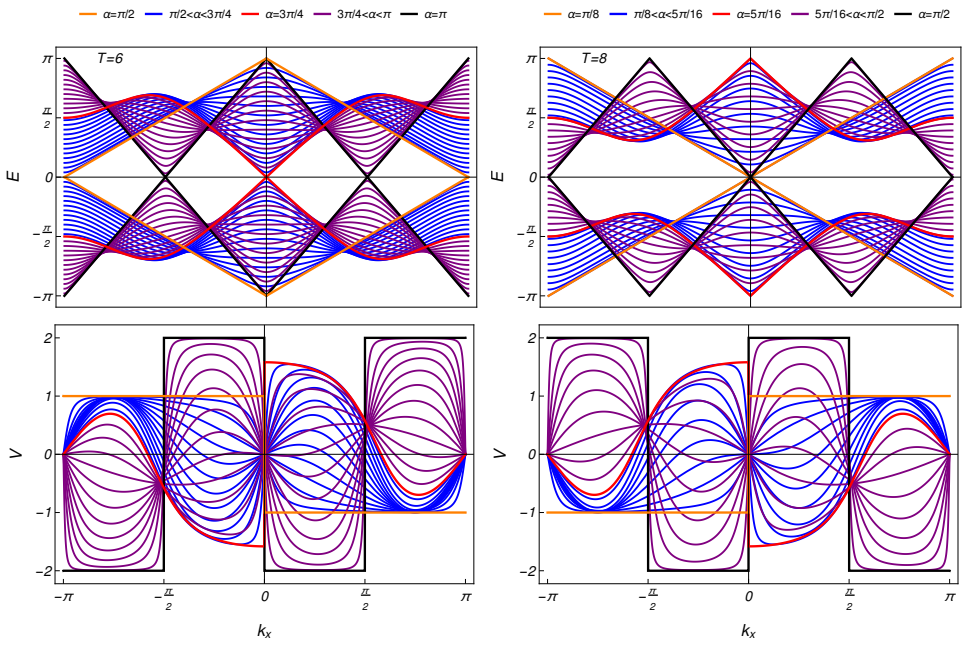

Figure 4.14: One-dimensional D class: Energy (upper panels) and group velocity (lower panels) for $T = 6$ (left panel) and $T = 8$ (right panel) with $\beta = (\alpha + \pi)/3$. Scanning the α through a limited range shows the simulations of type one and two Dirac cone, and Fermi arc boundary states. The place of topological phases and boundary states change step-dependently. In the lower panel, the group velocity around type one Dirac cone boundary state approximates to $\approx \pm 1$ while for the type two Dirac cone, it approximates to $\approx \pm 2$. For all of these boundary states, the sign of the group velocity swaps at the gapless point.

considering the rotation angles being a linear function of each other, we have the simulation of both Fermi arc and Dirac cone boundary states in a single step. In addition, a characteristic behavior would emerge which is the reminiscence of the cell-like structure observed before. The new structures contain two Dirac cones as the exterior of the structure and two Fermi arcs with an additional Dirac cone located between them. The Dirac cone boundary states of the exterior are different from the one between the Fermi arcs (see Fig. 4.13).

The first issue about the group velocity is its value which spans between $[-2, 2]$ (see Fig. 4.14). For Fermi arc boundary state, the group velocity is a nonlinear function of the k_x and it swaps sign at the phase transition point. For the Dirac cone boundary state, the behavior of the group velocity depends on the type of the Dirac cone boundary state. For type one, the group velocity is fixed around the phase transition point to ± 1 and at the phase transition point, it swaps from $+1$ to -1 or vice versa. In contrast, for type two Dirac cone, the group velocity is fixed at ± 2 and the swapping at phase transition point happens between $+2$ to -2 or the opposite.

4.2.2 *Topological phenomena in two dimensions*

Now, we turn our attentions to build the protocols to simulate observed topological phases in two dimensions. For two dimensional systems, the topological phases are observed for A, AII, C, D, and DIII classes. While this is the case, it was shown that for Floquet operators describing the topological phases, it is possible to find special phenomena such as multicriticality where phase boundaries cross each other (Thakurathi et al., 2013; Molignini et al., 2018). Therefore, we also present the protocols for BDI class which according to a non-driven system admits only trivial phases in two dimensions.

Two-dimensional BDI class

For this class, we introduce two protocols including simple- and split-step ones. The simple-step protocol is given by

$$\widehat{U} \;=\; \widehat{S}_{\uparrow\downarrow}(x,y)\widehat{C}_{\theta}. \tag{4.39}$$

The shift operator includes two other shift operators

$$\widehat{S}_{\uparrow\downarrow}(x,y) \;=\; \widehat{S}_{\uparrow\downarrow}(y)\widehat{S}_{\uparrow\downarrow}(x), \tag{4.40}$$

where

$$\widehat{S}_{\uparrow\downarrow}(x) \;=\; |\uparrow\rangle\langle\uparrow| \otimes \sum_{x,y} |x+1,y\rangle\langle x,y| + |\downarrow\rangle\langle\downarrow| \otimes \sum_{x,y} |x-1,y\rangle\langle x,y|\,, \tag{4.41}$$

$$\widehat{S}_{\uparrow\downarrow}(y) \;=\; |\uparrow\rangle\langle\uparrow| \otimes \sum_{x,y} |x,y+1\rangle\langle x,y| + |\downarrow\rangle\langle\downarrow| \otimes \sum_{x,y} |x,y-1\rangle\langle x,y|\,, \tag{4.42}$$

which by using the Fourier transformation, we rewrite them as $\widehat{S}_{\uparrow\downarrow}(x) = e^{ik_x\sigma_z}$ and $\widehat{S}_{\uparrow\downarrow}(y) = e^{ik_y\sigma_z}$.

The energy bands for this protocol are obtained as

$$E \;=\; \pm\cos^{-1}\Big(\kappa_{\theta}\cos(k_x+k_y)\Big). \tag{4.43}$$

The energy bands close their gap only at $E = 0$ and $\pm\pi$ which we can find analytically as

$$\theta_{E=\pi} \;=\; \frac{\pm 2\cos^{-1}[-\sec(k_x+k_y)] + 4\pi c}{T}, \tag{4.44}$$

$$\theta_{E=0} = \frac{\pm 2\cos^{-1}[\sec(k_x + k_y)] + 4\pi c}{T}. \tag{4.45}$$

The energy bands will be in the form of flat bands with $E = \frac{\pi}{2}$ provided that the rotation angle admits

$$\theta_{E=\pi/2} = \frac{4\pi c \pm \pi}{T}. \tag{4.46}$$

It is straightforward to find $\mathbf{n}$ in the form of

$$\mathbf{n} = \frac{1}{\sin(E)} \begin{pmatrix} \kappa_\theta \sin(k_x + k_y) \\ \lambda_\theta \cos(k_x + k_y) \\ -\kappa_\theta \sin(k_x + k_y) \end{pmatrix}. \tag{4.47}$$

The present protocol has three symmetries of CHS, PHS, and TRS. Since the elements of the protocol's matrix are real-valued, the PHS is present for this protocol with the complex conjugate operator being the PHS operator. To find the CHS, we first introduce $\mathbf{A}$ in the form of

$$\mathbf{A} = \begin{pmatrix} \kappa_\theta \\ 0 \\ \lambda_\theta \end{pmatrix}, \tag{4.48}$$

which gives us the CHS operator as

$$\widehat{\Gamma} = \begin{pmatrix} \lambda_\theta & \kappa_\theta \\ \kappa_\theta & -\lambda_\theta \end{pmatrix}. \tag{4.49}$$

The presence of the TRS is then guaranteed and its operator is given by $\widehat{\Gamma}\widehat{K}$. Since all three operators of the symmetries square to $+\widehat{I}$, BDI class should be simulated by this protocol in two dimensions. The group velocity for this quantum walk would have two components in x and y directions

$$V(k_x) = V(k_y) = \pm \frac{\cos(\frac{T\theta}{2})\sin(k_x + k_y)}{\sqrt{1 - [\cos(\frac{T\theta}{2})\cos(k_x + k_y)]^2}}, \tag{4.50}$$

in which we have used $V(k_x) = \partial E/\partial k_x$ and likewise for $V(k_y)$.

In two-dimensional cases, the $\mathbf{n}$ maps a small area on a two-dimensional torus to a small area on a Bloch sphere (Kitagawa et al., 2012). The winding number is no

longer the topological invariant for the two-dimensional quantum walk. In contrast, an integer number known as the Chern number is the topological invariant. The Chern number measures the number of times that $\mathbf{n}$ covers the Bloch sphere as k_x and k_y traverse the first Brillouin zone. The Chern number is calculated by

$$\mathcal{C} = \int_{-\pi}^{\pi} \left(\frac{\partial \mathbf{n}}{\partial k_x} \times \frac{\partial \mathbf{n}}{\partial k_y} \right) \cdot \mathbf{n} \frac{d^2k}{4\pi}. \tag{4.51}$$

It should be noted that instead of $\mathbf{n}$, one can also plot the Bloch sphere presentation of $\mathbf{d}$ for variations of k_x and k_y through the first Brillouin zone. If $\mathbf{d}$ covers the origin and it does not pass the origin, then the Chern number is non-zero and we have a non-trivial phase. If it does not cover the origin, then we have a trivial phase with Chern number zero. Finally, $\mathbf{d}$ passing the origin represents a boundary state or gapless energy bands. For the protocol in Eq. (4.39), the Chern number is equal to 0 for obtained $\mathbf{n}$.

Next, we build up the split-step protocol for BDI class in two dimensions in the form of

$$\widehat{U} \;=\; \widehat{S}_{\uparrow\downarrow}(y)\widehat{C}_\alpha \widehat{S}_{\uparrow\downarrow}(x)\widehat{C}_\beta, \tag{4.52}$$

in which a single step of the quantum walk includes rotation of the internal states by $\widehat{C}_\beta$, then a displacement in x space with $\widehat{S}_{\uparrow\downarrow}(x)$, an additional rotation of internal states with $\widehat{C}_\alpha$ and finally, a displacement of its position in y space with $\widehat{S}_{\uparrow\downarrow}(y)$. The coin operators are given in Eqs. (4.17) and (4.18), while the shift operators in complex space of k are $\widehat{S}_{\uparrow\downarrow}(x) = e^{ik_x\sigma_z}$ and $\widehat{S}_{\uparrow\downarrow}(y) = e^{ik_y\sigma_z}$. The energy bands of the effective Hamiltonian are found as

$$\begin{aligned} E \;=\; \pm\cos^{-1}\Bigg(& \cos(k_x+k_y)\cos(\frac{T\alpha}{2})\cos(\frac{T\beta}{2}) - \\ & \cos(k_x-k_y)\sin(\frac{T\alpha}{2})\sin(\frac{T\beta}{2}) \Bigg). \end{aligned} \tag{4.53}$$

For these energy bands, we find that:

I) If $\alpha = \beta = \pm 2c\pi/T$, then energy bands will linearly depend on k_x and k_y given by $E = \pm(k_x + k_y)$, hence Dirac cone boundary states.

II) For $\alpha = \beta = \pm(2c+1)\pi/T$, energy bands become linear functions of k_x and k_y given by $E = \pm\cos^{-1}(-\cos(k_x - k_y))$. This indicates possible Dirac cone boundary states.

III) Provided that $\alpha = \pm(2c+1)\pi/T$ and $\beta = \pm 2c\pi/T$ or vice versa, the energy bands reduce to flat bands with $E = \pm\pi/2$.

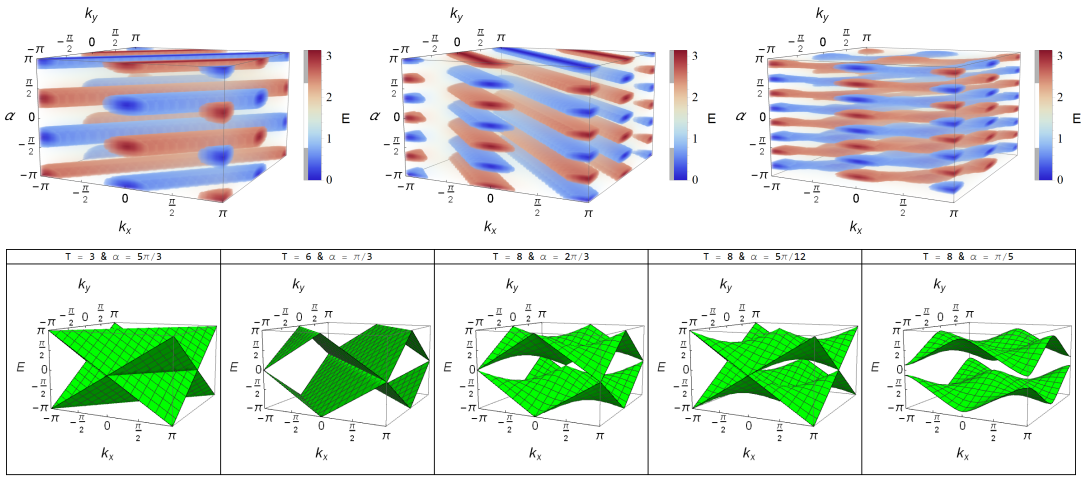

Figure 4.15: Two-dimensional BDI class: Energy as a function of rotation angle and momenta for $\beta = \pi/3$ with $T = 3$ (upper left panel), $T = 6$ (upper middle panel) and $T = 8$ (upper right panel). In the lower panel, we observe different types of boundary states in three different steps as well as a case of trivial phase.

Next, we find the $\mathbf{d}$ which enables us to calculate $\mathbf{n}$

$$\begin{aligned} d_x &= \sin(k_x + k_y)\cos(\frac{T\alpha}{2})\sin(\frac{T\beta}{2}) - \sin(k_x - k_y)\sin(\frac{T\alpha}{2})\cos(\frac{T\beta}{2}), \\ d_y &= \cos(k_x + k_y)\cos(\frac{T\alpha}{2})\sin(\frac{T\beta}{2}) + \cos(k_x - k_y)\sin(\frac{T\alpha}{2})\cos(\frac{T\beta}{2}), \\ d_z &= \sin(k_x - k_y)\sin(\frac{T\alpha}{2})\sin(\frac{T\beta}{2}) - \sin(k_x + k_y)\cos(\frac{T\alpha}{2})\cos(\frac{T\beta}{2}). \end{aligned} \tag{4.54}$$

The protocol has three symmetries of CHS and PHS and TRS. The operators of symmetries are identical to those obtained for the split-step protocol simulating BDI class in one dimension. Therefore, we have a protocol that simulates BDI class in two dimensions. It is a matter of calculation to find the components of the group velocity as

$$V(k_x) = \pm\frac{\sin(k_x - k_y)\sin(\frac{T\alpha}{2})\sin(\frac{T\beta}{2}) - \sin(k_x + k_y)\cos(\frac{T\alpha}{2})\cos(\frac{T\beta}{2})}{\sqrt{1-\gamma^2}}, \tag{4.55}$$

$$V(k_y) = \pm\frac{-\sin(k_x - k_y)\sin(\frac{T\alpha}{2})\sin(\frac{T\beta}{2}) - \sin(k_x + k_y)\cos(\frac{T\alpha}{2})\cos(\frac{T\beta}{2})}{\sqrt{1-\gamma^2}}. \tag{4.56}$$

For both of the BDI protocols in two dimensions, we observe a new type of flat bands boundary state. In the one-dimensional case, flat bands boundary states emerged as energy bands become independent of the k_x (see Fig. 4.15). In contrast, for the two-dimensional case with a split-step protocol, it is possible to have flat bands provided that $k_x + k_y = 0$ and $\pm\pi$. Therefore, flat bands are formed when energy bands depend on both momenta. If we fix one of the momenta and varies the other one through the first Brillouin zone, the Dirac cone boundary states would be observed for both

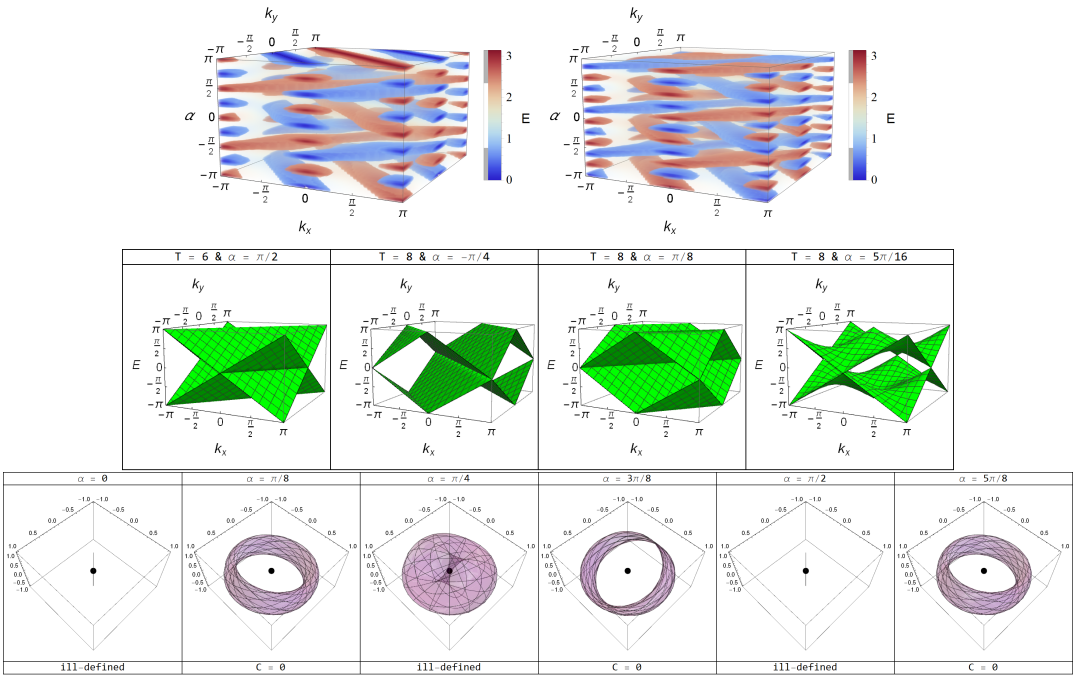

Figure 4.16: Two-dimensional BDI class: Energy (upper panels) as a function of rotation angle and momenta for $\beta = (\alpha + \pi)/3$, $T = 6$ (left upper panel) and $T = 8$ (right upper panel). In the middle panel, we observe Dirac cones (provided $k_y = -\pi$) and flat bands (provided k_x and k_y traverse first Brillouin zone) and Fermi arc boundary states. In right upper panel, a cell-like structure is emerged for $\alpha \in [-\pi/2, \pi/2]$. The cell contains two flat bands, two Fermi arcs, and one additional flat bands. Each cell also contains Dirac cones provided $k_y = -\pi$. In the lower panel, $\mathbf{d}$ is plotted for the first Brillouin zone. For gapless energy bands, $\mathbf{d}$ passes origin while for gapped phases, it goes around it. The phases are trivial since $\mathbf{d}$ can not cover the origin completely.

simple- and split-step protocols. For simple-step protocol, Fermi arc boundary states are absent while in split-step protocol, due to $\cos(k_x - k_y)\sin(\frac{T\alpha}{2})\sin(\frac{T\beta}{2})$, Fermi arc boundary states are observed as well. Therefore, the split-step protocol admits the three types of boundary states while simple-step only simulates two of them.

The cell-like structure that was found for one-dimensional protocols of BDI class can be obtained here as well. This is done if one of the rotation angles is a linear function of the other one $\beta = s_1\alpha + s_2$ (see Fig. 4.16). The cells in two dimensions contain two flat bands boundary states playing the role of the cell's walls, two Fermi arc boundary states, and one additional flat bands boundary state located between the Fermi arc boundary states. The flat bands boundary state between the Fermi arcs differs from those of the cell's walls. If we fix one of the momenta and let the other one varies, we also find Dirac cone boundary states in the cells. Therefore, a single cell contains all three types of boundary states. As a final remark, we should point out that Chern number for this case is also zero indicating simulation of the only trivial phases.

Two-dimensional A, AII and C classes

A class of the topological phases requires absences of all three symmetries. To this end, we first break the PHS by performing at least one of the rotations around the $\mathbf{\Phi}$ axis. To break the CHS, we include an additional shift operator to the protocol of the quantum walk. This results in the following protocol

$$\widehat{U} = \widehat{S}_{\uparrow\downarrow}(y)\widehat{C}_{\gamma}\widehat{S}_{\uparrow\downarrow}(x)\widehat{C}_{\alpha}\widehat{S}_{\uparrow\downarrow}(x,y)\widehat{C}_{\beta}, \tag{4.57}$$

in which due to $\widehat{C}_{\alpha}$ and $\widehat{S}_{\uparrow\downarrow}(x,y)$, the PHS and CHS are broken, respectively. As for the coin operators, $\widehat{C}_{\alpha} = e^{-i\frac{T\alpha}{2}\mathbf{\Phi}.\sigma}$, $\widehat{C}_{\beta}$ is given in Eq. (4.18) and $\widehat{C}_{\gamma}$ is likewise. Using the protocol, we can find the energy bands as

$$\begin{aligned} E = \pm\cos^{-1}\Bigg(&\frac{\sqrt{2}\lambda_{\alpha}}{2}[\kappa_{\beta}\kappa_{\gamma}\sin(2k_x+2k_y)-\lambda_{\beta}\kappa_{\gamma}-\kappa_{\beta}\lambda_{\gamma}\cos(2k_y)-\lambda_{\beta}\lambda_{\gamma}\sin(2k_x)]+\\ &\kappa_{\alpha}[\kappa_{\beta}\kappa_{\gamma}\cos(2k_x+2k_y)-\lambda_{\beta}\lambda_{\gamma}\cos(2k_x)]\Bigg), \end{aligned} \tag{4.58}$$

in which the energy bands' behaviors can be described in the following cases:

I) If $\alpha = \beta = \gamma = \pm 2c\pi/T$, the energy bands become linear functions of the momenta, hence Dirac cone boundary states can be resulted.

II) In case of $\beta = \pm 2c\pi/T$ with $\alpha = \gamma = \pm(2c+1)\pi/T$, the energy bands become independent of k_y and they will be linear functions of the k_x.

III) By setting $\gamma = \pm 2c\pi/T$ with $\alpha = \beta = \pm(2c+1)\pi/T$, the energy bands will be independent of momenta and flat bands with $E = \pm\pi/4$ would be resulted.

It is a matter of calculation to find the $\mathbf{d}$ as

$$\begin{aligned} d_x &= \frac{\sqrt{2}\lambda_{\alpha}}{2}[\kappa_{\beta}\lambda_{\gamma}\cos(2k_x)-\lambda_{\beta}\kappa_{\gamma}\cos(2k_x+2k_y)-\lambda_{\beta}\lambda_{\gamma}\sin(2k_y)]+\\ &\quad\kappa_{\alpha}[\lambda_{\beta}\kappa_{\gamma}\sin(2k_x+2k_y)-\kappa_{\beta}\lambda_{\gamma}\sin(2k_x)],\\ d_y &= \frac{\sqrt{2}\lambda_{\alpha}}{2}[\kappa_{\beta}\kappa_{\gamma}+\kappa_{\beta}\lambda_{\gamma}\sin(2k_x)+\lambda_{\beta}\kappa_{\gamma}\sin(2k_x+2k_y)-\lambda_{\beta}\lambda_{\gamma}\cos(2k_y)]+\\ &\quad\kappa_{\alpha}[\kappa_{\beta}\lambda_{\gamma}\cos(2k_x)+\lambda_{\beta}\kappa_{\gamma}\cos(2k_x+2k_y)],\\ d_z &= \frac{\sqrt{2}\lambda_{\alpha}}{2}[\kappa_{\beta}\kappa_{\gamma}\cos(2k_x+2k_y)+\kappa_{\beta}\lambda_{\gamma}\sin(2k_y)+\lambda_{\beta}\lambda_{\gamma}\cos(2k_x)]-\\ &\quad\kappa_{\alpha}[\lambda_{\beta}\lambda_{\gamma}\sin(2k_x)+\kappa_{\beta}\kappa_{\gamma}\sin(2k_x+2k_y)]. \end{aligned} \tag{4.59}$$

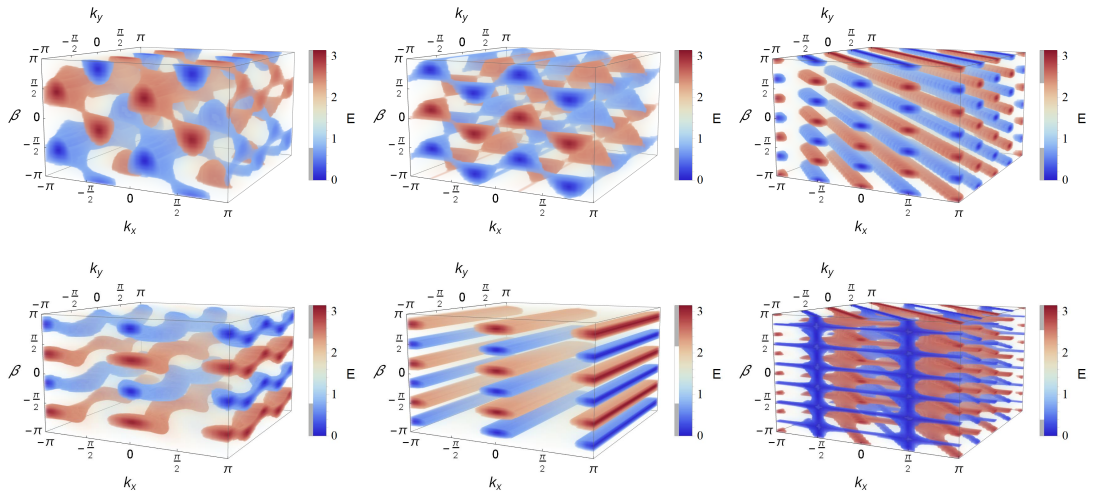

Figure 4.17: Two-dimensional A (upper panel) and D (lower panel) classes: Modification of energy with $\alpha = \pi/3$ and $\gamma = \pi/4$ for subsequent steps of $T = 2$, 3 and 6. The structures of the simulated topological phenomena change step-dependently for both classes. Usually, each step includes both Dirac cone and Fermi arc boundary states with characteristic flat bands boundary states except for $T = 3$ of D class.

Next, we find the components of the group velocity

$$V(k_x) = \pm \sin(E)^{-1}\Big(2\kappa_\alpha\lambda_\beta\lambda_\gamma \sin(2k_x) + \sqrt{2}\lambda_\alpha\kappa_\beta\kappa_\gamma \cos(2k_x + 2k_y) - 2\kappa_\alpha\kappa_\beta\kappa_\gamma \sin(2k_x + 2k_y) - \sqrt{2}\lambda_\alpha\lambda_\beta\lambda_\gamma \cos(2k_x)\Big), \tag{4.60}$$

$$V(k_y) = \pm \sin(E)^{-1}\Big(2\sqrt{2}\lambda_\alpha\kappa_\beta\kappa_\gamma \cos(2k_x + 2k_y) - 4\kappa_\alpha\kappa_\beta\kappa_\gamma \sin(2k_x + 2k_y) + 2\sqrt{2}\lambda_\alpha\kappa_\beta\lambda_\gamma \sin(2k_y)\Big). \tag{4.61}$$

The protocol of A class alongside the using doubling procedure can produce the necessary protocols for simulating AII and C classes. As we recall, the doubling procedure requires consideration of two additional internal states for the walk. For AII class, we find the proper protocol as

$$\widehat{U} = \begin{pmatrix} \widehat{U}_d & 0 \\ 0 & 1 \end{pmatrix} e^{-i\tau_y\sigma_y\phi/2} \begin{pmatrix} 1 & 0 \\ 0 & \widehat{U}_d^t \end{pmatrix}, \tag{4.62}$$

where τ_y is a Pauli matrix related to the two additional internal states (flavors) and $\widehat{U}_d$ is given in Eq. (4.57). This protocol has only the TRS with squaring to $-\widehat{I}$. Therefore, it indeed simulates AII class in two dimensions. As for the C class, we use a rather different formula for building its proper protocol. The formula is given by

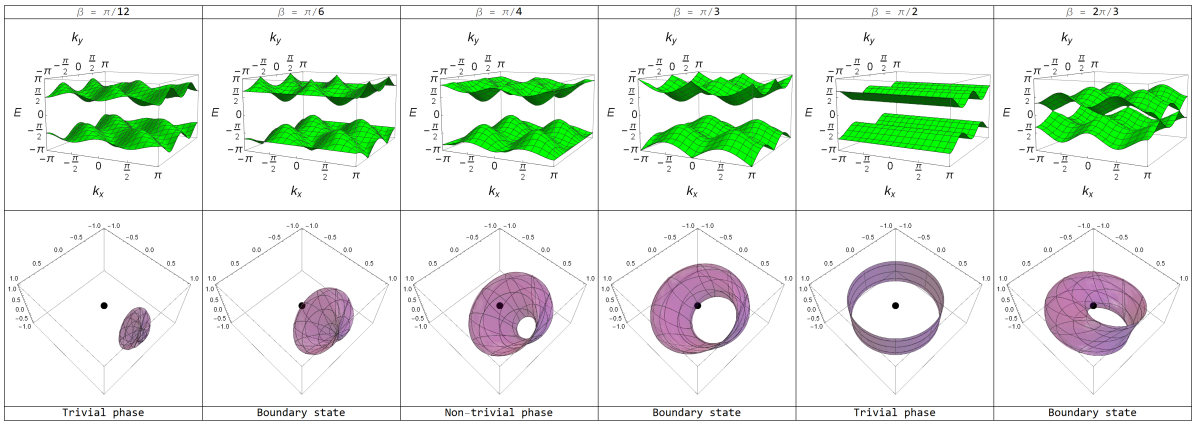

Figure 4.18: Two-dimensional A class: Modification of energy (upper panel) and $\mathbf{d}$ (lower panel) with $T = 2$ and $\alpha = \pi/3$. The $\mathbf{d}$ surfaces are plotted by variation of the momenta through the first Brillouin zone. We observe simulations of trivial phases ($\beta = \pi/12$ and $\pi/2$), non-trivial ones $\beta = \pi/4$, and boundary states ($\beta = \pi/6$, $\pi/3$ and $2\pi/3$). In case of boundary states, $\mathbf{d}$ passes the origin.

$$\widehat{U} = \begin{pmatrix} \widehat{U}_d & 0 \\ 0 & \widehat{U}_d^* \end{pmatrix}, \tag{4.63}$$

in which $*$ stands for complex conjugate. This protocol has only the PHS with operator of $\widehat{\mathcal{P}} = i\tau_y\widehat{K}$ which squares to $\widehat{\mathcal{P}}^2 = -\widehat{I}$. Therefore, the protocol can simulate C class of topological phases in two dimensions.

As we highlighted before for A class, by tuning the rotation angles, we are able to produce energy bands that are independent of one of the momenta or linear functions of them. The Dirac cone boundary states are found if we fix one of the momenta and let the other one varies. The flat bands and Fermi arc boundary states are formed when both of the momenta traverse the first Brillouin zone. Therefore, we can simulate three types of the Fermi arc, Dirac cone, and flat bands boundary states (see Fig. 4.17).

Regarding the phase structure of the simulated A class, our case study in a limited range of rotation angle shows that two trivial phases can be found between two non-trivial ones (see Fig. 4.18). Therefore, we have two types of phase transitions: a transition between two similar phases (trivial to trivial) and a transition between two different phases (trivial to non-trivial).

Two-dimensional D and DIII classes

Similar to its one-dimensional counterpart, the topological phases of class D requires the system having only the PHS. To achieve this, we consider the following protocol

$$\widehat{U} = \widehat{S}_{\uparrow\downarrow}(x)\widehat{C}_\beta\widehat{S}_{\uparrow\downarrow}(y)\widehat{C}_\alpha\widehat{S}_{\uparrow\downarrow}(x,y)\widehat{C}_\beta, \tag{4.64}$$

where $\widehat{S}_{\uparrow\downarrow}(x,y)$ breaks the CHS, and since the matrix elements are real and rotation matrices are in xy plane, the PHS is preserved for this protocol. The TRS should automatically be absent since its presence would lead to the presence of the CHS. The energy bands for this protocol are found as

$$\begin{aligned} E = \pm\cos^{-1}\Big(&\kappa_\alpha[\cos(T\beta)\cos(k_x)\cos(k_x+2k_y)-\sin(k_x)\sin(k_x+2k_y)]- \\ &\lambda_\alpha\sin(T\beta)\cos^2(k_x)\Big). \end{aligned} \tag{4.65}$$

The followings could be pointed out regarding the energy bands:

I) If $\alpha = \beta = \pm(2c+1)\pi/2T$, then energy bands will be independent of k_y and gap-closure happens nonlinearly. In addition, by setting $\alpha = \beta = \pm 2c\pi/T$ and provided $k_x = \pm(2c+1)\pi/2$ $k_y = \pm c\pi$, the energy bands close their gap nonlinearly. Therefore, Fermi arc boundary states are observable for both cases.

II) In case of $\alpha = \beta = \pm 2c\pi/T$ and appropriate values of k_x and k_y, the gap-closure will be linearly, and therefore, the boundary states are Dirac cone type.

Next, we find $\mathbf{d}$ (hence $\mathbf{n}$) in form of

$$\begin{aligned} d_x &= 2\lambda_\beta\sin(k_x)\left[\kappa_\alpha\kappa_\beta\cos(k_x+2k_y)-\lambda_\alpha\lambda_\beta\cos(k_x)\right], \\ d_y &= \lambda_\alpha\kappa_\beta^2-\lambda_\alpha\lambda_\beta^2\cos(2k_x)+2\kappa_\alpha\kappa_\beta\lambda_\beta\cos(k_x)\cos(k_x+2k_y), \\ d_z &= \lambda_\alpha\kappa_\beta\lambda_\beta\sin(2k_x)-\kappa_\alpha[\kappa_\beta^2\sin(2(k_x+k_y))+\lambda_\beta^2\sin(2k_y)]. \end{aligned} \tag{4.66}$$

The symmetry operator of the PHS is the complex conjugate operator, $\widehat{K}$, since the matrix elements of the protocol are all real-valued. The PHS operator squares to $+\widehat{I}$ which brings us to the simulation of the D class of the topological phases in two dimensions. The group velocity can be calculated as

$$\begin{aligned} V(k_x) = \pm\sin(E)^{-1}\Big(&2\lambda_\alpha\sin(T\beta)\sin(k_x)\cos(k_x)-\cos(k_x+2k_y)\sin(k_x)\lambda_\alpha \\ &[1+\cos(k_x+2k_y)]-\kappa_\alpha\cos(k_x)\sin(k_x+2k_y)[1+\cos(T\beta)]\Big), \end{aligned} \tag{4.67}$$

$$V(k_y) = \pm\frac{-2\kappa_\alpha\cos(T\beta)\cos(k_x)\sin(k_x+2k_y)-2\kappa_\alpha\sin(k_x)\cos(k_x+2k_y)}{\sin(E)}. \tag{4.68}$$

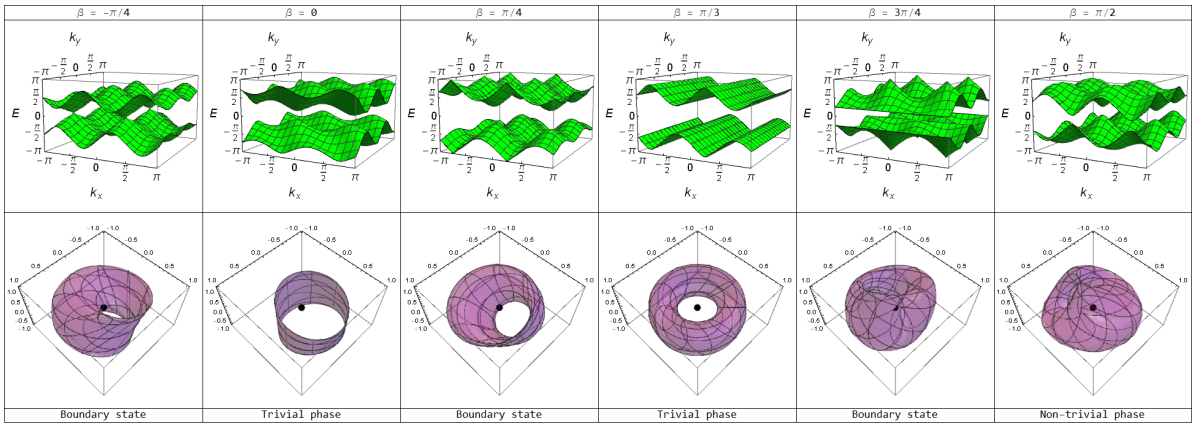

Figure 4.19: Two-dimensional D class: Modification of energy (upper panel) and $\mathbf{d}$ (lower panel) with $T = 3$, $\alpha = \pi/3$ and $\gamma = \pi/4$. We observe two trivial phases for $\beta = 0$ and $\pi/3$, a non-trivial phase for $\beta = \pi/2$ and three boundary states for $\beta = -\pi/4$, $\pi/4$, and $3\pi/4$. Two trivial phases reside next to each other followed by a non-trivial phase.

Using the doubling procedure, we find the protocol of the quantum walk simulating the topological phases of the DIII class as

$$\widehat{U} = \begin{pmatrix} \widehat{U}_c & 0 \\ 0 & \widehat{U}_{c'}^{t} \end{pmatrix}, \tag{4.69}$$

in which $\widehat{U}_c$ is Eq. (4.64) and this protocol has PHS, TRS and CHS with their operators given by $\widehat{K}$, $i\tau_y\widehat{K}$ and $\widehat{\mathcal{P}}\widehat{\mathcal{T}}$, respectively. Therefore, the squares of their operators would read as $\widehat{\mathcal{P}}^2 = +\widehat{I}$, $\widehat{\mathcal{T}}^2 = -\widehat{I}$ and $\widehat{\Gamma}^2 = +\widehat{I}$, hence enabling the simulation of the DIII class of the topological phases in two dimensions.

For the two-dimensional protocol simulating D class, similar to previous cases, it is possible to have boundary states in three forms of Dirac cone, Fermi arc, and flat bands (see Fig. 4.17). The conditions for Fermi arc boundary states are presented before. For the Dirac cone boundary states, we need to fix one of the momenta and let the other one varies. Whereas for the flat bands, the two momenta should traverse the $[-\pi, \pi]$.

In the phase structure of the protocol of the D class, we showed that at the neighbors of each phase, there are two phases that are different from that phase (see Fig. 4.19). Therefore, in contrast to the protocol of A class, the only type of phase transition observed in the protocol of D class is between two different phases of trivial to non-trivial or vice versa.

4.2.3 *Topological phenomena in three dimensions*

In this section, we introduce five protocols to simulate different classes of the topological phases in three dimensions. Before we do so, we should highlight a few issues regarding the three-dimensional phases.

Schnyder et al. pointed out that for some of the topological phases such as insulators and superconductors in three dimensions, the Hamiltonian should possess the minimal number of four energy bands (Schnyder et al., 2008; Ryu et al., 2010; Chiu et al., 2016; Zhang et al., 2018). This means that system should have at least four internal states. In contrast, there are Weyl semimetallic phases that can be described by Hamiltonians with only two bands of energy. In what follows, we introduce protocols with two internal states and then use the doubling procedure to build Hamiltonians with four energy bands. Our approach is motivated by the following points:

I) It is possible to use the method of dimensional reduction and relate different families of the topological phases from a dimension to another one (Ryu et al., 2010). The procedure requires compactification of one or more spatial dimensions similar to Kaluza-Klein approach.

II) Our protocols in three dimensions can produce Hamiltonians with two bands of energy that can simulate Weyl semimetallic phases (Okugawa and Murakami, 2014; Weng et al., 2015; Burkov, 2016; Yokomizo and Murakami, 2017; Armitage et al., 2018; Rafi-Ul-Islam et al., 2020). Naively speaking, the Hamiltonians with two bands of energy have only three anticommuting terms given by Pauli matrices which vanish at discrete points in the first Brillouin zone. This will lead to the formation of the Weyl semimetallic phases (Li and Chen, 2019).

III) Finally, the Hamiltonians with two bands of energy can be used as building blocks of the Hamiltonians with four bands of energy. This is done via the doubling procedure.

The protocols devised by doubling procedure can be decomposed in the following forms; If the protocols are produced using $\widehat{U}' = \begin{pmatrix} \widehat{U} & 0 \\ 0 & \widehat{U}^t \end{pmatrix}$, the decomposition would be

$$\widehat{U}' = d_0\tau_0 \otimes \sigma_0 - Id_1\tau_0 \otimes \sigma_1 - Id_2\tau_3 \otimes \sigma_2 - I\tau_0 \otimes \sigma_3, \tag{4.70}$$

On the other hand, if the doubling procedure has used $\widehat{U} = \begin{pmatrix} \widehat{U} & 0 \\ 0 & \widehat{U}^* \end{pmatrix}$, the decomposition of the resulted protocol would be

$$\widehat{U}' = d_0\tau_0 \otimes \sigma_0 - Id_1\tau_3 \otimes \sigma_1 - Id_2\tau_0 \otimes \sigma_2 - I\tau_3 \otimes \sigma_3, \tag{4.71}$$

in which σ_i and τ_i are Pauli matrices for the two internal states of $|\uparrow\rangle$ and $|\downarrow\rangle$, and two flavors of A and B, respectively. These decompositions are necessary for calculating the topological invariant.

Finally, due to the size of the calculated $\mathbf{d}$ and components of the group velocity for three-dimensional cases, we provide them in appendix 7.3.

Three-dimensional BDI class

According to non-driven topological phases, in the three-dimensional BDI class, only trivial phases can be observed. While this is the case, for driven systems, the situation could be rather different; Although only trivial phases could be observed for driven systems as well, there are other phenomena such as mulitciriticality could emerge. Therefore, we start our discussion by building two protocols for BDI class in three dimensions.

The first protocol is simple-step with the following structure (Panahiyan and Fritzsche, 2021)

$$\widehat{U} = \widehat{S}_{\uparrow\downarrow}(z)\widehat{S}_{\uparrow\downarrow}(y)\widehat{S}_{\uparrow\downarrow}(x)\widehat{C}_\theta, \tag{4.72}$$

with shift operators given as

$$\widehat{S}_{\uparrow\downarrow}(x) = |\uparrow\rangle\langle\uparrow| \otimes \sum_{x,y,z} |x+1,y,z\rangle\langle x,y,z| + |\downarrow\rangle\langle\downarrow| \otimes \sum_{x,y,z} |x-1,y,z\rangle\langle x,y,z|\,, \tag{4.73}$$

$$\widehat{S}_{\uparrow\downarrow}(y) = |\uparrow\rangle\langle\uparrow| \otimes \sum_{x,y,z} |x,y+1,z\rangle\langle x,y,z| + |\downarrow\rangle\langle\downarrow| \otimes \sum_{x,y,z} |x,y-1,z\rangle\langle x,y,z|\,, \tag{4.74}$$

$$\widehat{S}_{\uparrow\downarrow}(z) = |\uparrow\rangle\langle\uparrow| \otimes \sum_{x,y,z} |x,y,z+1\rangle\langle x,y,z| + |\downarrow\rangle\langle\downarrow| \otimes \sum_{x,y,z} |x,y,z-1\rangle\langle x,y,z|\,, \tag{4.75}$$

in which we use the Fourier transformation to find them as $\widehat{S}_{\uparrow\downarrow}(x) = e^{ik_x\sigma_z}$, $\widehat{S}_{\uparrow\downarrow}(y) = e^{ik_y\sigma_z}$, and $\widehat{S}_{\uparrow\downarrow}(z) = e^{ik_z\sigma_z}$ where k_x, k_y and k_z span the first Brillouin zone. The energy bands of this protocol are found as

$$E = \pm\cos^{-1}\Big(\kappa_\theta \cos(k_x + k_y + k_z)\Big), \tag{4.76}$$

which have gap-closure at $E = 0$ and $\pm\pi$ for

$$\theta_{E=\pi} = \frac{\pm 2\cos^{-1}[-\sec(k_x + k_y + k_z)] + 4\pi c}{T}, \tag{4.77}$$

$$\theta_{E=0} = \frac{\pm 2\cos^{-1}[\sec(k_x + k_y + k_z)] + 4\pi c}{T}. \tag{4.78}$$

and energy bands become flat bands if

$$\theta_{E=\pm\pi/2} = \frac{4\pi c \pm \pi}{T}. \tag{4.79}$$

Next, we find $\mathbf{n}$ as

$$\mathbf{n} = \frac{1}{\sin(E)} \begin{pmatrix} \kappa_\theta \sin(k_x + k_y + k_z) \\ \lambda_\theta \cos(k_x + k_y + k_z) \\ -\kappa_\theta \sin(k_x + k_y + k_z) \end{pmatrix}. \tag{4.80}$$

Like its one- and two-dimensional counterparts, the protocol has three symmetries of the CHS, PHS, and TRS. The PHS operator is the complex conjugate operator. The CHS operator is found by using $\boldsymbol{A} = (\kappa_\theta, 0, \lambda_\theta)$. The TRS operator is obtained by $\widehat{\Gamma}\widehat{\mathcal{P}}$. The squaring of all the three symmetry operators yield $+\widehat{I}$ which indicates simulation of the BDI class. Finally, we find the components of the group velocity admitting $V_{k_x} = V_{k_y} = V_{k_y} = \pm n_z$ which puts a limit on the values that group velocity can attain.

Next, we modify the simple-step protocol into split-step in the form of

$$\widehat{U} = \widehat{S}_{\uparrow\downarrow}(z)\widehat{C}_\gamma \widehat{S}_{\uparrow\downarrow}(y)\widehat{C}_\alpha \widehat{S}_{\uparrow\downarrow}(x)\widehat{C}_\beta, \tag{4.81}$$

where the coin and shift operators are given in Eqs. (4.17), (4.18) and (4.73)-(4.75), and the coin operator $\widehat{C}_\gamma$ is likewise $\widehat{C}_\beta$. The energy bands associated to this protocol are found as

$$\begin{aligned} E = \pm\cos^{-1}\Big(& \cos(k_x + k_y + k_z)\kappa_\gamma\kappa_\alpha\kappa_\beta - \cos(k_x - k_y - k_z)\kappa_\gamma\lambda_\alpha\lambda_\beta - \\ & \cos(k_x - k_y + k_z)\lambda_\gamma\lambda_\alpha\kappa_\beta - \cos(k_x + k_y - k_z)\lambda_\gamma\kappa_\alpha\lambda_\beta \Big). \end{aligned} \tag{4.82}$$

For the obtained energy bands, we find the followings:

I) By considering $\alpha = \beta = \pm(2c+1)\pi/T$ and $\gamma = \pm 2c\pi/T$, the energy bands become linear functions of the momenta which indicates that boundary states are Dirac cone type. The same takes place if $\beta = \gamma = \pm 2c\pi/T$ and $\alpha = \pm(2c+1)\pi/T$.

II) In case of $\beta = \alpha = \gamma = \pm(2c+1)\pi/T$ or $\beta = \alpha = \gamma = \pm 2c\pi/T$, the energy bands would be flat with $E = \pm\pi/2$.

III) If the last two conditions are not met, the gap-closure would be nonlinear.

The components of the $\mathbf{d}$ and group velocity are given in Eqs. (7.14) and (7.15). The split-step protocol here has three symmetries of the CHS, PHS, and TRS. The PHS operator is the same as the simple-step protocol while to build the CHS protocol, we use $\boldsymbol{A} = (\kappa_\beta, 0, \lambda_\beta)$ and TRS operator is found by the other two symmetry operators. All the three symmetry operators admit the squaring of $+\widehat{I}$, hence the protocol simulating BDI class.

Three-dimensional D and DIII classes

To break the CHS and TRS and retain the PHS, we consider the following protocol

$$\widehat{U} = \widehat{S}_{\uparrow\downarrow}(z)\widehat{C}_\zeta\widehat{S}_{\uparrow\downarrow}(y)\widehat{C}_\gamma\widehat{S}_{\uparrow\downarrow}(x)\widehat{C}_\alpha\widehat{S}_{\uparrow\downarrow}(x,y,z)\widehat{C}_\beta, \tag{4.83}$$

where $\widehat{S}_{\uparrow\downarrow}(x,y,z)$ breaks the CHS and the absence of CHS removes the TRS as well. $\widehat{S}_{\uparrow\downarrow}(x,y,z)$ is given by

$$\begin{aligned}\widehat{S}_{\uparrow\downarrow}(x,y,z) = {} & |\uparrow\rangle\langle\uparrow| \otimes \sum_{x,y,z} |x+1,y+1,z+1\rangle\langle x,y,z| + \\ & |\downarrow\rangle\langle\downarrow| \otimes \sum_{x,y,z} |x-1,y-1,z-1\rangle\langle x,y,z| \,. \end{aligned} \tag{4.84}$$

The energy bands are calculated as

$$\begin{aligned} E = {} & \pm\cos^{-1}\Big(\kappa_\alpha\kappa_\beta[\kappa_\gamma\kappa_\zeta\cos(2k_x+2k_y+2k_z) - \lambda_\gamma\lambda_\zeta\cos(2k_x+2k_z)] \\ & -\kappa_\alpha\lambda_\beta[\lambda_\gamma\kappa_\zeta\cos(2k_x) + \kappa_\gamma\lambda_\zeta\cos(2k_x+2k_y)] - \lambda_\alpha\lambda_\beta[\kappa_\gamma\kappa_\zeta - \lambda_\gamma\lambda_\zeta\cos(2k_y)] \\ & -\lambda_\alpha\kappa_\beta[\lambda_\gamma\kappa_\zeta\cos(2k_y+2k_z) + \kappa_\gamma\lambda_\zeta\cos(2k_z)]\Big), \end{aligned} \tag{4.85}$$

which can have the following indications:

I) If $\beta = \pm(2c+1)\pi/T$, $\alpha = \gamma = \zeta = \pm 2c\pi/T$, the energy bands will become linear dependent on the momenta. Therefore, the gap-closure happens linearly, hence Dirac cone boundary states. On the other hand, by setting $\alpha = \zeta = \pm 2c\pi/T$ and $\beta = \gamma = \pm(2c+1)\pi/T$, the energy bands become independent of momenta k_y and k_z while it is linear function of k_x which indicates Dirac cone boundary states.

II) In case of $\gamma = \zeta = \pm 2c\pi/T$, the energy bands reduce to $E = \pm\cos^{-1}(\pm\lambda_\alpha\lambda_\beta)$. Therefore, if any gap-closure happens, it would be in form of flat bands. This is similar to the flat bands observed in the one-dimensional case and different from the

ones in two dimensions. It is worthwhile to mention that we have a network of flat bands including flat bands boundary states in this case.

III) If the last two conditions are not satisfied for the energy bands, the gap-closure would be in nonlinear form, hence Fermi arc boundary states.

Next, we calculate $\mathbf{d}$ (hence $\mathbf{n}$) and components of group velocity resulting in Eqs. (7.16) and (7.17), respectively. The protocol only admits the PHS with the symmetry operator being the complex conjugate operator since all the elements of the protocol's matrix are real-valued. It is straightforward to find $\widehat{\mathcal{P}}^2 = +\widehat{\mathrm{I}}$. Therefore, the protocol simulates phases of the D class in three dimensions which are only trivial ones.

Now, we are in a position to build a protocol that simulates DIII topological phases in three dimensions. We use the doubling procedure which gives us the protocol as

$$\widehat{\mathrm{U}} = \begin{pmatrix} \widehat{\mathrm{U}}_e & 0 \\ 0 & \widehat{\mathrm{U}}_e^{\mathrm{t}} \end{pmatrix}, \tag{4.86}$$

where $\widehat{\mathrm{U}}_e$ is given by Eq. (4.83). The protocol has PHS, TRS, and CHS with $\widehat{\mathcal{P}}^2 = +\widehat{\mathrm{I}}$, $\widehat{\mathcal{T}}^2 = -\widehat{\mathrm{I}}$ and $\widehat{\Gamma}^2 = +\widehat{\mathrm{I}}$ and it can simulate DIII family of the topological phases.

Three-dimensional AIII and CII classes

In AIII class of the topological phases, the CHS symmetry is present while PHS and TRS are absent. To break the PHS, we perform at least one of the rotations by coin operators in a non-xy plane. To this end, we consider the following protocol

$$\widehat{\mathrm{U}} \;=\; \widehat{\mathrm{S}}_{\uparrow\downarrow}(z)\widehat{\mathrm{C}}_\gamma\widehat{\mathrm{S}}_{\uparrow\downarrow}(y)\widehat{\mathrm{C}}_\alpha\widehat{\mathrm{S}}_{\uparrow\downarrow}(x)\widehat{\mathrm{C}}_\beta, \tag{4.87}$$

where the rotation matrices rotate the internal states with respect to $\phi = \frac{1}{\sqrt{2}}(0,1,1)$. The energy bands of this protocol are obtained as

$$\begin{aligned} \mathrm{E} \;=\; & \pm\cos^{-1}\Bigg(\left[2\lambda_\alpha\kappa_\beta\kappa_\gamma + 2\kappa_\alpha\lambda_\beta\kappa_\gamma + 2\kappa_\alpha\kappa_\beta\lambda_\gamma - \lambda_\alpha\lambda_\beta\lambda_\gamma\right]\frac{\sin(k_x+k_y+k_z)}{2\sqrt{2}} \\ & -\frac{1}{2}[\lambda_\alpha\lambda_\beta\kappa_\gamma\cos(k_x-k_y-k_z) + \kappa_\alpha\lambda_\beta\lambda_\gamma\cos(k_x+k_y-k_z) + \lambda_\alpha\kappa_\beta\lambda_\gamma\cos(k_x-k_y+k_z)] \\ & +[2\kappa_\alpha\kappa_\beta\kappa_\gamma - \lambda_\alpha\lambda_\beta\kappa_\gamma - \lambda_\alpha\kappa_\beta\lambda_\gamma - \kappa_\alpha\lambda_\beta\lambda_\gamma]\frac{\cos(k_x+k_y+k_z)}{2} \\ & +[\sin(k_x-k_y-k_z) - \sin(k_x+k_y-k_z) - \sin(k_x-k_y+k_z)]\,\frac{\lambda_\alpha\lambda_\beta\lambda_\gamma}{2\sqrt{2}}\Bigg). \end{aligned} \tag{4.88}$$

Evidently, in case of $\alpha = \beta = \gamma = \pm 2c\pi/T$, the energy bands will be linear functions of momenta. Therefore, the boundary states are in the form of Dirac cone

boundary states. Otherwise, the gap-closure will happen nonlinearly, hence Fermi arc boundary states.

Next, we find $\mathbf{d}$ and group velocity as (7.18) and (7.19), respectively. The rotation of internal states around the ϕ axis breaks the PHS. The absence of the PHS enforces the absence of TRS. The symmetry operator of the CHS is squaring to $+\widehat{I}$ which is a necessary condition to simulate AIII class of the topological phases in three dimensions with this protocol of the quantum walk.

Similar to its two-dimensional counterpart, by using the protocol for simulation of the AIII class and doubling procedure, we can build

$$\widehat{U} = \begin{pmatrix} \widehat{U}_f & 0 \\ 0 & \widehat{U}_f^t \end{pmatrix}, \tag{4.89}$$

in which $\widehat{U}_f$ is given by Eq. (4.87). The symmetries of this protocol are PHS, TRS, and CHS with $\widehat{\mathcal{P}}^2 = -\widehat{I}$, $\widehat{\mathcal{T}}^2 = -\widehat{I}$ and $\widehat{\Gamma}^2 = +\widehat{I}$. Therefore, this protocol simulates three-dimensional topological phases of the CII class.

Three-dimensional A, AII and C classes

To build a protocol simulating topological phases of AII class in three dimensions, we first need to introduce a protocol for simulating trivial phases of the A class in three dimensions. Such a protocol has the following form

$$\widehat{U} = \widehat{S}_{\uparrow\downarrow}(z)\widehat{C}_\zeta \widehat{S}_{\uparrow\downarrow}(y)\widehat{C}_\gamma \widehat{S}_{\uparrow\downarrow}(x)\widehat{C}_\alpha \widehat{S}_{\uparrow\downarrow}(x,y,z)\widehat{C}_\beta, \tag{4.90}$$

in which rotation matrix $\widehat{C}_\alpha$ is rotation around $\boldsymbol{\phi}$ axis which breaks the PHS and $\widehat{S}_{\uparrow\downarrow}(x,y,z)$ does the the same for the CHS. It should be noted that the other coin operators are rotation matrices in the xy plane. The energy bands of this protocol are given by

$$\begin{aligned} E \;=\; & \pm\cos^{-1}\Bigg(\kappa_\alpha\kappa_\beta\kappa_\gamma\kappa_\zeta\cos(2k_x+2k_y+2k_z)+\frac{\lambda_\alpha\kappa_\beta\kappa_\gamma\kappa_\zeta\sin(2k_x+2k_y+2k_z)}{\sqrt{2}} \\ & +[\lambda_\zeta\cos(2k_y)-\kappa_\zeta\sin(2k_x)]\frac{\lambda_\alpha\lambda_\beta\lambda_\gamma}{\sqrt{2}}-\frac{\lambda_\alpha\lambda_\beta\kappa_\gamma\kappa_\zeta}{\sqrt{2}}-\kappa_\alpha\lambda_\beta\lambda_\gamma\kappa_\zeta\cos(2k_x) \\ & -\kappa_\alpha\lambda_\beta\kappa_\gamma\lambda_\zeta\cos(2k_x+2k_y)-\kappa_\alpha\kappa_\beta\lambda_\gamma\lambda_\zeta\cos(2k_x+2k_z) \\ & +\frac{\lambda_\alpha}{\sqrt{2}}\Big[\lambda_\beta\kappa_\gamma\lambda_\zeta\sin(2k_x+2k_y)+\kappa_\beta\lambda_\gamma\lambda_\zeta\sin(2k_x+2k_z) \\ & +\kappa_\beta\lambda_\gamma\kappa_\zeta\cos(2k_y+2k_z)+\kappa_\beta\kappa_\gamma\lambda_\zeta\cos(2k_z)\Big]\Bigg). \end{aligned} \tag{4.91}$$

The followings can be highlighted for the energy bands:

I) By setting $\alpha = \beta = \gamma = \zeta = \pm 2c\pi/T$, the energy bands become linear functions of the momenta, therefore indicating the presence of Dirac cone boundary states. Additionally, if $\alpha = \beta = \gamma = \pm(2c+1)\pi/T$ and $\zeta = \pm 2c\pi/T$, the energy bands will be independent of momenta k_y and k_z and linear functions of k_x, hence Dirac cone boundary states.

II) In case of $\alpha = \beta = \pm(2c+1)\pi/T$ and $\gamma = \zeta = \pm 2c\pi/T$, flat bands with energy of $E = \pm\pi/4$ are formed.

III) If the last two conditions are not admitted, the gap-closure for energy bands will be nonlinearly, hence Fermi arc boundary states.

Next, it is a matter of calculation to find $\mathbf{d}$ and group velocity in Eqs. (7.20) and (7.21), respectively.

As we pointed out before, for the protocol simulating A class introduced in Eq. (4.90), all the three symmetries are absent. This enables us to use this protocol alongside the doubling procedure to introduce two new protocols for simulating AII and C classes in three dimensions. For AII class, we find its simulating protocol in the quantum walk as

$$\widehat{U} = \begin{pmatrix} \widehat{U}_g & 0 \\ 0 & 1 \end{pmatrix} e^{-i\tau_y \sigma_y \phi/2} \begin{pmatrix} 1 & 0 \\ 0 & \widehat{U}_g^t \end{pmatrix}, \tag{4.92}$$

where $\widehat{U}_g$ is given by Eq. (4.90). This protocol has only the TRS with $\widehat{\mathcal{T}}^2 = -\widehat{I}$. Therefore, AII class of the topological phases can be simulated by this protocol. The other protocol which simulates trivial phases of the C class is given by

$$\widehat{U} = \begin{pmatrix} \widehat{U}_g & 0 \\ 0 & \widehat{U}_g^* \end{pmatrix}, \tag{4.93}$$

which admits presence of only the PHS with $\widehat{\mathcal{T}}^2 = -\widehat{I}$. This indicates the simulation of trivial phases of C class in three dimensions.

4.2.4 *On the controllability of the simulated topological phenomena*

Through previous sections, we considered step-dependent coins in the protocols of the quantum walks in different dimensions. The utmost result of such consideration was step-dependent Hamiltonians, energy bands, $\mathbf{n}$, group velocities, and in general, step-dependent simulated topological phenomena. This step-dependency indicates that from one step to another one, the phase structure, including phases and boundary

states, would be different. The numbers of the phases and boundary states are increasing functions of the step number. Therefore, as the quantum walk proceeds, the number of phases and boundary states would increase, and consequently, the rotation angles in which boundary states and or phases could emerge are modified as well. In addition, the size of the phases shrinks as step number increases.

These features point to the possibility of a high-level control provided through step number of the quantum walk. To put it more simply, by using the step number, tuning the rotation angles, and employing proper protocol, we can determine where and when a certain phase appears or the energy bands close their gaps. For example, for BDI class of one-dimensional walk, we showed that if in the split-step protocol, rotation angles are not linearly related, we can simulate only one type of the boundary states in the walk, hence one type of dispersive behavior for the walker. By considering a linear relation between the rotation angles, we had emergences of cell-like structures that contained all three types of the boundary states and all phases observable in BDI class in one dimension. Therefore, we observe that our introduction of step-dependent coins into the protocol of the quantum walks provides us with a high level of control over the simulation of the topological phases, boundary states, and in general the properties of the simulated topological phenomena.

4.2.5 *Critical exponents, scaling law and correlation function*

In Landau paradigm, the usual second-order (quantum) phase transition of the system can be characterized by a series of parameters that are known as critical exponents. The critical exponents are universal parameters that describe the behavior of the system near the critical point. These parameters are used to classify materials with similar critical behavior.

For topological phases of the matter, the modification in the topological invariant and formation of the boundary states indicate a phase transition. In general, to find the topological invariant and study its modification, one uses the curvature function. The curvature function is defined as the function whose momentum space integration gives the topological invariant.

In a series of studies, it was shown that the curvature function can be used to extract critical exponents and scaling laws governing the topologically ordered materials. In addition, via the Fourier transformation of the curvature function, it was possible to find the correlation function. Due to the geometrical nature of the curvature function, the approach is not limited to specific materials, rather applicable to different topological phases of materials observed in arbitrary dimensions.

As we established before, the quantum walk can simulate different topological phases that are observed in condensed matter. Here, the question would arise on how the critical exponents, scaling law, correlation function, and in general critical behavior of the system can be characterized in terms of simulation's parameters, hence coins and shift operators of the quantum walk.

Curvature function and critical properties of the system

The curvature function is built by using Berry curvature or connection depending on the dimensionality of the system. The Berry curvature is calculated with eigenstates of the Hamiltonian describing the system. Therefore, we use the eigenstates to find the curvature function.

The D-dimensional Hamiltonian describing topological phases of matter is parameterized by two distinct sets of parameters; $\mathbf{k}$ which are momenta in D dimensions and tunable parameters in the Hamiltonian, $\mathbf{M}$. The topological invariant is calculated by integration of the curvature function over the first Brillouin zone (BZ)

$$\gamma(M) \quad = \quad \int_{BZ} F(\mathbf{k}, \mathbf{M}) \frac{d^d \mathbf{k}}{(2\pi)^d}, \tag{4.94}$$

in which $F(\mathbf{k}, \mathbf{M})$ is the curvature function. Different topological phases and their corresponding boundary states are obtained by tuning $\mathbf{M}$. Therefore, there is a $\mathbf{M}_c$ in which a boundary state is formed (gap-closure happens) and the system acquires a phase transition point. c stands for critical. Generally speaking, as $\mathbf{M}$ crosses the critical point ($\mathbf{M}_c$), the topological invariant jumps from one integer to another.

The key ingredient of using the curvature function as a tool to investigate the topological phase transition is its varying nature. In other words, as $\mathbf{M}$ changes and it does not meet a gapless point ($\mathbf{M}_c$), the topological invariant is fixed whereas the profile of the curvature function varies. As we get close to the gap-closure point, the variation in curvature function features specific properties that enable us to characterize the critical behavior of the system with curvature function and extract correlation function, critical exponents, length scale, and validate a scaling law.

The curvature function is an even function around the critical point, $F(\mathbf{k}_c + \delta\mathbf{k}) = F(\mathbf{k}_c - \delta\mathbf{k})$, in which $\mathbf{k}_c$ is where the gap-closure takes place. In general, the critical behavior of the curvature function for different topological phases falls into two categories: Peak-divergence scenario and Shell-divergence scenario. Here, for the simulated topological phenomena, we are concerned with the Peak-divergence scenario.

In the Peak-divergence scenario, the curvature function starts to peak at the gapless point. This is done by the peak increasing its height and narrowing while the system

approaches the critical point, $\mathbf{M} \to \mathbf{M}_c$. Eventually, when $\mathbf{M} = \mathbf{M}_c$, the peak diverges and flips sign after the transition. The peak has a Lorentzian shape and it can be fitted by Ornstein-Zernike equation for one and two dimensions

$$F(k_c + \delta k, \mathbf{M}) = \frac{F(k_c, \mathbf{M})}{1 \pm \xi^2 \delta k^2}, \tag{4.95}$$

$$F(\mathbf{k}_c + \delta \mathbf{k}, \mathbf{M}) = \frac{F(\mathbf{k}_c, \mathbf{M})}{(1 \pm \xi_x^2 \delta k_x^2)(1 \pm \xi_y^2 \delta k_y^2)}, \tag{4.96}$$

in which ξ, ξ_x and ξ_y are the width of the peaks and they are the characteristic length scales. The critical behavior of the system when it approaches the two sides of the critical point $\mathbf{M}_c^+$ and $\mathbf{M}_c^-$, is summarized as

$$\lim_{\mathbf{M} \to \mathbf{M}_c^+} F(\mathbf{k}_c, \mathbf{M}) = - \lim_{\mathbf{M} \to \mathbf{M}_c^-} F(\mathbf{k}_c, \mathbf{M}) = \pm\infty, \tag{4.97}$$

$$\lim_{\mathbf{M} \to \mathbf{M}_c} \xi = \infty. \tag{4.98}$$

The divergencies observed for length scale and curvature function have indications that the critical behavior of $F(\mathbf{k}_c, \mathbf{M})$ and ξ can be parameterized by

$$F(\mathbf{k}_c, \mathbf{M}) \propto |\mathbf{M} - \mathbf{M}_c|^{-\mu}, \tag{4.99}$$

$$\xi \propto |\mathbf{M} - \mathbf{M}_c|^{-\nu}, \tag{4.100}$$

in which μ and ν are critical exponents. These exponents satisfy a scaling law in the form of $\mu = D\nu$ which is originated from the conservation of the topological invariant. It should be noted that band crossing in this scenario is one ($n = 1$).

The physical interpretation of critical exponents become transparent through the notion of the correlation function. The correlation function is introduced by the Wannier states constructed from the Bloch state of the Hamiltonian

$$|\mathbf{R}\rangle = \frac{1}{N} \sum_{\mathbf{k}} e^{i\mathbf{k}(\hat{\mathbf{r}} - \mathbf{R})} |\psi_{\mathbf{k}-}\rangle, \tag{4.101}$$

in which $|\psi_{\mathbf{k}-}\rangle$ is the lower eigenstate of the Hamiltonian. In essence, the correlation function is the Fourier transform of the curvature function. It measures the overlap of Wannier states at the origin $|0\rangle$ and at $|\mathbf{R}\rangle$ sandwiched by a certain position operator. For the one-dimensional case, the correlation function is obtained by

$$\begin{aligned} \tilde{F}_{1D}(R) &= \int_0^{2\pi} \frac{dk_x}{2\pi} F(k_x, \mathbf{M}) e^{ik_x R} = \int_0^{2\pi} \frac{dk}{2\pi} \langle \psi_- | i\partial_{k_x} | \psi_- \rangle e^{ik_x R} \\ &= \langle 0 | \hat{r} | R \rangle = \int dr\, r\, W^*(r) W(r - R), \end{aligned} \tag{4.102}$$

where $\langle\psi_-|i\partial_{k_x}|\psi_-\rangle$ is the Berry connection, $\langle r|R\rangle = W(r-R)$ is the Wannier function centering at the home cell R, and $\hat{r}$ is the position operator. If the curvature function is replaced by (4.95), the Wannier state correlation function decays with the length scale ξ. This indicates that ξ is the correlation length, assigned with the critical exponent ν as in the convention of statistical mechanics. For two-dimensional systems, we have

$$\begin{aligned}\tilde{F}_{2D}(\mathbf{R}) &= \int \frac{d^2\mathbf{k}}{(2\pi)^2} F(\mathbf{k},\mathbf{M}) \\ &= \int \frac{d^2\mathbf{k}}{(2\pi)^2} \left\{\partial_{k_x}\langle\psi_{\mathbf{k}-}|i\partial_{k_y}|\psi_{\mathbf{k}-}\rangle - \partial_{k_y}\langle\psi_{\mathbf{k}-}|i\partial_{k_x}|\psi_{\mathbf{k}-}\rangle\right\} e^{i\mathbf{k}\cdot R} \\ &= -i\langle\mathbf{R}|(R^x\hat{y} - R^y\hat{x})|0\rangle = -i\int d^2\mathbf{r}(R^x y - R^y x)W^*(\mathbf{r}-\mathbf{R})W(\mathbf{r}), \qquad (4.103)\end{aligned}$$

in which $\partial_{k_x}\langle\psi_{\mathbf{k}-}|i\partial_{k_y}|\psi_{\mathbf{k}-}\rangle - \partial_{k_y}\langle\psi_{\mathbf{k}-}|i\partial_{k_x}|\psi_{\mathbf{k}-}\rangle$ is the Berry curvature and $\langle\mathbf{r}|\mathbf{R}\rangle = W(\mathbf{r}-\mathbf{R})$ is the Wannier function.

Critical properties of one-dimensional BDI and two-dimensional D classes

The energy bands of the one-dimensional split-step protocol for BDI class are given in Eq. (4.22). In addition, we obtained $\mathbf{n}$ in Eq. (4.23). By setting $T = 1$ and using Eq. (3.35) for calculating the topological invariant for this class, one can find the following curvature function (Panahiyan et al., 2020)

$$F(k_x,\alpha,\beta) = \left(\mathbf{n}\times\partial_{k_x}\mathbf{n}\right)\cdot\mathbf{A} = \frac{-\cos(k_x)\lambda_{2\alpha}\kappa_\beta - 2\kappa_\alpha^2\lambda_\beta}{2\sin^2(k_x)\kappa_\alpha^2 + 2\left(\cos(k_x)\kappa_\alpha\lambda_\beta + \lambda_\alpha\kappa_\beta\right)^2}. \qquad (4.104)$$

In what follows, we consider α as the tuning parameter and denote its critical point by α_c. The obtained curvature function admits the followings

$$\lim_{\alpha\to\alpha_c^-} F(k_x=0,\alpha) = \infty = -\lim_{\alpha\to\alpha_c^+} F(k_x=0,\alpha), \qquad (4.105)$$

$$\lim_{\alpha\to\alpha_c^-} F(k_x=\pi,\alpha) = -\infty = -\lim_{\alpha\to\alpha_c^+} F(k_x=\pi,\alpha), \qquad (4.106)$$

which shows a divergency and sign change of the curvature function at the critical point (see Fig. 4.20). This is in agreement with Eq. (4.99).

The Berry connection in one-dimensional systems is gauge-dependent. In the present format, the Berry connection and curvature function does not coincide. Therefore, to address this, we gauge away the z component of the ζ by rotating it around the y axis which gives us a new curvature function as

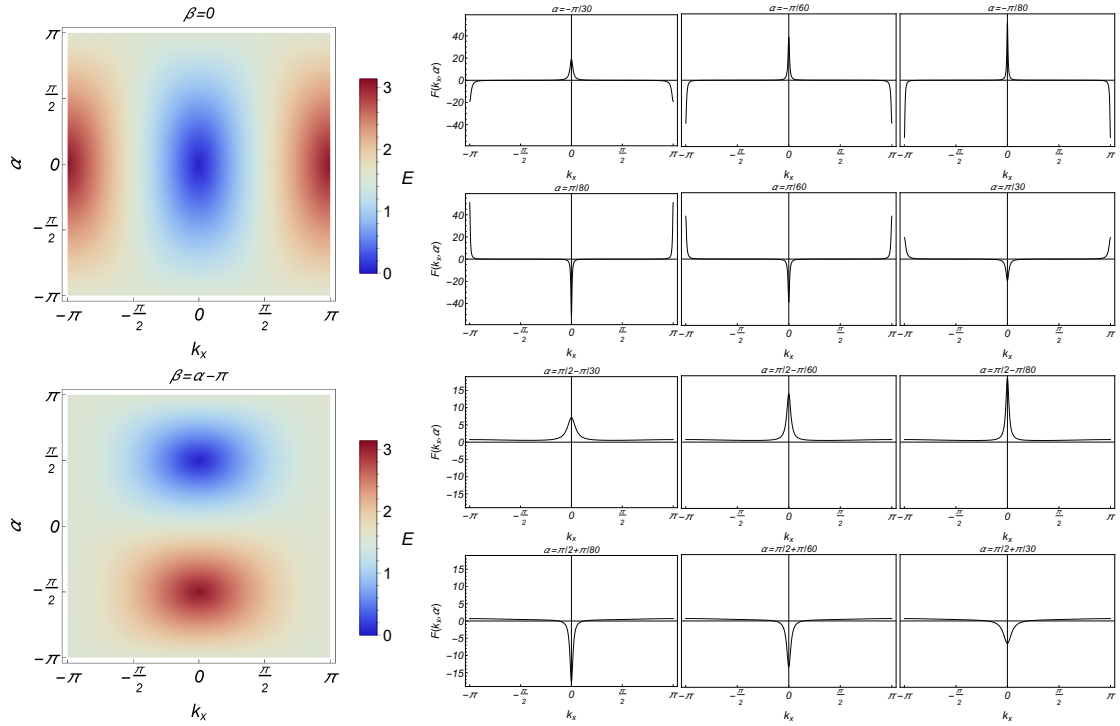

Figure 4.20: Left panel, energy as a function of rotation angle and momentum k with $\beta = 0$ and $\beta = \alpha - \pi$. In the upper panel, boundary states are Dirac cones and in the lower panel, they are Fermi arcs. In the right panel, the corresponding curvature function for $\alpha \to \alpha_c$ are plotted. The curvature function peaks around and flips at the critical point. The band crossing is one due to one peak.

$$\begin{aligned} F'(k_x,\alpha,\beta) &= \frac{\zeta'_x \partial_{k_x}\zeta'_y - \zeta'_y \partial_{k_x}\zeta'_x}{(\zeta'^2_x + \zeta'^2_y)} = 2\langle\psi'_{k-}|i\partial_{k_x}|\psi'_{k-}\rangle \\ &= \frac{-\kappa_\alpha^2\lambda_\beta - \lambda_\alpha\kappa_\alpha\kappa_\beta\cos(k_x)}{\kappa_\alpha^2\sin^2(k_x) + \lambda_\alpha^2\kappa_\beta^2 + 2\kappa_\alpha\kappa_\beta\lambda_\alpha\lambda_\beta\cos(k_x) + \kappa_\alpha^2\lambda_\beta^2\cos^2(k_x)}, \end{aligned} \tag{4.107}$$

in which considering that gap-closure happens at $k_c = 0$ and π and by series expansion of the curvature function around these points, we find that the Lorentzian shape in Eq. (4.95) can be fitted by

$$F'(k_x = \{0,\pi\},\alpha) = -\frac{\kappa_\alpha}{\lambda_{\alpha\pm\beta}} \propto \frac{1}{\lambda_{\alpha\pm\beta}}, \tag{4.108}$$

$$\xi^2(k_x = \{0,\pi\},\alpha) = \frac{1}{2}\frac{\kappa_\beta^2 + \kappa_\alpha^2\kappa_\beta^2 - \kappa_\alpha\kappa_\beta\lambda_\alpha\lambda_\beta}{\lambda^2_{\alpha\pm\beta}} \propto \frac{1}{\lambda^2_{\alpha\pm\beta}}. \tag{4.109}$$

In terms of the critical rotation angle α_c, we find

$$F(k_x = k_c,\alpha) \propto \xi(k_x = k_c,\alpha) \propto |\alpha - \alpha_c|^{-1}. \tag{4.110}$$

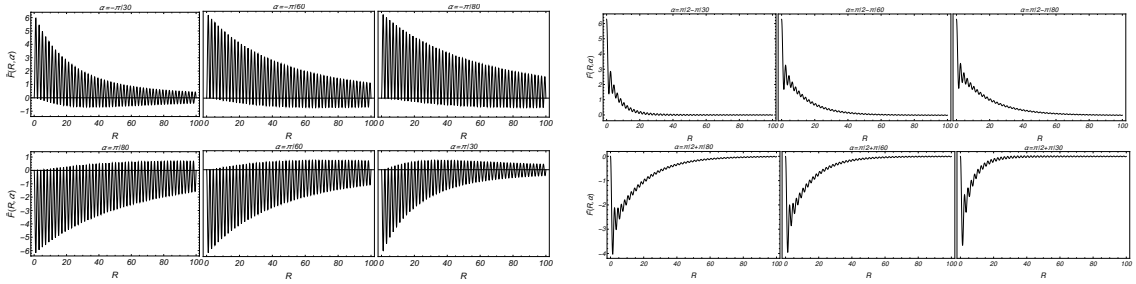

Figure 4.21: Correlation function, $\tilde{F}_{1D}(R, \alpha)$, as a function of R for two cases of $\beta = 0$ (left panel) and $\beta = \alpha - \pi$ (right panel). In the left panel, the correlation function decays via a damped oscillation. This oscillation is due to three peaks of the curvature function at $k = 0$ and $\pm\pi$. In the right panel, the correlation function decays monotonically. The correlation function has characteristic behaviors of sign flip that was observed for the curvature function around the critical point.

which gives the critical exponents as $\mu = \nu = 1$ satisfying the one-dimensional scaling law $\mu = \nu$ and BDI class that $\nu \in 2\mathbb{Z} + 1$ (Chen and Schnyder, 2019). The correlation function is obtained in the form of

$$\tilde{F}_{1D}(R, \alpha) \approx \frac{1}{2}\int_0^{2\pi} \frac{dk_x}{2\pi} \frac{F'(k_c, \alpha, \beta)}{1 + \xi^2 k_x^2} e^{ik_x R} \propto e^{-R/\xi}, \tag{4.111}$$

which decays as a function of R with the length scale ξ. Since the curvature function is the stroboscopic Berry connection of the rotated eigenstates, Eq. (4.107), the Fourier transform in Eq. (4.111) represents the correlation function between the rotated stroboscopic Wannier states with ξ playing the role of the correlation length. If the gap-closure is done linearly at $k_x = 0$ and π (Dirac boundary state), the correlation function decays through a damped oscillation (see Fig. 4.21). On the other hand, if the gap only closes at one momentum nonlinearly (Fermi arc boundary state), then the correlation function decays monotonically.

For the two-dimensional D class, we start with the curvature function

$$F(k_x, k_y, \alpha, \beta) = \left(\frac{\partial \mathbf{n}}{\partial k_x} \times \frac{\partial \mathbf{n}}{\partial k_y}\right) \cdot \mathbf{n} = \frac{\phi}{(d_x^2 + d_y^2 + d_z^2)^{\frac{3}{2}}}, \tag{4.112}$$

whose integral counts the skyrmion number of the $\mathbf{n}$ vector in the BZ, in which

$$\begin{aligned} \phi = {} & 2\kappa_\alpha \lambda_\beta \left(\kappa_\beta^2 + \lambda_\beta^2\right) \Big[4\kappa_\alpha^2 \kappa_\beta^2 \lambda_\beta \cos(k_x) \cos(k_x + 2k_y) + \kappa_\alpha \lambda_\alpha \kappa_\beta \Big(\\ & 2\kappa_\beta^2 \cos(2k_y) \cos(2k_x + 2k_y)) - \lambda_\beta^2 \left(2\cos(2k_x) + \cos(4k_y) + 3\right) \Big) \\ & + 2\lambda_\alpha^2 \lambda_\beta \cos(2k_y) \left(\lambda_\beta^2 - \kappa_\beta^2 \cos(2k_x)\right) \Big]. \end{aligned} \tag{4.113}$$

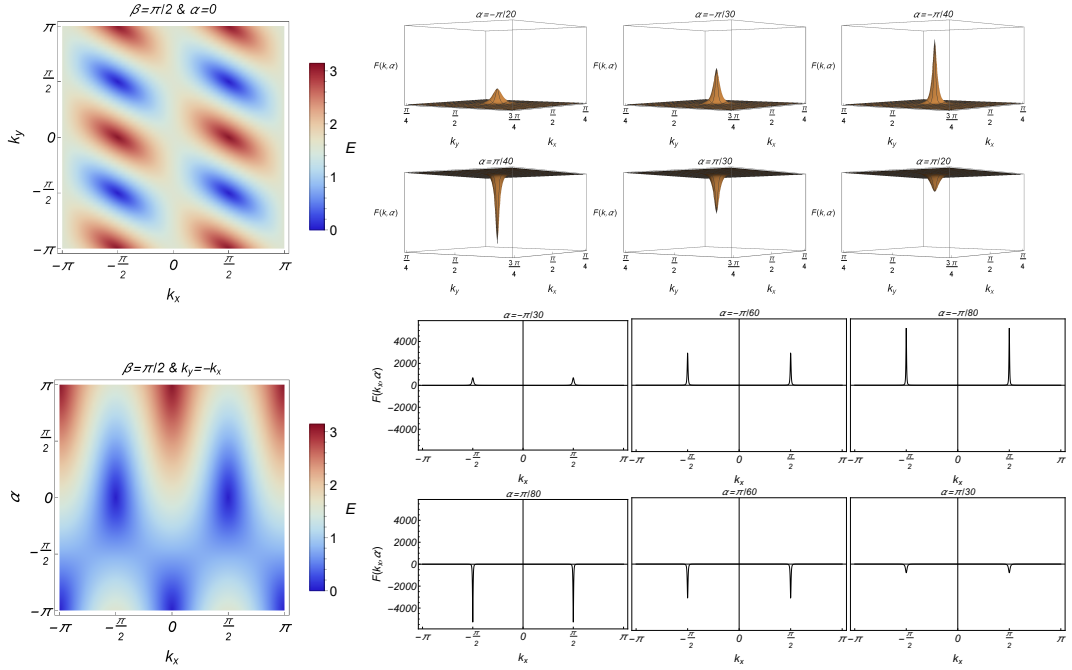

Figure 4.22: Left panel, energy as a function of rotation angle, momenta k_x and k_y for two cases of $\beta = \pi/2$ with $\alpha = 0$ and $\beta = \pi/2$ with $k_y = -k_x$. In right panel, the curvature function peaks at one place indicating the band crossing is one. The peak grows as $\alpha \to \alpha_c$ and it diverges at $\alpha = \alpha_c$ with the peak flipping.

Consider the rotation angle α as the tuning parameter, we find that the energy bands can close their gap at different values of k_x, k_y not limited to 0 and π. Nevertheless, the divergence and flipping of the curvature function always hold

$$\lim_{\alpha\to\alpha_c^-} F(k_x = k_c, k_y = k_c, \alpha) = -\lim_{\alpha\to\alpha_c^+} F(k_x = k_c, k_y = k_c, \alpha) = \pm\infty, \quad (4.114)$$

indicating that the curvature function can be invoked to study the critical behavior of the system. As $\alpha \to \alpha_c$, we observe the emergence of a single peak for curvature function (see Fig. 4.22). Therefore, the Peak-divergence scenario is applicable for this protocol and the band crossing is one. For the sake of brevity and simplicity, we set $k_y = -k_x$. In such a case, the gap-closure happens at $k_x = k_c = \pi/2$. The curvature function and the length scale at the critical points are

$$\begin{aligned} F(k_x = -k_y = \frac{\pi}{2}, \alpha) &= \frac{2\mathrm{Sig}(\kappa_\alpha)\left(\lambda_{2(\alpha-\beta)} - \lambda_{2\alpha} - \lambda_{2\beta}\right)}{1-\kappa_{2\alpha}}, \\ \xi_x^2(k_x = -k_y = \frac{\pi}{2}, \alpha) &\approx \frac{\Xi}{(1-\kappa_{2\alpha})^{\frac{1}{2}}}, \end{aligned} \quad (4.115)$$

in which

$$\Xi = \quad 2\sqrt{2}\kappa_\alpha(2\lambda_\beta^2(5+2\kappa_{2\alpha}+\kappa_{2\beta}) - \lambda_{2\beta}\cot\left(\frac{\alpha}{2}\right)(3\kappa_{2\beta}+\kappa_{2\alpha}-4)).$$

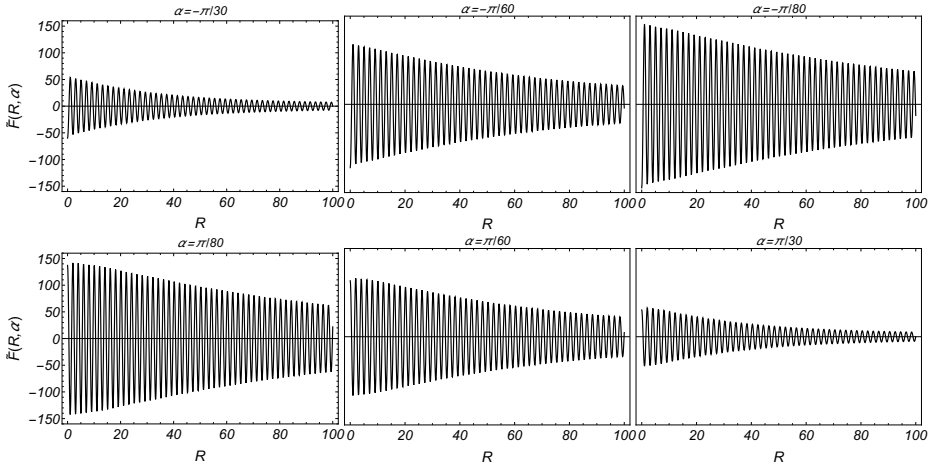

Figure 4.23: Correlation function, $\tilde{F}_{1D}(R,\alpha)$, as a function of R for $\beta = \pi/2$ with $k_y = -k_x$. The diagrams show decay of the correlation function via a damped oscillation. At the critical point, the correlation function similar to the curvature function also flips.

If $\beta = \pi/2$, critical point would be $\alpha_c = 0$, in which we find the critical exponents $\gamma = 2$ and $\nu = 1$, and the scaling law is valid through $\gamma = D\nu$ with $D = 2$. This is in agreement with the results in Refs. (Chen and Schnyder, 2019; Molignini et al., 2020).

Next, we find the correlation function starting from the stroboscopic eigenstates of the Hamiltonian

$$|\psi_{\mathbf{k}\pm}\rangle = \frac{1}{\sqrt{2n(n \pm n_z)}} \begin{pmatrix} n_z \pm n \\ n_x + in_y \end{pmatrix}, \tag{4.116}$$

which shows that stroboscopic Berry Curvature of the filled band eigenstates coincides with the curvature function

$$\partial_{k_x}\langle\psi_{\mathbf{k}-}|\partial_{k_y}|\psi_{\mathbf{k}-}\rangle - \partial_{k_y}\langle\psi_{\mathbf{k}-}|\partial_{k_x}|\psi_{\mathbf{k}-}\rangle = \frac{1}{2}F(\mathbf{k},\alpha,\beta),$$

Therefore, the Fourier transform of the curvature function, hence correlation function measures the overlap of the stroboscopic Wannier states according to Eq. (4.103). Moreover, using the Lorentzian shape in Eq. (4.96), the Fourier transform

$$\tilde{F}_{2D}(\mathbf{R},\alpha) \approx \frac{1}{2}\int \frac{d^2\mathbf{k}}{(2\pi)^2}\frac{F(\mathbf{k}_c,\alpha)}{1+\xi^2\delta\mathbf{k}^2}, \tag{4.117}$$

which gives a correlation function that decays with $\mathbf{R}$ where the correlation length is ξ. If we set $k_y = -k_x$ ($R_y = -R_x$), the decay of the correlation function would be through a damped oscillation which is due to the presences of at least two peaks in curvature function (see Fig. 4.23).

4.3 POSSIBLE EXPERIMENTAL REALIZATIONS

The experimental realizability of the quantum walks with the step-dependent coin is another issue that we address here. The quantum walk has been experimentally realized in different platforms such as neutral atoms (Karski et al., 2009), ions (Schmitz et al., 2009; Zähringer et al., 2010), photons (Schreiber et al., 2010; Bian et al., 2015; Barkhofen et al., 2018), Bose-Einstein condensation (Dadras et al., 2018), optical networks (Lorz et al., 2019) and etc. It can be also implemented in electric (Genske et al., 2013) or magnetic fields (Sajid et al., 2019). As for the simulation of the topological phases with quantum walks, it has been implemented and addressed in many references (Kitagawa et al., 2012; Barkhofen et al., 2017; Flurin et al., 2017; Zhan et al., 2017; Wang et al., 2018; Nitsche et al., 2019; Xu et al., 2020; D'Errico et al., 2020).

Using these implemented experiments, we can come up with specific methods to realize the quantum walk with step-dependent coins. The first proposal is inspired by an earlier work of Schreiber et al. (Schreiber et al., 2010). The quantum walk is done with passive optical elements. The walker is a photon and internal states are its polarizations. The coin operator is made of a combination of the half- and quarter-wave plates. The initial state is provided by half- and quarter-wave plates as well.

The internal states are limited to Horizontal and Vertical polarizations. Each step contains separation of the horizontal and vertical components of the polarization spatially and temporally, then their recombination, and being sent back to the input beam splitter for the next step. Each step of the walk is equivalent to one loop. At each step, one can couple out the photon out of the loop with 50 percent probability. In an occurrence of such a case, an avalanche photodiode registers a click. This click is recorded by a computer via a time-to-digital converter interface. The walk is characterized by a combination of these clicks which are due to a series of consecutive runs of the experiment.

In 2015, Xu et al. employed a similar principle to implement a quantum walk with varying coins which is a walk with step-dependent coin (Xue et al., 2015). In their proposal, the coin operator is realized by a series of half- and quarter-wave plates. The photon passes through these half- and quarter-wave plates which change its polarization. Afterward, first, it passes a beam splitter which separates the two polarization from one another, and then it passes through a beam displace which plays the role of the shift operator. The same is repeated in a longitudinal axis which provides us the quantum walk that we have in mind.

Finally, the last proposal is motivated by the work of Flurin et al. in which the quantum walk is done with ion trap and cavity modes (Flurin et al., 2017). In this scheme, the ion is trapped in a cavity and coupled with modes of the cavity. The ion provides the internal degrees of freedom for the walker while the walker is the cavity mode and its position is the mode's number. The ion is limited to specific levels and with the help of laser beams, its level is modified from one to another.

While we have outlined three possible scenarios for the realization of the quantum walk with step-dependent coin, it is possible to realize it in other systems as well. As for the simulation of topological phases described before, one can use the Flurin et al. in which they explicitly measured topological invariant with their setup.

4.4 CONCLUSION

In this chapter, we investigated the quantum walks with step-dependent coins and their applications in simulations of the topological phases. We established that utilization of the step-dependent coins in the quantum walks provides us with a high level of control over the walker's behavior. In fact, we were able to incorporate different characteristics in the walker's properties such as localization, trapped, classical- and quantum-like behaviors, and mimicking quantum walks in the presence of noise. This expresses and emphasizes the capability of the quantum walk as stand-alone machinery that provides us with diverse behaviors. This is a crucial qualification for a platform that is used for simulating other systems (one of the end goals of the quantum walks).

Recently, Katayama et al. showed that a quantum walk with step-dependent coins can transfer the state of the walker in a controlled and precise manner (Katayama et al., 2020). In addition, such a walk can manipulate the desired state on demand. These two properties are among the requirements for a computational model being a universal quantum computation primitive. Another application of the quantum walk with the step-dependent coin is in Parrondo's paradox (Pires and Queirós, 2020). In nutshell, Parrondo's paradox indicates that two losing games while on their own result in losing outcomes, if combined, they can produce a winning game. It was shown that using the quantum walk with step-dependent coins, one can indeed realize Parrondo's paradox.

In the other application of the quantum walks with step-dependent coins, we built different protocols of the quantum walk to simulate topological phases and boundary states that are observed in one-, two- and three-dimensional systems in condensed matter. While we were able to simulate the topological phenomena in

different dimensions, we also simulated multiphase configuration and multicriticality. Multiphase configuration and multicriticality are observed in the Floquet type of the topological phases and here, we were able to show that the quantum walks are indeed capable of simulating these phenomena as well.

The step-dependency was one of the features of the simulated topological phases and boundary states. The step-dependency provides us with the possibility of engineering the simulated topological phenomena via step number of the walk. In fact, we are able to specify the type of the topological phases and boundary states, their numbers, presences and/or absence, and finally where they can occur. This gives us a high level of control over the simulation of the topological phases and enables us to readily investigate different systems of topological phases in a more simplified manner.

Finally, we were able to show that one is able to extract the critical exponents, curvature function, and correlation function for the simulated topological phenomena with the quantum walks. This means that we are able to describe the critical behaviors of the topological phases in different systems via the parameters of the quantum walks. In this study, we only explored the critical behavior of the one-dimensional BDI and two-dimensional D classes and left the other classes of topological phases for future works.

5

DISCRETE-TIME QUANTUM WALK WITH ENTANGLED QUBITS

Entanglements and the possibility of entangling particles are the key features of quantum mechanics that have no classical counterpart. In fact, over the years, it has been argued that counter-intuitive occurrences in quantum mechanics are due to these features. In return, it was shown that entanglement and entangling qubits could be used as resources in quantum-mechanical systems. These resources were utilized in the emerging fields of superdense coding (Muralidharan and Panigrahi, 2008), teleportation (Bouwmeester et al., 1997), cryptography (Ekert, 1991), quantum computation (Jozsa and Linden, 2003) and algorithm developments (Hirsch et al., 2016).

Naturally, the quantum walk as a field of quantum information and computation could use these resources as well to attain better efficiency for the walker's properties or introduce new phenomena. In addition to these motivations, we have another line of motivation to carry out our study concerning the quantum walk with entangled qubits; we explore the possibility of using the entanglement as a means to engineer the behavior and the properties of the walker. Therefore, in what follows, we propose a scheme in which we have a walker with four internal states. The internal states of the walker are resulted from two entangled qubits.

Parts of the material presented in this chapter were published previously in the following reference:

> *One-dimensional quantum walks driven by two-entangled-qubit coins*
> S. Panahiyan and S. Fritzsche
> Phys. Lett. A **384**, 126673 (2020).

5.1 QUANTUM WALK WITH TWO ENTANGLED QUBITS

In contrast to usual studies in which two walkers are considered to be entangled, we consider having a walker that has two entangled qubits building up its internal

states. A simple physical realization of such a system is when we put two entangled ions in a trap and couple them with a cavity mode. The cavity mode will be our walker and entangled ions provide the internal states for it.

5.1.1 *Setup of the walk*

We have a single walker that has a one-dimensional position space. Therefore, the Hilbert space of the position, $\mathcal{H}_P$, is spanned by $\{|x\rangle : x \in \mathbb{Z}\}$. The internal states are products of the entanglement between two qubits each having two states. This indicates that coin Hilbert space, $\mathcal{H}_C$, is spanned by $\{|\uparrow\uparrow\rangle\,, |\uparrow\downarrow\rangle\,, |\downarrow\uparrow\rangle\,, |\downarrow\downarrow\rangle\}$. The total Hilbert space of the walk is then given by $\mathcal{H} \equiv \mathcal{H}_P \otimes \mathcal{H}_C$.

To find a proper coin operator, one should take the entanglement into consideration. This means we can use two single-qubit coin operators (sub-coins) and their tensor products to build the coin operator. The sub-coins are given by (Panahiyan and Fritzsche, 2020b)

$$\widehat{C}_\theta = \cos(\theta)\,|\uparrow\rangle\langle\uparrow| + \sin(\theta)\,|\uparrow\rangle\langle\downarrow| + \sin(\theta)\,|\downarrow\rangle\langle\uparrow| - \cos(\theta)\,|\downarrow\rangle\langle\downarrow|\,, \tag{5.1}$$

$$\widehat{C}_\gamma = \cos(\gamma)\,|\uparrow\rangle\langle\uparrow| + \sin(\gamma)\,|\uparrow\rangle\langle\downarrow| + \sin(\gamma)\,|\downarrow\rangle\langle\uparrow| - \cos(\gamma)\,|\downarrow\rangle\langle\downarrow|\,, \tag{5.2}$$

in which the sub-coins are understood as rotation matrices with rotation angles of θ and γ. It should be noted that the coin operators can be decomposed via Pauli matrices in forms of Pauli-X and -Z gates as $\widehat{C}_\theta = \cos(\theta)\sigma_Z + \sin(\theta)\sigma_X$ and $\widehat{C}_\gamma = \cos(\gamma)\sigma_Z + \sin(\gamma)\sigma_X$. In what follows, we call the Pauli matrices of σ_x and σ_z, Pauli-X and -Z gates, respectively. Using the sub-coins, one can find the total coin operator of the quantum walk as

$$\begin{aligned}
\widehat{C} = \widehat{C}_\gamma \otimes \widehat{C}_\theta \;=\; & |\uparrow\uparrow\rangle\,(\cos(\theta)\,\cos(\gamma)\,\langle\uparrow\uparrow| + \cos(\theta)\,\sin(\gamma)\,\langle\uparrow\downarrow| \\
& + \sin(\theta)\,\cos(\gamma)\,\langle\downarrow\uparrow| + \sin(\theta)\,\sin(\gamma)\,\langle\downarrow\downarrow|) \;+ \\
& |\uparrow\downarrow\rangle\,(\cos(\theta)\,\sin(\gamma)\,\langle\uparrow\uparrow| - \cos(\theta)\,\cos(\gamma)\,\langle\uparrow\downarrow| \\
& + \sin(\theta)\,\sin(\gamma)\,\langle\downarrow\uparrow| - \cos(\theta)\,\sin(\gamma)\,\langle\downarrow\downarrow|) \;+ \\
& |1\uparrow\rangle\,(\sin(\theta)\,\cos(\gamma)\,\langle\uparrow\uparrow| + \sin(\theta)\,\sin(\gamma)\,\langle\uparrow\downarrow| \\
& - \cos(\theta)\,\cos(\gamma)\,\langle\downarrow\uparrow| - \cos(\theta)\,\sin(\gamma)\,\langle\downarrow\downarrow|) \;+ \\
& |\downarrow\downarrow\rangle\,(\sin(\theta)\,\sin(\gamma)\,\langle\uparrow\uparrow| - \sin(\theta)\,\cos(\gamma)\,\langle\uparrow\downarrow| \\
& - \cos(\theta)\,\sin(\gamma)\,\langle\downarrow\uparrow| + \cos(\theta)\,\cos(\gamma)\,\langle\downarrow\downarrow|).
\end{aligned} \tag{5.3}$$

The application of the coin operator creates a superposition of the internal states. We call the rotation angles, θ and γ, coin's parameters since they parametrize the coin operator. Since the walker moves in the one-dimensional position space, the conditional shift operator can be given in the form of

$$\begin{aligned}\widehat{S} &= |\uparrow\uparrow\rangle\langle\uparrow\uparrow| \otimes \sum |x+1\rangle\langle x| + (|\downarrow\uparrow\rangle\langle\downarrow\uparrow| + |\uparrow\downarrow\rangle\langle\uparrow\downarrow|) \otimes \sum |x\rangle\langle x| + \\ &\quad |\downarrow\downarrow\rangle\langle\downarrow\downarrow| \otimes \sum |x-1\rangle\langle x|, \end{aligned} \tag{5.4}$$

which indicates that at each step, the walker can move to the right, left, or remain in the same position.

The protocol of the quantum walk is simple-step and the quantum walk is resulted via

$$|\psi_j\rangle_{Fin} = \widehat{U}^T |\psi_j\rangle_{Int} = [\widehat{S}\widehat{C}]^T |\psi_j\rangle_{Int}, \tag{5.5}$$

in which j represents the initial state that is used. We consider two types of initial states

$$|\psi_1\rangle_{Int} = (\cos(\eta)|\uparrow\uparrow\rangle + e^{I\phi}\sin(\eta)|\downarrow\downarrow\rangle) \otimes |0\rangle, \tag{5.6}$$

$$|\psi_2\rangle_{Int} = (\cos(\alpha)|\downarrow\uparrow\rangle + e^{I\phi}\sin(\alpha)|\uparrow\downarrow\rangle) \otimes |0\rangle, \tag{5.7}$$

which are inspired by Bell states. The amount of initial entanglement between the qubits is determined by η and α. ϕ is a phase factor that controls the interference between the internal states of the initial state through the walk. The complete isolation of the interfere could happen if $\phi = \pi/2$. Note that by setting $\phi = 0$ and π with $\eta = \alpha = \pi/4$ in Eqs. (5.6) and (5.7), the initial states reduce to Bell states which are maximally entangled.

Before we proceed, for the sake of clarification, we introduce a few terminologies which we will use later. Two-peaks-zone indicates that there are two major peaks in the probability density distribution of the walker in the position space. Similarly, Three- and Four-peaks-zone point to three and four major peaks. The most left- and right-hand sides positions are called extreme zones.

The two sub-coins building up the coin operator could be identical ($\theta = \gamma$). This means that the qubits are modified identically through the application of the coin. In contrast, if $\theta \neq \gamma$, the sub-coins would be different indicating that the two qubits are modified at different ratios. We call these cases *identical sub-coins* and *non-identical sub-coins*, respectively. In what follows, we only focus on the case of identical sub-coins. Finally, for different parameters, we have $\eta, \theta, \phi, \alpha, \beta \in [0, \pi/2]$.

θ	$\|\psi_1\rangle_{\text{Int}}$	$\|\psi_2\rangle_{\text{Int}}$
$\theta = 0$	*Localized in two positions*	*Localized in one position*
$\theta \to 0$	*Two-peaks-zone*	*Three-peaks-zone*
$\theta \to \pi/2$	*Gaussian*	*Gaussian*
$\theta = \pi/2$	*Localized in one position*	*Localized in one position*
Otherwise	*Three- and Four-peaks-zone*	*Three- and Four-peaks-zone*

Table 5.1: Type of the probability density distribution as a function of coin's rotation angle for $\theta = \gamma$. The initial states' parameters change the amplitudes of the probability density in positions but do not change the type of the distribution.

5.1.2 *Probability density distribution and classification*

The behavior of the walker in position space highly depends on whether sub-coins are identical or not and which internal states are used in the initial state of the walker. To have a better picture, we discuss cases of identical sub-coins with the two intitial states in more details.

Generally speaking, the variance and type of the probability density distribution is determined by the rotation angle, hence the coin's proprieties (see Fig. 5.1). In contrast, the symmetry of the distribution and probability densities in each position are determined by internal states that are used in the initial state and the amount of initial entanglement between the qubits in the initial state of the quantum walk (see Fig. 5.1).

In general, the probability density distributions are in the forms of Three- and Four-peaks-zone types. If the sub-coins are Pauli-X gates ($\theta = \pi/2$), the probability density distribution becomes completely localized in the initial position or the two neighboring positions (see Fig. 5.1). This behavior remains intact through the evolution of the walk which indicates that the walker is trapped. For $\theta \to \pi/2$, the coin approximating to Pauli-X gate, we detect a Gaussian distribution, hence classical-like behavior. This is valid for both of the initial states. In contrast, for sub-coins being Pauli-Z gates, we observe significantly different behavior for the walker with different initial states. In the case of initial states of (5.6), the probability density distribution localizes equally in two positions. This localization is mobile and in the mobility of the localization, perfect transfer with the highest velocity to both left- and right-sides positions takes place. In contrast, for the initial state of (5.7), the walker shows trapped behavior with complete localization at the initial position or around it. For $\theta \to 0$, we find Two-peaks-zone in case of (5.6) and Three-peaks-zone for (5.7). Therefore, the type of probability density distribution and walker's behaviors are determined by the internal states that are used for initial state and rotation angles.

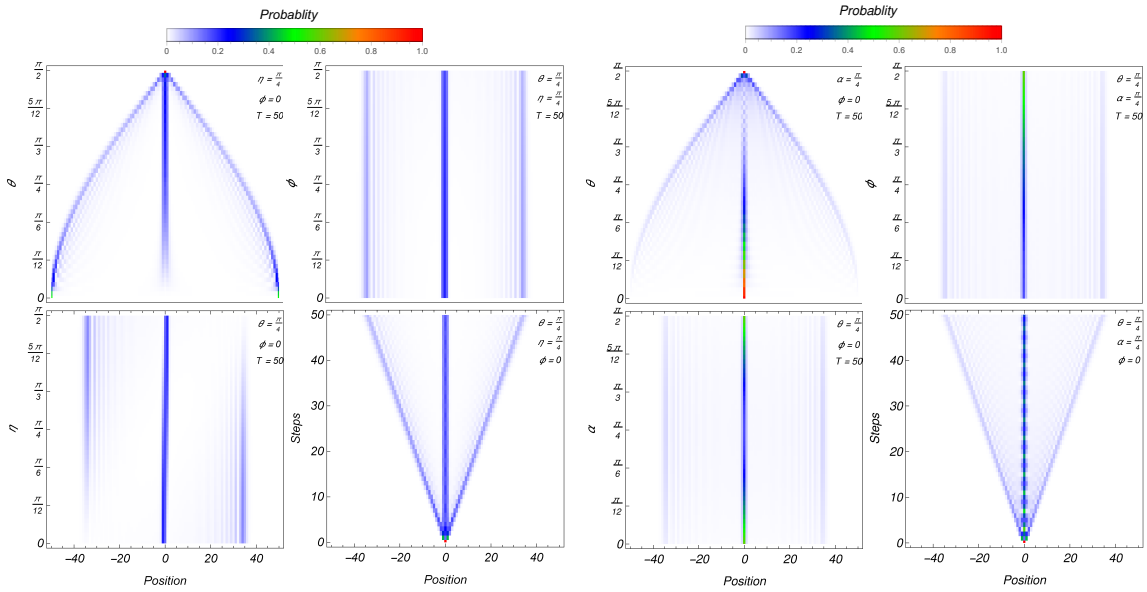

Figure 5.1: Probability density distributions for initial states of $|\psi_1\rangle_{Int}$ (left panel) and $|\psi_2\rangle_{Int}$ (right panel). In the left panel, the symmetrical probability density distribution is conditioned to have a maximally entangled initial state. Gaussian distribution is found when the sub-coins approximate to Pauli-X gates while for Pauli-X gates, the walker becomes completely trapped. In the case of Pauli-Z gate sub-coins, a perfect transfer with the highest velocity to both left- and right-sides positions for the walker is observed. In the right panel, the symmetry of probability density distribution is independent of entanglement in the initial state and the entanglement only modifies the places where it is more probable to find the walker.

This is in contrast to the quantum walk with two internal states where the type of probability density distribution is independent of the internal states in the initial state. In table 5.1, we have summarized the discussion of this paragraph.

As for the effects of amplitudes of different internal states on the walker's properties, we have different behaviors for the initial states. In the case of the initial state of (5.6), the probability densities of the left(right) hand side positions are increasing (decreasing) functions of η while central probability density approximately is fixed and independent of it (see Fig. 5.1). Interestingly, the symmetrical probability density distribution is found if the initial state is maximally entangled ($\eta = \pi/4$). In contrast, the symmetry of probability density distribution is independent of α in the initial state of (5.7). Therefore, the initial entanglement between the qubits only changes the values of probability densities. The central probability densities are decreasing functions of the initial entanglement between the qubits while the ones in the extreme zones are increasing functions of it. The contribution of variation in phase parameter (ϕ) is determined by the internal states that are used in the initial state. For the initial state of (5.6), ϕ insignificantly affects the probability densities in each position, while

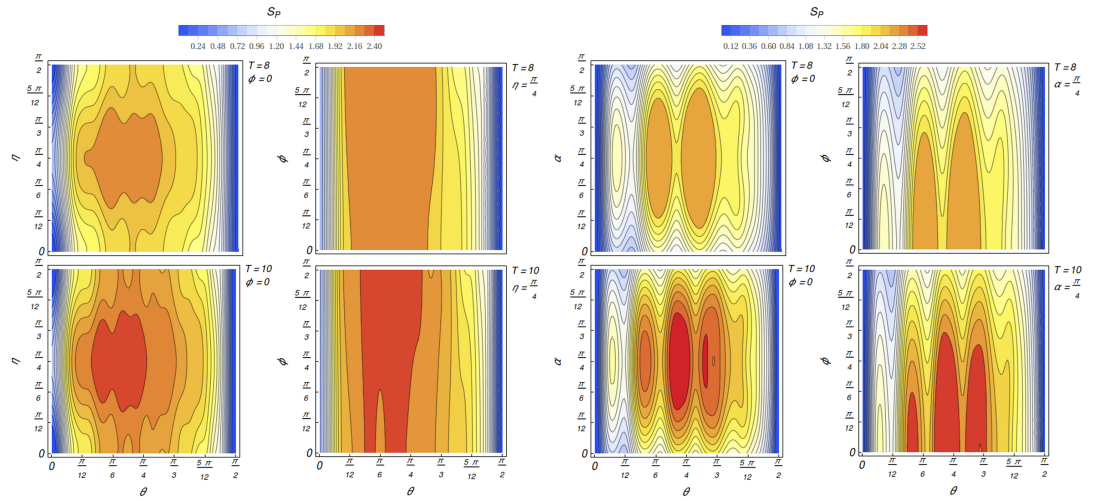

Figure 5.2: Entropy of position space as a function of coin's and initial state's parameters for steps 8 and 10 with initial states $|\psi_1\rangle_{\mathrm{Int}}$ (left panel) and $|\psi_2\rangle_{\mathrm{Int}}$ (right panel). The minimized entropy is found if sub-coins approximate to Pauli-X and Z gates or become these gates, and the initial entanglement between the two qubits becomes zero (two qubits become separable). In contrast, maximized entropy emerges if the initial state is maximally entangled. The entropy's behavior is symmetrical with respect to $\eta = \alpha = \pi/4$.

in the case of the initial state of (5.7), the effect of variation of ϕ on central probability densities is more evident.

In the case of localization, Pauli-X and Z gates for sub-coins, the variance is almost zero. Otherwise, the variance is a decreasing function of the θ. Except for the localized cases, the variance monotonically increases as the walk proceeds. The analytical description of our discussion is provided in 7.4.

5.1.3 *Entropy of the walk*

Next, we investigate the modification of entropy as a function of coin's and initial state's parameters and clarify the role of the entanglement between the qubits on this quantity. We are only concerned with the entropy in position space. To find the entropy, one should use von Neumann's method. This includes the calculation of the density matrix and tracing over the internal states to find the entropy in position space. Since the system is pure, the von Neumann entropy coincides with Shannon entropy. Therefore, the entropy can be calculated with Eq. (4.6).

The entropy is an increasing function of the step number of the quantum walk. The only exception is for localized cases in which the entropy would vanish. If we exclude vanishing cases of entropy, the minimization of the entropy happens when two conditions are met: I) sub-coins approximate to Pauli-X and Z gates or become

these gates, and II) the initial entanglement between the qubits is zero (see Fig. 5.2). In contrast, the entropy maximizes when the initial state is maximally entangled ($\eta = \alpha = \pi/4$) and the rotation angles of the sub-coins approach Hadamard gates, $\pi/4$. On the other hand, studying the entropy's behavior, we observe a symmetrical property with respect to $\eta = \alpha = \pi/4$. As for the phase factor, ϕ, in the case of the initial state of (5.6), the entropy is not a sensitive function of the phase factor, while the effects of its variation moderately modify entropy in the case of the initial state of (5.7).

5.2 CONCLUSION

In this chapter, we studied the quantum walks with entangled qubits. In our investigation, we confirmed one can readily control the walker's behavior in position space by modifying the initial entanglement between the entangled qubits. In fact, we showed that depending on qubits' states in the initial state of the walker and how these qubits are modified by the coin operator, we are able to change the walker's behavior from trapped or localized walker to a ballistic one.

We were also able to specify where the walker is most probable to be found by tuning the initial entanglement between the qubits. This makes the entanglement between the qubits an additional tool for controlling the walker. Such a tool is absent in the classical walk. Therefore, we were able to highlight one of the differences that entanglement as a resource in quantum systems can play.

6

CONCLUSIONS AND OUTLOOK

In this dissertation, we studied the discrete-time quantum walks and their applications in two different proposals. The first proposal incorporated step-dependent coins in the protocols of the quantum walks. In the second proposal, we investigated the quantum walks with entangled qubits. The main goal in both of these proposals was attaining a high level of control over the walker, its properties, and in general the discrete-time quantum walks. The necessity of such a control rises from the applications of the quantum walks in developing quantum algorithms as well as their role in simulating other quantum systems and phenomena.

First, we introduced the stochastic processes and their roles in developing necessary frameworks to explain and estimates the behaviors of systems observed in different branches of the science (Sec. 2.1). Later, we gave a brief review of the random walks as one of the sub-branches of Markovian stochastic processes (Sec. 2.2). The random walks are divided into two classes known as classical and quantum random walks. The classical random walks use the principles of classical mechanics to perform the walks whereas the quantum walks equip the quantum mechanics to do the same.

In Chap. 3, we firstly reviewed the discrete-time quantum walk in the one-dimensional position space with two internal states. The theoretical framework for such a quantum walk was outlined and it was shown that discrete-time quantum walk is quadratically faster than its classical counterpart. Next, we presented the method of the stationary phases as an analytical approach to study the limit behavior of the discrete-time quantum walk. As two of the important applications of the discrete-time quantum walks, we reviewed a series of algorithms developed by quantum walks and simulations of topological phases observed in condensed matter with the discrete-time quantum walks. In both cases, we met a question concerning attaining a high level of the control over walker's properties and its behavior.

Motivated by this question, in Chap. 4, we introduced our first proposal to attain a better control in the discrete-time quantum walks. In this proposal, we considered the coin operators, building blocks of the protocols of discrete-time quantum walks, to modify step-dependently. This step-dependency induces a dynamical nature for

the protocols of the quantum walks. This dynamical nature enabled us to control the walker's behavior by tuning the coins' parameters and step number of the walks. In fact, we were able to introduce characterizations such as localization, trapped, diffusive, and ballistic into the walker's properties. This provided us with a unitary and pure operation that produces diverse behaviors without resorting to decoherence as a controlling factor to achieve such a goal.

In the application of discrete-time quantum walks with step-dependent coins, we built necessary protocols for simulating topological phases and boundary states that are observable in condensed matter. In our formalism, we were able to simulate all types of topological phases and boundary states that can be observed in one- two- and three-dimensional systems. The step-dependency of coins resulted in step-dependent properties for the simulations which in return enabled us to readily control the simulated topological phenomena. The controlling factor, in this case, was the step number of the walks. By tuning the step number of the walks, we determined the type of topological phases and boundary states, their occurrences or absences, their numbers, and even where they could happen.

The simulated topological phenomena had several exotic results. One of these results was the formation of cell-like structures containing all types of boundary states and topological phases in BDI class of the topological phases. The second issue was multiphase configuration and multicriticality which are characteristic behaviors observed in topological phases of driven systems. Finally, we were able to extract the critical exponents and curvature function of the simulated topological phenomena around the critical points and show the decay of the correlation function for them. This enabled us to quantify the critical behaviors of the systems with parameters of the discrete-time quantum walks.

In the other proposal, we took the advantages of the quantum-mechanical principles of entanglement and entangled qubits, and introduced the discrete-time quantum walks with entangled qubits. We showed that the entangled qubits and their initial entanglement can be used as tools to modify the properties of the walker. In fact, by tuning the initial entanglement between the qubits, we were able to specify the determinateness of the walker's behavior as well as properties such as the most probable place to find the walker. In addition, we were able to show that discrete-time quantum walks with entangled qubits enable one to steer the walker's behavior from localized and trapped to diffusive and ballistic ones.

The emergences of multiphase configuration and multicriticality in our simulations indicate that the potential of the discrete-time quantum walks as simulators of the topological phases and boundary states exceed the expectation. The question arises whether other topological phenomena can be simulated by discrete-time quantum

walks. Specifically, phases such as Weyl semimetallic phases have yet to be addressed in the context of the discrete-time quantum walks.

In our study of the critical properties of the simulated topological phases, we only concentrated on two classes of the topological phases. Considering that there are at least 13 more classes of the topological phases in one, two, and three dimensions, one can concentrate on formalizing the critical properties of simulated topological phases for them. A uniform approach to the analytical description of the discrete-time quantum walk with the step-dependent coin is yet another question that must be addressed. This issue becomes important due to the universal primitive nature of this quantum walk.

In the context of the quantum walk with entangled qubits, the first issue to follow would be the simulations of the topological phases and boundary states with them. Such a quantum walk can produce Hamiltonian with four bands of energy. Given the driven nature of the quantum walk, one can expect emergence of qualitatively different types of simulated topological phenomena for the quantum walk with entangled qubits. It should be noted that the task involves building protocols for different classes of topological phases in one, two, and three dimensions. This requires careful examination of different shift and coin operators which yield the desirable symmetries for the protocol of the walk and simulate all types of topological phases and boundary states.

Finally, generalization to an arbitrary number of entangled qubits with different coin and shift operators is yet another issue that can be followed. The applications of such walks in the simulations of the topological phases is another issue that can be addressed independently.

BIBLIOGRAPHY

Aaronson, S. and Y. Shi (July 2004). "Quantum Lower Bounds for the Collision and the Element Distinctness Problems." In: *J. ACM* 51.4, 595–605. DOI: 10.1145/1008731.1008735.

Aharonov, D., A. Ambainis, J. Kempe, and U. Vazirani (2001). "Quantum Walks on Graphs." In: *Proceedings of the Thirty-Third Annual ACM Symposium on Theory of Computing*. STOC '01. Hersonissos, Greece: Association for Computing Machinery, 50–59. DOI: 10.1145/380752.380758.

Aharonov, Y., L. Davidovich, and N. Zagury (1993). "Quantum random walks." In: *Phys. Rev. A* 48 (2), pp. 1687–1690. DOI: 10.1103/PhysRevA.48.1687.

Ambainis, A. (2004). "Quantum walk algorithm for element distinctness." In: pp. 22–31. DOI: 10.1109/FOCS.2004.54.

Ambainis, A., E. Bach, A. Nayak, A. Vishwanath, and J. Watrous (2001). "One-Dimensional Quantum Walks." In: *Proceedings of the Thirty-Third Annual ACM Symposium on Theory of Computing*. STOC '01. Hersonissos, Greece: Association for Computing Machinery, 37–49. DOI: 10.1145/380752.380757.

Armitage, N. P., E. J. Mele, and A. Vishwanath (2018). "Weyl and Dirac semimetals in three-dimensional solids." In: *Rev. Mod. Phys.* 90 (1), p. 015001. DOI: 10.1103/RevModPhys.90.015001.

Asbóth, J. K. (2012). "Symmetries, topological phases, and bound states in the one-dimensional quantum walk." In: *Phys. Rev. B* 86 (19), p. 195414. DOI: 10.1103/PhysRevB.86.195414.

Asbóth, J. K. and H. Obuse (2013). "Bulk-boundary correspondence for chiral symmetric quantum walks." In: *Phys. Rev. B* 88 (12), p. 121406. DOI: 10.1103/PhysRevB.88.121406.

Barkhofen, S., L. Lorz, T. Nitsche, C. Silberhorn, and H. Schomerus (2018). "Supersymmetric Polarization Anomaly in Photonic Discrete-Time Quantum Walks." In: *Phys. Rev. Lett.* 121 (26), p. 260501. DOI: 10.1103/PhysRevLett.121.260501.

Barkhofen, S., T. Nitsche, F. Elster, L. Lorz, A. Gábris, I. Jex, and C. Silberhorn (2017). "Measuring topological invariants in disordered discrete-time quantum walks." In: *Phys. Rev. A* 96 (3), p. 033846. DOI: 10.1103/PhysRevA.96.033846.

Bernevig, B. A., T. L. Hughes, and S.-C. Zhang (2006). "Quantum Spin Hall Effect and Topological Phase Transition in HgTe Quantum Wells." In: *Science* 314.5806,

pp. 1757–1761. DOI: 10.1126/science.1133734. eprint: https://science.sciencemag.org/content/314/5806/1757.full.pdf.

Bian, Z., J. Li, H. Qin, X. Zhan, R. Zhang, B. C. Sanders, and P. Xue (2015). "Realization of Single-Qubit Positive-Operator-Valued Measurement via a One-Dimensional Photonic Quantum Walk." In: *Phys. Rev. Lett.* 114 (20), p. 203602. DOI: 10.1103/PhysRevLett.114.203602.

Bouwmeester, D., J.-W. Pan, K. Mattle, M. Eibl, H. Weinfurter, and A. Zeilinger (1997). "Experimental quantum teleportation." In: *Nature* 390.6660, pp. 575–579. DOI: 10.1038/37539.

Buhrman, H., C. Dürr, M. Heiligman, P. Høyer, F. Magniez, M. Santha, and R. de Wolf (2005). "Quantum Algorithms for Element Distinctness." In: *SIAM Journal on Computing* 34.6, pp. 1324–1330. DOI: 10.1137/S0097539702402780. eprint: https://doi.org/10.1137/S0097539702402780.

Burkov, A. A. (2016). "Topological semimetals." In: *Nature Materials* 15.11, pp. 1145–1148. DOI: 10.1038/nmat4788.

Cardano, F., A. D'Errico, A. Dauphin, M. Maffei, B. Piccirillo, C. de Lisio, G. De Filippis, V. Cataudella, E. Santamato, L. Marrucci, M. Lewenstein, and P. Massignan (2017). "Detection of Zak phases and topological invariants in a chiral quantum walk of twisted photons." In: *Nature Communications* 8.1, p. 15516. DOI: 10.1038/ncomms15516.

Cardano, F., M. Maffei, F. Massa, B. Piccirillo, C. de Lisio, G. De Filippis, V. Cataudella, E. Santamato, and L. Marrucci (2016). "Statistical moments of quantum-walk dynamics reveal topological quantum transitions." In: *Nature Communications* 7.1, p. 11439. DOI: 10.1038/ncomms11439.

Chen, T., B. Wang, and X. Zhang (2018). "Characterization of topological phases and selection of topological interface modes in the parity-time-symmetric quantum walk." In: *Phys. Rev. A* 97 (5), p. 052117. DOI: 10.1103/PhysRevA.97.052117.

Chen, W. and A. P. Schnyder (2019). "Universality classes of topological phase transitions with higher-order band crossing." In: *New Journal of Physics* 21.7, p. 073003. DOI: 10.1088/1367-2630/ab2a2d.

Childs, A. M. (2009). "Universal Computation by Quantum Walk." In: *Phys. Rev. Lett.* 102 (18), p. 180501. DOI: 10.1103/PhysRevLett.102.180501.

Chiu, C.-K., J. C. Y. Teo, A. P. Schnyder, and S. Ryu (2016). "Classification of topological quantum matter with symmetries." In: *Rev. Mod. Phys.* 88 (3), p. 035005. DOI: 10.1103/RevModPhys.88.035005.

Clauset, A., M. Kogan, and S. Redner (2015). "Safe leads and lead changes in competitive team sports." In: *Phys. Rev. E* 91 (6), p. 062815. DOI: 10.1103/PhysRevE.91.062815.

Codling, E. A., M. J. Plank, and S. Benhamou (2008). "Random walk models in biology." In: *Journal of The Royal Society Interface* 5.25, pp. 813–834. DOI: 10.1098/rsif.2008.0014. eprint: https://royalsocietypublishing.org/doi/pdf/10.1098/rsif.2008.0014.

Coifman, R. R., S. Lafon, A. B. Lee, M. Maggioni, B. Nadler, F. Warner, and S. W. Zucker (2005). "Geometric diffusions as a tool for harmonic analysis and structure definition of data: Diffusion maps." In: *Proceedings of the National Academy of Sciences* 102.21, pp. 7426–7431. DOI: 10.1073/pnas.0500334102. eprint: https://www.pnas.org/content/102/21/7426.full.pdf.

D'Errico, A., F. Cardano, M. Maffei, A. Dauphin, R. Barboza, C. Esposito, B. Piccirillo, M. Lewenstein, P. Massignan, and L. Marrucci (2020). "Two-dimensional topological quantum walks in the momentum space of structured light." In: *Optica* 7.2, pp. 108–114. DOI: 10.1364/OPTICA.365028.

Dadras, S., A. Gresch, C. Groiseau, S. Wimberger, and G. S. Summy (2018). "Quantum Walk in Momentum Space with a Bose-Einstein Condensate." In: *Phys. Rev. Lett.* 121 (7), p. 070402. DOI: 10.1103/PhysRevLett.121.070402.

Ekert, A. K. (1991). "Quantum cryptography based on Bell's theorem." In: *Phys. Rev. Lett.* 67 (6), pp. 661–663. DOI: 10.1103/PhysRevLett.67.661.

Farhi, E. and S. Gutmann (1998). "Quantum computation and decision trees." In: *Phys. Rev. A* 58 (2), pp. 915–928. DOI: 10.1103/PhysRevA.58.915.

Feynman, R. P., R. B. Leighton, and M. Sands (1964). *Feynman Lectures on Physics*. Addison Wesley.

Feynman, R. P. (1982). "Simulating physics with computers." In: *International Journal of Theoretical Physics* 21.6, pp. 467–488. DOI: 10.1007/BF02650179.

Feynman, R. P. (1985). "Quantum Mechanical Computers." In: *Optics News* 11.2, pp. 11–20. DOI: 10.1364/ON.11.2.000011.

Fidkowski, L. and A. Kitaev (2011). "Topological phases of fermions in one dimension." In: *Phys. Rev. B* 83 (7), p. 075103. DOI: 10.1103/PhysRevB.83.075103.

Fisher, M. E. (1966). "Shape of a Self-Avoiding Walk or Polymer Chain." In: *The Journal of Chemical Physics* 44.2, pp. 616–622. DOI: 10.1063/1.1726734. eprint: https://doi.org/10.1063/1.1726734.

Flurin, E., V. V. Ramasesh, S. Hacohen-Gourgy, L. S. Martin, N. Y. Yao, and I. Siddiqi (2017). "Observing Topological Invariants Using Quantum Walks in Superconducting Circuits." In: *Phys. Rev. X* 7 (3), p. 031023. DOI: 10.1103/PhysRevX.7.031023.

Fu, L. and C. L. Kane (2007). "Topological insulators with inversion symmetry." In: *Phys. Rev. B* 76 (4), p. 045302. DOI: 10.1103/PhysRevB.76.045302.

Genske, M., W. Alt, A. Steffen, A. H. Werner, R. F. Werner, D. Meschede, and A. Alberti (2013). "Electric Quantum Walks with Individual Atoms." In: *Phys. Rev. Lett.* 110 (19), p. 190601. DOI: 10.1103/PhysRevLett.110.190601.

Gold, J. I. and M. N. Shadlen (2007). "The Neural Basis of Decision Making." In: *Annual Review of Neuroscience* 30.1. PMID: 17600525, pp. 535–574. DOI: 10.1146/annurev.neuro.29.051605.113038. eprint: https://doi.org/10.1146/annurev.neuro.29.051605.113038.

Grössing, G. and A. Zeilinger (1988). "Quantum Cellular Automata." In: *Complex Syst.* 2.2.

Gudder, S. (1988). *Quantum Probability*. Academic Press Inc.

Harper, R., S. T. Flammia, and J. J. Wallman (2020). "Efficient learning of quantum noise." In: *Nature Physics*. DOI: 10.1038/s41567-020-0992-8.

Hasan, M. Z. and C. L. Kane (2010). "Colloquium: Topological insulators." In: *Rev. Mod. Phys.* 82 (4), pp. 3045–3067. DOI: 10.1103/RevModPhys.82.3045.

Hirsch, F., M. T. Quintino, T. Vértesi, M. F. Pusey, and N. Brunner (2016). "Algorithmic Construction of Local Hidden Variable Models for Entangled Quantum States." In: *Phys. Rev. Lett.* 117 (19), p. 190402. DOI: 10.1103/PhysRevLett.117.190402.

Jia, T., D. Wang, and B. K. Szymanski (2017). "Quantifying patterns of research-interest evolution." In: *Nature Human Behaviour* 1.4, p. 0078. DOI: 10.1038/s41562-017-0078.

Jozsa, R. and N. Linden (2003). "On the role of entanglement in quantum-computational speed-up." In: *Proceedings of the Royal Society of London. Series A: Mathematical, Physical and Engineering Sciences* 459.2036, pp. 2011–2032. DOI: 10.1098/rspa.2002.1097. eprint: https://royalsocietypublishing.org/doi/pdf/10.1098/rspa.2002.1097.

Karski, M., L. Förster, J.-M. Choi, A. Steffen, W. Alt, D. Meschede, and A. Widera (2009). "Quantum Walk in Position Space with Single Optically Trapped Atoms." In: *Science* 325.5937, pp. 174–177. DOI: 10.1126/science.1174436. eprint: https://science.sciencemag.org/content/325/5937/174.full.pdf.

Katayama, H., N. Hatakenaka, and T. Fujii (2020). "Floquet-engineered quantum walks." In: *Scientific Reports* 10.1, p. 17544. DOI: 10.1038/s41598-020-74418-w.

Keating, J. P., N. Linden, J. C. F. Matthews, and A. Winter (2007). "Localization and its consequences for quantum walk algorithms and quantum communication." In: *Phys. Rev. A* 76 (1), p. 012315. DOI: 10.1103/PhysRevA.76.012315.

Kitaev, A. Y. (2001). "Unpaired Majorana fermions in quantum wires." In: *Phys. Usp.* 44.10S, p. 131.

Kitaev, A. (May 2009). "Periodic table for topological insulators and superconductors." In: *AIP Conf. Proc.* 1134, p. 22. DOI: 10.1063/1.3149495.

Kitagawa, T. (2012). "Topological phenomena in quantum walks: elementary introduction to the physics of topological phases." In: *Quantum Information Processing* 11.5, pp. 1107–1148. DOI: 10.1007/s11128-012-0425-4.

Kitagawa, T., M. A. Broome, A. Fedrizzi, M. S. Rudner, E. Berg, I. Kassal, A. Aspuru-Guzik, E. Demler, and A. G. White (2012). "Observation of topologically protected bound states in photonic quantum walks." In: *Nature Communications* 3.1, p. 882. DOI: 10.1038/ncomms1872.

Kitagawa, T., M. S. Rudner, E. Berg, and E. Demler (2010). "Exploring topological phases with quantum walks." In: *Phys. Rev. A* 82 (3), p. 033429. DOI: 10.1103/PhysRevA.82.033429.

König, M., S. Wiedmann, C. Brüne, A. Roth, H. Buhmann, L. W. Molenkamp, X.-L. Qi, and S.-C. Zhang (2007). "Quantum Spin Hall Insulator State in HgTe Quantum Wells." In: *Science* 318.5851, pp. 766–770. DOI: 10.1126/science.1148047. eprint: https://science.sciencemag.org/content/318/5851/766.full.pdf.

Landau, L. D. (1937). In: *Phys. Z. Sowjetunion* 11, pp. 19–32.

Li, L. and S. Chen (2019). *Advanced Topolog-ical Insulators*. Wiley, New York, 1–43.

Liu, C. (2012). "Asymptotic distributions of quantum walks on the line with two entangled coins." In: *Quantum Information Processing* 11.5, pp. 1193–1205. DOI: 10.1007/s11128-012-0361-3.

Liu, C. and N. Petulante (2009). "One-dimensional quantum random walks with two entangled coins." In: *Phys. Rev. A* 79 (3), p. 032312. DOI: 10.1103/PhysRevA.79.032312.

Lorz, L., E. Meyer-Scott, T. Nitsche, V. Potocek Vaclav, A. Gábris, S. Barkhofen, I. Jex, and C. Silberhorn (2019). "Photonic quantum walks with four-dimensional coins." In: *Phys. Rev. Research* 1 (3), p. 033036. DOI: 10.1103/PhysRevResearch.1.033036.

Lovett, N. B., S. Cooper, M. Everitt, M. Trevers, and V. Kendon (2010). "Universal quantum computation using the discrete-time quantum walk." In: *Phys. Rev. A* 81 (4), p. 042330. DOI: 10.1103/PhysRevA.81.042330.

Lutchyn, R. M., J. D. Sau, and S. Das Sarma (Aug. 2010). "Majorana Fermions and a Topological Phase Transition in Semiconductor-Superconductor Heterostructures." In: *Phys. Rev. Lett.* 105 (7), p. 077001. DOI: 10.1103/PhysRevLett.105.077001.

Magniez, F., M. Santha, and M. Szegedy (May 2007). "Quantum Algorithms for the Triangle Problem." In: *SIAM J. Comput.* 37.2, 413–424. DOI: 10.1137/050643684.

Mohseni, M., P. Rebentrost, S. Lloyd, and A. Aspuru-Guzik (2008). "Environment-assisted quantum walks in photosynthetic energy transfer." In: *The Journal of Chemical Physics* 129.17, p. 174106. DOI: 10.1063/1.3002335.

Molignini, P., W. Chen, and R. Chitra (2018). "Universal quantum criticality in static and Floquet-Majorana chains." In: *Phys. Rev. B* 98 (12), p. 125129. DOI: 10.1103/PhysRevB.98.125129.

Molignini, P., R. Chitra, and W. Chen (2020). "Unifying topological phase transitions in non-interacting, interacting, and periodically driven systems." In: *EPL (Europhysics Letters)* 128.3, p. 36001. DOI: 10.1209/0295-5075/128/36001.

Muralidharan, S. and P. K. Panigrahi (2008). "Perfect teleportation, quantum-state sharing, and superdense coding through a genuinely entangled five-qubit state." In: *Phys. Rev. A* 77 (3), p. 032321. DOI: 10.1103/PhysRevA.77.032321.

Nayak, A. and A. Vishwanath (2000). "Quantum Walk on the Line." In: *arXiv:quant-ph/0010117*.

Nitsche, T., T. Geib, C. Stahl, L. Lorz, C. Cedzich, S. Barkhofen, R. F. Werner, and C. Silberhorn (2019). "Eigenvalue measurement of topologically protected edge states in split-step quantum walks." In: *New Journal of Physics* 21.4, p. 043031. DOI: 10.1088/1367-2630/ab12fa.

Niu, Q., D. J. Thouless, and Y.-S. Wu (1985). "Quantized Hall conductance as a topological invariant." In: *Phys. Rev. B* 31 (6), pp. 3372–3377. DOI: 10.1103/PhysRevB.31.3372.

Obuse, H., J. K. Asbóth, Y. Nishimura, and N. Kawakami (2015). "Unveiling hidden topological phases of a one-dimensional Hadamard quantum walk." In: *Phys. Rev. B* 92 (4), p. 045424. DOI: 10.1103/PhysRevB.92.045424.

Okugawa, R. and S. Murakami (2014). "Dispersion of Fermi arcs in Weyl semimetals and their evolutions to Dirac cones." In: *Phys. Rev. B* 89 (23), p. 235315. DOI: 10.1103/PhysRevB.89.235315.

Panahiyan, S., W. Chen, and S. Fritzsche (2020). "Fidelity susceptibility near topological phase transitions in quantum walks." In: *Phys. Rev. B* 102 (13), p. 134111. DOI: 10.1103/PhysRevB.102.134111.

Panahiyan, S and S Fritzsche (2018). "Controlling quantum random walk with a step-dependent coin." In: *New Journal of Physics* 20.8, p. 083028. DOI: 10.1088/1367-2630/aad899.

Panahiyan, S. and S. Fritzsche (2019). "Simulation of the multiphase configuration and phase transitions with quantum walks utilizing a step-dependent coin." In: *Phys. Rev. A* 100 (6), p. 062115. DOI: 10.1103/PhysRevA.100.062115.

Panahiyan, S. and S. Fritzsche (2020a). "Controllable simulation of topological phases and edge states with quantum walk." In: *Physics Letters A* 384.32, p. 126828. DOI: https://doi.org/10.1016/j.physleta.2020.126828.

Panahiyan, S. and S. Fritzsche (2020b). "One-dimensional quantum walks driven by two-entangled-qubit coins." In: *Physics Letters A* 384.26, p. 126673. DOI: https://doi.org/10.1016/j.physleta.2020.126673.

Panahiyan, S. and S. Fritzsche (2020c). "Simulation of novel cell-like topological structures with quantum walk." In: *The European Physical Journal Plus* 135.8, p. 626. DOI: 10.1140/epjp/s13360-020-00641-z.

Panahiyan, S. and S. Fritzsche (2021). "Toward simulation of topological phenomena with one-, two-, and three-dimensional quantum walks." In: *Phys. Rev. A* 103 (1), p. 012201. DOI: 10.1103/PhysRevA.103.012201.

Paparo, G. D. and M. A. Martin-Delgado (2012). "Google in a Quantum Network." In: *Scientific Reports* 2.1, p. 444. DOI: 10.1038/srep00444.

Pires, M. A. and S. M. D. Queirós (2020). "Parrondo's paradox in quantum walks with time-dependent coin operators." In: *Phys. Rev. E* 102 (4), p. 042124. DOI: 10.1103/PhysRevE.102.042124.

Qi, X.-L., T. L. Hughes, and S.-C. Zhang (2008). "Topological field theory of time-reversal invariant insulators." In: *Phys. Rev. B* 78 (19), p. 195424. DOI: 10.1103/PhysRevB.78.195424.

Rafi-Ul-Islam, S. M., Z. B. Siu, C. Sun, and M. B. A. Jalil (2020). "Realization of Weyl semimetal phases in topoelectrical circuits." In: *New Journal of Physics* 22.2, p. 023025. DOI: 10.1088/1367-2630/ab6eaf.

Rakovszky, T. and J. K. Asboth (2015). "Localization, delocalization, and topological phase transitions in the one-dimensional split-step quantum walk." In: *Phys. Rev. A* 92 (5), p. 052311. DOI: 10.1103/PhysRevA.92.052311.

Ramasesh, V. V., E. Flurin, M. Rudner, I. Siddiqi, and N. Y. Yao (2017). "Direct Probe of Topological Invariants Using Bloch Oscillating Quantum Walks." In: *Phys. Rev. Lett.* 118 (13), p. 130501. DOI: 10.1103/PhysRevLett.118.130501.

Richter, P. (2007). "Almost uniform sampling via quantum walks." In: *New Journal of Physics* 9.3, pp. 72–72. DOI: 10.1088/1367-2630/9/3/072.

Rohde, P. P., J. F. Fitzsimons, and A. Gilchrist (2012). "Quantum Walks with Encrypted Data." In: *Phys. Rev. Lett.* 109 (15), p. 150501. DOI: 10.1103/PhysRevLett.109.150501.

Ryu, S., A. P. Schnyder, A. Furusaki, and A. W. W. Ludwig (2010). "Topological insulators and superconductors: tenfold way and dimensional hierarchy." In: *New Journal of Physics* 12.6, p. 065010. DOI: 10.1088/1367-2630/12/6/065010.

Sajid, M., J. K. Asbóth, D. Meschede, R. F. Werner, and A. Alberti (2019). "Creating anomalous Floquet Chern insulators with magnetic quantum walks." In: *Phys. Rev. B* 99 (21), p. 214303. DOI: 10.1103/PhysRevB.99.214303.

Schmitz, H., R. Matjeschk, C. Schneider, J. Glueckert, M. Enderlein, T. Huber, and T. Schaetz (2009). "Quantum Walk of a Trapped Ion in Phase Space." In: *Phys. Rev. Lett.* 103 (9), p. 090504. DOI: 10.1103/PhysRevLett.103.090504.

Schnyder, A. P. and S. Ryu (2011). "Topological phases and surface flat bands in superconductors without inversion symmetry." In: *Phys. Rev. B* 84 (6), p. 060504. DOI: 10.1103/PhysRevB.84.060504.

Schnyder, A. P., S. Ryu, A. Furusaki, and A. W. W. Ludwig (Nov. 2008). "Classification of topological insulators and superconductors in three spatial dimensions." In: *Phys. Rev. B* 78 (19), p. 195125. DOI: 10.1103/PhysRevB.78.195125.

Schreiber, A., K. N. Cassemiro, V. Potoceck, A. Gábris, P. J. Mosley, E. Andersson, I. Jex, and C. Silberhorn (2010). "Photons Walking the Line: A Quantum Walk with Adjustable Coin Operations." In: *Phys. Rev. Lett.* 104 (5), p. 050502. DOI: 10.1103/PhysRevLett.104.050502.

Shannon, C. E. (1948). "A Mathematical Theory of Communication." In: *Bell System Technical Journal* 27.3, pp. 379–423. DOI: 10.1002/j.1538-7305.1948.tb01338.x. eprint: https://onlinelibrary.wiley.com/doi/pdf/10.1002/j.1538-7305.1948.tb01338.x.

Shenvi, N., J. Kempe, and K. B. Whaley (2003). "Quantum random-walk search algorithm." In: *Phys. Rev. A* 67 (5), p. 052307. DOI: 10.1103/PhysRevA.67.052307.

Shor, P. W. (Oct. 1997). "Polynomial-Time Algorithms for Prime Factorization and Discrete Logarithms on a Quantum Computer." In: *SIAM J. Comput.* 26.5, 1484–1509. DOI: 10.1137/S0097539795293172.

Su, W. P., J. R. Schrieffer, and A. J. Heeger (1979). "Solitons in Polyacetylene." In: *Phys. Rev. Lett.* 42 (25), pp. 1698–1701. DOI: 10.1103/PhysRevLett.42.1698.

Tarasinski, B., J. K. Asbóth, and J. P. Dahlhaus (2014). "Scattering theory of topological phases in discrete-time quantum walks." In: *Phys. Rev. A* 89 (4), p. 042327. DOI: 10.1103/PhysRevA.89.042327.

Thakurathi, M., A. A. Patel, D. Sen, and A. Dutta (2013). "Floquet generation of Majorana end modes and topological invariants." In: *Phys. Rev. B* 88 (15), p. 155133. DOI: 10.1103/PhysRevB.88.155133.

Thouless, D. J., M. Kohmoto, M. P. Nightingale, and M. den Nijs (Aug. 1982). "Quantized Hall Conductance in a Two-Dimensional Periodic Potential." In: *Phys. Rev. Lett.* 49 (6), pp. 405–408. DOI: 10.1103/PhysRevLett.49.405.

Tsui, D. C., H. L. Stormer, and A. C. Gossard (1982). "Two-Dimensional Magnetotransport in the Extreme Quantum Limit." In: *Phys. Rev. Lett.* 48 (22), pp. 1559–1562. DOI: 10.1103/PhysRevLett.48.1559.

Vakulchyk, I., M. V. Fistul, and S. Flach (2019). "Wave Packet Spreading with Disordered Nonlinear Discrete-Time Quantum Walks." In: *Phys. Rev. Lett.* 122 (4), p. 040501. DOI: 10.1103/PhysRevLett.122.040501.

Venegas-Andraca, S. E. (2012). "Quantum walks: a comprehensive review." In: *Quantum Information Processing* 11.5, pp. 1015–1106. DOI: 10.1007/s11128-012-0432-5.

Viswanathan, G. M., S. V. Buldyrev, S. Havlin, M. G. E. da Luz, E. P. Raposo, and H. E. Stanley (1999). "Optimizing the success of random searches." In: *Nature* 401.6756, pp. 911–914. DOI: 10.1038/44831.

Wang, X., L. Xiao, X. Qiu, K. Wang, W. Yi, and P. Xue (2018). "Detecting topological invariants and revealing topological phase transitions in discrete-time photonic quantum walks." In: *Phys. Rev. A* 98 (1), p. 013835. DOI: 10.1103/PhysRevA.98.013835.

Weng, H., C. Fang, Z. Fang, B. A. Bernevig, and X. Dai (2015). "Weyl Semimetal Phase in Noncentrosymmetric Transition-Metal Monophosphides." In: *Phys. Rev. X* 5 (1), p. 011029. DOI: 10.1103/PhysRevX.5.011029.

Xu, X.-Y., Q.-Q. Wang, M. Heyl, J. C. Budich, W.-W. Pan, Z. Chen, M. Jan, K. Sun, J.-S. Xu, Y.-J. Han, C.-F. Li, and G.-C. Guo (2020). "Measuring a dynamical topological order parameter in quantum walks." In: *Light: Science & Applications* 9.1, p. 7. DOI: 10.1038/s41377-019-0237-8.

Xue, P., R. Zhang, H. Qin, X. Zhan, Z. H. Bian, J. Li, and B. C. Sanders (2015). "Experimental Quantum-Walk Revival with a Time-Dependent Coin." In: *Phys. Rev. Lett.* 114 (14), p. 140502. DOI: 10.1103/PhysRevLett.114.140502.

Yokomizo, K. and S. Murakami (2017). "Topological phases in a Weyl semimetal multilayer." In: *Phys. Rev. B* 95 (15), p. 155101. DOI: 10.1103/PhysRevB.95.155101.

Zähringer, F., G. Kirchmair, R. Gerritsma, E. Solano, R. Blatt, and C. F. Roos (2010). "Realization of a Quantum Walk with One and Two Trapped Ions." In: *Phys. Rev. Lett.* 104 (10), p. 100503. DOI: 10.1103/PhysRevLett.104.100503.

Zhan, X., L. Xiao, Z. Bian, K. Wang, X. Qiu, B. C. Sanders, W. Yi, and P. Xue (2017). "Detecting Topological Invariants in Nonunitary Discrete-Time Quantum Walks." In: *Phys. Rev. Lett.* 119 (13), p. 130501. DOI: 10.1103/PhysRevLett.119.130501.

Zhang, L., L. Zhang, S. Niu, and X.-J. Liu (2018). "Dynamical classification of topological quantum phases." In: *Science Bulletin* 63.21, pp. 1385 –1391. DOI: https://doi.org/10.1016/j.scib.2018.09.018.

7

APPENDIX

7.1 THE METHOD OF STATIONARY PHASES

In this method, we deal with integrals in the form of

$$I(T) = \int_a^b g(k) e^{iT\phi(k_x)} |k_x\rangle \, dk_x. \tag{7.1}$$

The main goal is to find the leading T dependent terms of expansion of the integral for large T. We assume that T tends to infinity. In this integral, the exponential part would rapidly oscillate as T becomes large. If $g(k)$ is a smooth function of the k, the largely contributing parts to the value of the integral are coming from the regions which have the least rapid oscillation. Such regions are marked by stationary points of $\phi(k)$ ($k = a$ which admits $\phi'(a) = 0$). Therefore, the major contributions are coming from the small intervals around the stationary points. For a $p-1$ order stationary point of a and when $g(a)$ is smooth and non-vanishing, we have

$$I(T) \sim g(a) e^{i(T\phi(a) \pm \pi/2p)} \left(\frac{p!}{T|\phi^p(a)|} \right)^{\frac{1}{p}} \frac{\Gamma(\frac{1}{p})}{p}, \tag{7.2}$$

provided that $\phi'(a) = \phi''(a) = ... = \phi^{p-1}(a) = 0$. The $-\pi/2p$ in argument of the exponential emerges if $\phi^p(a) < 0$ and vice versa for the positive case.

In the context of our quantum walk, we have $\phi(k_x, \alpha) = -(\omega_{k_x} + \alpha k_x)$ in which α is limited to $[-1, 1]$ and the integral would be in form of

$$I(T, \alpha) = \int_{-\pi}^{\pi} g(k) e^{iT\phi(k_x,\alpha)} |k_x\rangle \, \frac{dk_x}{2\pi}, \tag{7.3}$$

where $\alpha = \frac{x}{T}$. The asymptotic behavior of this integral depends on the value of the α and can be divided into three distinct behaviors: I) If $|\alpha| > \frac{1}{\sqrt{2}} + O(T^{-\frac{2}{3}})$, the integral decays faster for any inverse polynomial in T. II) Around $\alpha = \pm\frac{1}{\sqrt{2}}$ and with the

order of $O(T^{-\frac{2}{3}})$, the decay would be at the rate of $\frac{1}{\sqrt[3]{T}}$. III) Finally for $|\alpha| < \frac{1}{\sqrt{2}}$, the integral goes as $\frac{1}{\sqrt{T}}$. For our quantum walk, we have

$$\phi' = -\frac{\cos(k_x)}{\sqrt{1+\cos^2(k_x)}} - \alpha, \tag{7.4}$$

$$\phi'' = \frac{\sin(k_x)}{\sqrt{(1+\cos^2(k_x))^3}}, \tag{7.5}$$

$$\phi''' = \frac{2\cos(k_x)(1+\sin^2(k_x))}{\sqrt{(1+\cos^2(k_x))^5}}. \tag{7.6}$$

For $|\alpha| > \frac{1}{\sqrt{2}}$, the obtained relations in Eqs. (7.5) (7.6) are without any root, hence there is no stationary point in this region. Using the method of the integration by part, one can show that $I(T,\alpha)$ is zero in this region. In case of $|\alpha| = \frac{1}{\sqrt{2}}$ though, for $k = 0$ and π, ϕ'' would vanish which indicates the presence of two stationary points. Using Eq. (7.2), we can find

$$I(T,\frac{1}{\sqrt{2}}) \sim g(0)\sqrt{\frac{3}{2}}\frac{\Gamma(\frac{1}{3})}{6\pi}\sqrt[3]{\frac{6}{T}}, \tag{7.7}$$

$$I(T,-\frac{1}{\sqrt{2}}) \sim g(\pi)\sqrt{2}\frac{\Gamma(\frac{1}{3})}{3\pi}\sqrt[3]{\frac{6}{T}}\cos(\frac{\pi}{6}+\frac{\pi}{\sqrt{2}T}). \tag{7.8}$$

Finally, for the region of $-\frac{1}{\sqrt{2}} < \alpha < \frac{1}{\sqrt{2}}$, we have two stationary points of the first order at

$$k = \pm\arccos(-\frac{\alpha}{\sqrt{1-\alpha^2}}) \equiv k_\alpha, \tag{7.9}$$

which by using it alongside the method of the stationary phase gives us

$$I(T,\alpha) \sim \begin{cases} \frac{2g(k_\alpha,\alpha)\cos(\phi(k_\alpha,\alpha)T+\frac{\pi}{4})}{\sqrt{2\pi T|\omega''_{k_\alpha}|}} & \text{for even } g(k_\alpha,\alpha) \\ \\ \frac{2ig(k_\alpha,\alpha)\sin(\phi(k_\alpha,\alpha)T+\frac{\pi}{4})}{\sqrt{2\pi T|\omega''_{k_\alpha}|}} & \text{for odd } g(k_\alpha,\alpha) \end{cases}. \tag{7.10}$$

Now, we are in a position to find the two amplitudes of $\psi_\uparrow(x,T)$ and $\psi_\downarrow(x,T)$ using the above analysis which results into Eqs. (3.23) and (3.24).

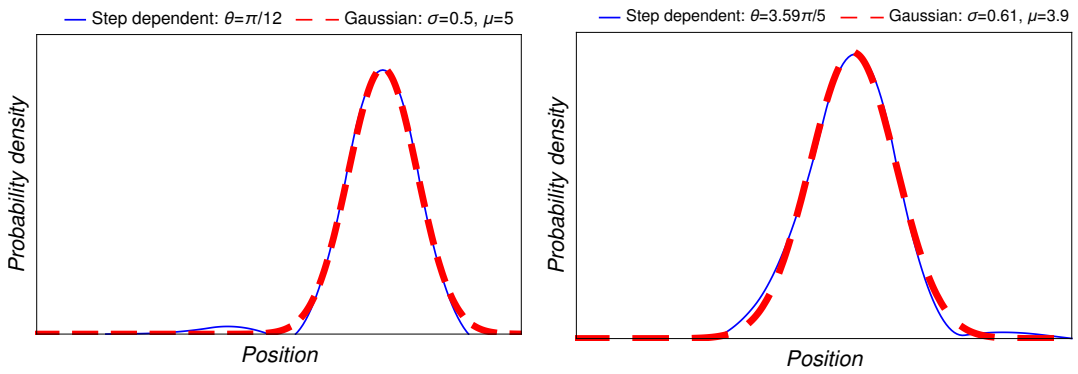

Figure 7.1: Probability density distributions of the Normal distributions and the quantum walks with step-dependent coins for 6th step.

7.2 JUSTIFICATION FOR CLASSIFICATION OF QUANTUM WALKS WITH STEP-DEPENDENT COINS

The two categorizations of classical-like and semi classical/quantum-like can be justified through investigations of the normal distribution and a quantum walk in the presence of decoherence, respectively. The general formula for Normal or Gaussian distribution is

$$f(x \mid \mu, \sigma^2) = \frac{e^{-\frac{(x-\mu)^2}{2\sigma^2}}}{\sqrt{2\pi\sigma^2}}, \tag{7.11}$$

in which μ is the expectation of the distribution, σ is the standard deviation, and σ^2 is the variance. The classical-like behaviors was divided into two sub-classes of compact and usual classical-likes. Therefore, we focus on $T = 6$ for two cases of $\theta = \pi/2$ and $3.59\pi/5$ and fit the Normal distribution to their probability density distributions (see Fig. 7.1).

We use the number of positions occupied by the wave function and their probability densities as means to achieve the fitting. In Fig. 7.1, we show that by tuning the parameters of the Eq. (7.11), one can match the probability density distributions of the compact and usual classical-likes with their corresponding Gaussian ones. The variance of the fitted Gaussian distribution for $\theta = \pi/12$ confirms that indeed we have a more compact distribution comparing to the case with $3.59\pi/5$. This provides us with justification for the classical-like classification. It should be noted that though we have done the fitting for $T = 6$, one can do so for an arbitrary number of steps with proper tuning of the parameters of Normal distribution.

To justify the semi classical/quantum-like classification, we match the probability density distributions of this class with those observed for quantum walks in the presence of decoherence. The amount of decoherence in the quantum walk determines

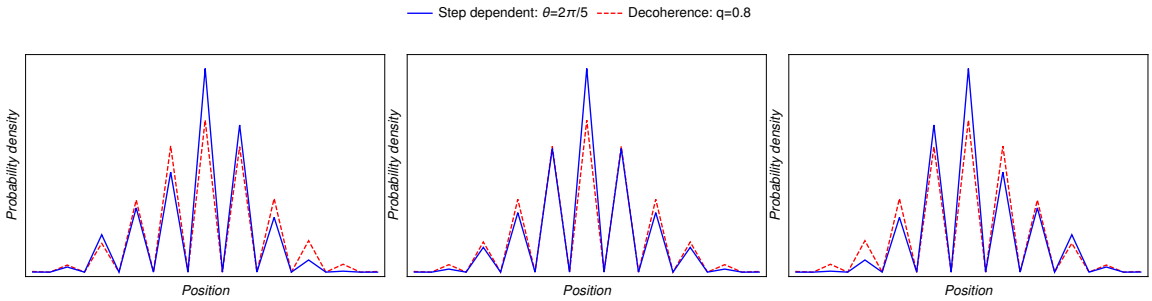

Figure 7.2: Probability density distributions of the quantum walks with step-dependent coins and the decoherent walks for 10th step; left panel $|\phi\rangle_{int} = |\uparrow\rangle \otimes |0\rangle$, middle panel $|\phi\rangle_{int} = (|\uparrow\rangle + I\,|\downarrow\rangle) \otimes \frac{|0\rangle}{\sqrt{2}}$, and right panel with $|\phi\rangle_{int} = |\downarrow\rangle \otimes |0\rangle$.

the behavior of the walker ranging from purely quantum- to classical-like. To include the decoherence, one can perform measurements in the coin and/or position space after each step. Since the system is no longer unitary and pure, we use the density operator for the evolution of the walk in each step

$$\hat{\rho}(T+1) \quad = \quad (1-q-s)\hat{U}\hat{\rho}(T)\hat{U}^{\dagger} + q\mathbb{P}_C\hat{U}\hat{\rho}(t)\hat{U}^{\dagger}\mathbb{P}_C^{\dagger} \quad + s\mathbb{P}_P\hat{U}\hat{\rho}(T)\hat{U}^{\dagger}\mathbb{P}_P^{\dagger}, \qquad (7.12)$$

in which $\mathbb{P}_C$ and $\mathbb{P}_P$ are projections to coin and position spaces, respectively while q and s are the probabilities of a decoherence event happening per time step. We consider $s = 0$. The value of the decoherence parameter is within $0 \leqslant q \leqslant 1$, where $q = 0$ and $q = 1$ correspond to quantum and classical-like behaviors, respectively. We limit our fitting to $T = 10$ while the same can be done for other steps as well. We consider three different initial states in which two of them have only one internal state in themselves while the other one has a superposition of the internal states.

The results in Fig. 7.2 show that the semi classical/quantum-like behavior observed in quantum walks step-dependent coins can be fitted with those observed for the quantum walks in the presence of decoherence with step-independent coins. To prove this also mathematically, we use fidelity which measures how similar two distributions are

$$F(P,Q) \quad = \quad (\sum_i \sqrt{P_i Q_i})^2, \qquad (7.13)$$

where P_i and Q_i are the probability densities of the position i for the quantum walk with step-dependent coin and decoherent ones, respectively. $F(P,Q)$ lies within $[-0,1]$ in which $F(P,Q) = 1$ indicates identical distributions. Our fitting shows that the fidelity is up to 0.97 which shows very good matching and since $q < 1$, we have semi classical/quantum-like walks. Therefore, our classification is justified.

7.3 GROUP VELOCITY AND $\mathbf{d}$ OF THREE-DIMENSIONAL PROTOCOLS

For three-dimensional BDI class, the components of $\mathbf{d}$ are calculated as

$$\begin{aligned}
d_x &= \lambda_\beta[\kappa_\alpha\kappa_\gamma\sin(k_x+k_y+k_z)-\lambda_\alpha\lambda_\gamma\sin(k_x-k_y+k_z)]-\\
&\quad \kappa_\beta[\lambda_\alpha\kappa_\gamma\sin(k_x-k_y-k_z)+\kappa_\alpha\lambda_\gamma\sin(k_x+k_y-k_z)],\\
d_y &= \lambda_\beta[\lambda_\alpha\lambda_\gamma\cos(k_x-k_y+k_z)-\kappa_\alpha\kappa_\gamma\cos(k_x+k_y+k_z)]-\\
&\quad \kappa_\beta[\lambda_\alpha\kappa_\gamma\cos(k_x-k_y-k_z)+\kappa_\alpha\lambda_\gamma\cos(k_x+k_y-k_z)],\\
d_z &= \lambda_\gamma[\lambda_\alpha\kappa_\beta\sin(k_x-k_y+k_z)-\kappa_\alpha\lambda_\beta\sin(k_x+k_y-k_z)]-\\
&\quad \kappa_\gamma[\lambda_\alpha\lambda_\beta\sin(k_x-k_y-k_z)+\kappa_\alpha\kappa_\beta\sin(k_x+k_y+k_z)],
\end{aligned} \tag{7.14}$$

and the components of the group velocity are found as

$$\begin{aligned}
V(k_i) &= \pm\sin(E)^{-1}\Big(A_i^1\kappa_\gamma\lambda_\alpha\lambda_\beta\sin(k_x-k_y-k_z)+A_i^2\kappa_\alpha\lambda_\gamma\lambda_\beta\sin(k_x+k_y-k_z)\\
&\quad +A_i^3\kappa_\beta\lambda_\gamma\lambda_\alpha\sin(k_x-k_y+k_z)+A_i^4\kappa_\alpha\kappa_\gamma\kappa_\beta\sin(k_x+k_y+k_z)\Big),
\end{aligned} \tag{7.15}$$

where $A_x^j=(+1,+1,+1,-1)$, $A_y^j=(-1,-1,-1,+1)$ and $A_z^j=(+1,+1,-1,+1)$.

In case of three-dimensional D class, we find the components of $\mathbf{d}$

$$\begin{aligned}
d_x &= -\kappa_\alpha\kappa_\beta\lambda_\gamma\kappa_\zeta\sin(2k_x)-\kappa_\alpha\kappa_\beta\kappa_\gamma\lambda_\zeta\sin(2k_x+2k_y)+\lambda_\alpha\kappa_\beta\lambda_\gamma\lambda_\zeta\sin(2k_y)\\
&\quad -\kappa_\alpha\lambda_\beta\lambda_\gamma\lambda_\zeta\sin(2k_x+2k_z)+\kappa_\alpha\lambda_\beta\kappa_\gamma\kappa_\zeta\sin(2k_x+2k_y+2k_z)\\
&\quad -\lambda_\alpha\lambda_\beta\lambda_\gamma\kappa_\zeta\sin(2k_y+2k_z)-\lambda_\alpha\lambda_\beta\kappa_\gamma\lambda_\zeta\sin(2k_z),\\
d_y &= \lambda_\alpha\kappa_\beta\kappa_\gamma\kappa_\zeta+\kappa_\alpha\kappa_\beta\lambda_\gamma\kappa_\zeta\cos(2k_x)+\kappa_\alpha\kappa_\beta\kappa_\gamma\lambda_\zeta\cos(2k_x+2k_y)+\\
&\quad \kappa_\alpha\lambda_\beta\kappa_\gamma\kappa_\zeta\cos(2k_x+2k_y+2k_z)-\kappa_\alpha\lambda_\beta\lambda_\gamma\lambda_\zeta\cos(2k_x+2k_z)-\\
&\quad \lambda_\alpha\kappa_\beta\lambda_\gamma\lambda_\zeta\cos(2k_y)-\lambda_\alpha\lambda_\beta\lambda_\gamma\kappa_\zeta\cos(2k_y+2k_z)-\lambda_\alpha\lambda_\beta\kappa_\gamma\lambda_\zeta\cos(2k_z),\\
d_z &= \kappa_\alpha\kappa_\beta\lambda_\gamma\lambda_\zeta\sin(2k_x+2k_z)+\lambda_\alpha\lambda_\beta\lambda_\gamma\lambda_\zeta\sin(2k_y)+\lambda_\alpha\kappa_\beta\kappa_\gamma\lambda_\zeta\sin(2k_z)\\
&\quad +\lambda_\alpha\kappa_\beta\lambda_\gamma\kappa_\zeta\sin(2k_y+2k_z)-\kappa_\alpha\lambda_\beta\kappa_\gamma\lambda_\zeta\sin(2k_x+2k_y)-\\
&\quad -\kappa_\alpha\lambda_\beta\lambda_\gamma\kappa_\zeta\sin(2k_x)-\kappa_\alpha\kappa_\beta\kappa_\gamma\kappa_\zeta(\sin(2k_x+2k_y+2k_z)),
\end{aligned} \tag{7.16}$$

and we obtain the components of group velocity as

$$\begin{aligned}
V(k_x) &= \pm\sin(E)^{-1}2\kappa_\alpha\Big[\lambda_\beta\lambda_\gamma\kappa_\zeta\sin(2k_x)+\lambda_\beta\kappa_\gamma\lambda_\zeta\sin(2k_x+2k_y)\\
&\quad -\kappa_\beta\kappa_\gamma\kappa_\zeta\sin(2k_x+2k_y+2k_z)+\kappa_\beta\lambda_\gamma\lambda_\zeta\sin(2k_x+2k_z)\Big],\\
V(k_y) &= \pm\sin(E)^{-1}2\Big[\kappa_\alpha\lambda_\beta\kappa_\gamma\lambda_\zeta\sin(2k_x+2k_y)-\kappa_\alpha\kappa_\beta\kappa_\gamma\kappa_\zeta\sin(2k_x+2k_y+2k_z)\\
&\quad -\lambda_\alpha\lambda_\beta\lambda_\gamma\lambda_\zeta\sin(2k_y)+\lambda_\alpha\kappa_\beta\lambda_\gamma\kappa_\zeta\sin(2k_y+2k_z)\Big],
\end{aligned}$$

$$V(k_z) = \pm \sin(E)^{-1} 2\kappa_\beta \Big[\kappa_\alpha \lambda_\gamma \lambda_\zeta \sin(2k_x + 2k_z) + \lambda_\alpha \lambda_\gamma \kappa_\zeta \sin(2k_y + 2k_z) + \lambda_\alpha \kappa_\gamma \lambda_\zeta \sin(2k_z) - \kappa_\alpha \kappa_\gamma \kappa_\zeta \sin(2k_x + 2k_y + 2k_z) \Big]. \quad (7.17)$$

As for three-dimensional AIII class, we find the $\mathbf{d}$ and group velocity

$$\begin{aligned}
d_x = {} & [\lambda_\alpha \lambda_\beta \lambda_\gamma - 2\kappa_\alpha \kappa_\beta \lambda_\gamma] \frac{\sin(k_x + k_y - k_z)}{2\sqrt{2}} - [2\lambda_\alpha \kappa_\beta \kappa_\gamma + \lambda_\alpha \lambda_\beta \lambda_\gamma] \frac{\sin(k_x - k_y - k_z)}{2\sqrt{2}} \\
& + [2\kappa_\alpha \lambda_\beta \kappa_\gamma - \lambda_\alpha \lambda_\beta \lambda_\gamma] \frac{\sin(k_x + k_y + k_z)}{2\sqrt{2}} - \frac{\lambda_\alpha \lambda_\beta \lambda_\gamma \sin(k_x - k_y + k_z)}{2\sqrt{2}} \\
& + [\kappa_\alpha \lambda_\beta \lambda_\gamma + \lambda_\alpha \kappa_\beta \lambda_\gamma] \frac{\cos(k_x + k_y - k_z)}{2} + [\lambda_\alpha \lambda_\beta \kappa_\gamma - \lambda_\alpha \kappa_\beta \lambda_\gamma] \frac{\cos(k_x - k_y - k_z)}{2} \\
& - [\lambda_\alpha \lambda_\beta \kappa_\gamma + \frac{1}{2} \kappa_\alpha \lambda_\beta \lambda_\gamma] \frac{\cos(k_x + k_y + k_z)}{2}, \\
d_y = {} & [\lambda_\alpha \kappa_\beta \lambda_\gamma + \kappa_\alpha \lambda_\beta \lambda_\gamma] \frac{\sin(k_x + k_y - k_z)}{2} + [\lambda_\alpha \lambda_\beta \kappa_\gamma - \lambda_\alpha \kappa_\beta \lambda_\gamma] \frac{\sin(k_x - k_y - k_z)}{2} \\
& + [\lambda_\alpha \lambda_\beta \kappa_\gamma + \kappa_\alpha \lambda_\beta \lambda_\gamma] \frac{\sin(k_x + k_y + k_z)}{2} + [2\kappa_\alpha \lambda_\beta \kappa_\gamma - \lambda_\alpha \lambda_\beta \lambda_\gamma] \frac{\cos(k_x + k_y + k_z)}{2\sqrt{2}} \\
& + [2\lambda_\alpha \kappa_\beta \kappa_\gamma + \lambda_\alpha \lambda_\beta \lambda_\gamma] \frac{\cos(k_x - k_y - k_z)}{2\sqrt{2}} + [2\kappa_\alpha \kappa_\beta \lambda_\gamma - \lambda_\alpha \lambda_\beta \lambda_\gamma] \frac{\cos(k_x + k_y - k_z)}{2\sqrt{2}} \\
& - \frac{\lambda_\alpha \lambda_\beta \lambda_\gamma \cos(k_x - k_y + k_z)}{2\sqrt{2}}, \\
d_z = {} & \frac{1}{2} \Big[\lambda_\alpha \kappa_\beta \lambda_\gamma \sin(k_x - k_y + k_z) - \lambda_\alpha \lambda_\beta \kappa_\gamma \sin(k_x - k_y - k_z) \\
& - \kappa_\alpha \lambda_\beta \lambda_\gamma \sin(k_x + k_y - k_z) \Big] + \Big[\lambda_\alpha \lambda_\beta \kappa_\gamma + \lambda_\alpha \kappa_\beta \lambda_\gamma + \kappa_\alpha \lambda_\beta \lambda_\gamma - 2\kappa_\alpha \kappa_\beta \kappa_\gamma \Big] \\
& \times \frac{\sin(k_x + k_y + k_z)}{2} + [2\lambda_\alpha \kappa_\beta \kappa_\gamma + 2\kappa_\alpha \lambda_\beta \kappa_\gamma + 2\kappa_\alpha \kappa_\beta \lambda_\gamma - \lambda_\alpha \lambda_\beta \lambda_\gamma] \frac{\cos(k_x + k_y + k_z)}{2\sqrt{2}} \\
& + [\cos(k_x + k_y - k_z) - \cos(k_x - k_y - k_z) - \cos(k_x - k_y + k_z)] \frac{\lambda_\alpha \lambda_\beta \lambda_\gamma}{2\sqrt{2}}, \quad (7.18)
\end{aligned}$$

$$\begin{aligned}
V(k_i) = {} & \pm \sin(E)^{-1} \Big(\frac{1}{2} [A_i^1 \lambda_\alpha \kappa_\beta \lambda_\gamma \sin(k_x - k_y + k_z) + A_i^2 \lambda_\alpha \lambda_\beta \kappa_\gamma \sin(k_x - k_y - k_z) \\
& + A_i^3 \kappa_\alpha \lambda_\beta \lambda_\gamma \sin(k_x + k_y - k_z)] + \Big[\lambda_\alpha \lambda_\beta \kappa_\gamma + \lambda_\alpha \kappa_\beta \lambda_\gamma + \kappa_\alpha \lambda_\beta \lambda_\gamma - 2\kappa_\alpha \kappa_\beta \kappa_\gamma \Big] \\
& \times \frac{\sin(k_x + k_y + k_z)}{2} + \Big[2\lambda_\alpha \kappa_\beta \kappa_\gamma + 2\kappa_\alpha \lambda_\beta \kappa_\gamma + 2\kappa_\alpha \kappa_\beta \lambda_\gamma - \lambda_\alpha \lambda_\beta \lambda_\gamma \Big] \\
& \times \frac{\cos(k_x + k_y + k_z)}{2\sqrt{2}} + \Big[A_i^4 \cos(k_x + k_y - k_z) + A_i^5 \cos(k_x - k_y - k_z) \\
& + A_i^6 \cos(k_x - k_y + k_z) \Big] \frac{\lambda_\alpha \lambda_\beta \lambda_\gamma}{2\sqrt{2}} \Big), \quad (7.19)
\end{aligned}$$

where $A_x^j = (+1,+1,+1,-1,+1,-1)$, $A_y^j = (-1,-1,+1,-1,-1,+1)$ and $A_z^j = (+1,-1,-1,+1,-1,-1)$.

Finally, for three-dimensional A class, the components of $\mathbf{d}$ and $V(k_i)$ are found as

$$
\begin{aligned}
d_x &= \kappa_\alpha\lambda_\beta\kappa_\gamma\kappa_\zeta\sin(2k_x+2k_y+2k_z)-\frac{\lambda_\alpha\lambda_\beta\kappa_\gamma\kappa_\zeta\cos(2k_x+2k_y+2k_z)}{\sqrt{2}}\\
&-\kappa_\alpha\kappa_\beta\kappa_\gamma\lambda_\zeta\sin(2k_x+2k_y)+\frac{\lambda_\alpha\lambda_\beta\lambda_\gamma}{\sqrt{2}}[\lambda_\zeta\cos(2k_x+2k_z)-\kappa_\zeta\sin(2k_y+2k_z)]\\
&-\kappa_\alpha\lambda_\beta\lambda_\gamma\lambda_\zeta\sin(2k_x+2k_z)-\kappa_\alpha\kappa_\beta\lambda_\gamma\kappa_\zeta\sin(2k_x)+\frac{\lambda_\alpha}{\sqrt{2}}[\kappa_\beta\lambda_\gamma\kappa_\zeta\cos(2k_x)\\
&+\kappa_\beta\lambda_\gamma\lambda_\zeta\sin(2k_y)-\lambda_\beta\kappa_\gamma\lambda_\zeta\sin(2k_z)+\kappa_\beta\kappa_\gamma\lambda_\zeta\cos(2k_x+2k_y)],\\
d_y &= \frac{\lambda_\alpha\lambda_\beta\kappa_\gamma\kappa_\zeta\sin(2k_x+2k_y+2k_z)}{\sqrt{2}}+\kappa_\alpha\lambda_\beta\kappa_\gamma\kappa_\zeta\cos(2k_x+2k_y+2k_z)+\frac{\lambda_\alpha\kappa_\beta\kappa_\gamma\kappa_\zeta}{\sqrt{2}}\\
&+\kappa_\alpha\kappa_\beta\lambda_\gamma\kappa_\zeta\cos(2k_x)-\frac{\lambda_\alpha\lambda_\beta\lambda_\gamma}{\sqrt{2}}[\lambda_\zeta\sin(2k_x+2k_z)+\kappa_\zeta\cos(2k_y+2k_z)]\\
&+\kappa_\alpha\kappa_\beta\kappa_\gamma\lambda_\zeta\cos(2k_x+2k_y)-\kappa_\alpha\lambda_\beta\lambda_\gamma\lambda_\zeta\cos(2k_x+2k_z)+\frac{\lambda_\alpha}{\sqrt{2}}\Big[\kappa_\beta\lambda_\gamma\kappa_\zeta\sin(2k_x)\\
&+\kappa_\beta\kappa_\gamma\lambda_\zeta\sin(2k_x+2k_y)-\kappa_\beta\lambda_\gamma\lambda_\zeta\cos(2k_y)-\lambda_\beta\kappa_\gamma\lambda_\zeta\cos(2k_z)\Big],\\
d_z &= \frac{\lambda_\alpha\kappa_\beta\kappa_\gamma\kappa_\zeta\cos(2k_x+2k_y+2k_z)}{\sqrt{2}}-\kappa_\alpha\kappa_\beta\kappa_\gamma\kappa_\zeta\sin(2k_x+2k_y+2k_z)+\Big[\kappa_\zeta\cos(2k_x)\\
&+\lambda_\zeta\sin(2k_y)\Big]\frac{\lambda_\alpha\lambda_\beta\lambda_\gamma}{\sqrt{2}}+\kappa_\alpha\kappa_\beta\lambda_\gamma\lambda_\zeta\sin(2k_x+2k_z)-\kappa_\alpha\lambda_\beta\lambda_\gamma\kappa_\zeta\sin(2k_x)\\
&-\kappa_\alpha\lambda_\beta\kappa_\gamma\lambda_\zeta\sin(2k_x+2k_y)+\frac{\lambda_\alpha}{\sqrt{2}}\Big[\lambda_\beta\kappa_\gamma\lambda_\zeta\cos(2k_x+2k_y)+\kappa_\beta\kappa_\gamma\lambda_\zeta\sin(2k_z)\\
&+\kappa_\beta\lambda_\gamma\kappa_\zeta\sin(2k_y+2k_z)-\kappa_\beta\lambda_\gamma\lambda_\zeta\cos(2k_x+2k_z)\Big],
\end{aligned}
\tag{7.20}
$$

$$
\begin{aligned}
V(k_x) &= \pm\sin(E)^{-1}\Big(2\kappa_\alpha\lambda_\beta\lambda_\gamma\kappa_\zeta\sin(2k_x)-\sqrt{2}\lambda_\alpha\lambda_\beta\lambda_\gamma\kappa_\zeta\cos(2k_x)\\
&+2\kappa_\alpha\lambda_\beta\kappa_\gamma\lambda_\zeta\sin(2k_x+2k_y)-\sqrt{2}\lambda_\alpha\lambda_\beta\kappa_\gamma\lambda_\zeta\cos(2k_x+2k_y)\\
&+\sqrt{2}\lambda_\alpha\kappa_\beta\kappa_\gamma\kappa_\zeta\cos(2k_x+2k_y+2k_z)-2\kappa_\alpha\kappa_\beta\kappa_\gamma\kappa_\zeta\sin(2k_x+2k_y+2k_z)+\\
&+2\kappa_\alpha\kappa_\beta\lambda_\gamma\lambda_\zeta\sin(2k_x+2k_z)-\sqrt{2}\lambda_\alpha\kappa_\beta\lambda_\gamma\lambda_\zeta\cos(2k_x+2k_z)\Big),\\
V(k_y) &= \pm\sin(E)^{-1}\Big(2\kappa_\alpha\lambda_\beta\kappa_\gamma\lambda_\zeta\sin(2k_x+2k_y)-\sqrt{2}\lambda_\alpha\lambda_\beta\kappa_\gamma\lambda_\zeta\cos(2k_x+2k_y)+\\
&\sqrt{2}\lambda_\alpha\kappa_\beta\kappa_\gamma\kappa_\zeta\cos(2k_x+2k_y+2k_z)-2\kappa_\alpha\kappa_\beta\kappa_\gamma\kappa_\zeta\sin(2k_x+2k_y+2k_z)-\\
&\sqrt{2}\lambda_\alpha\lambda_\beta\lambda_\gamma\lambda_\zeta\sin(2k_y)+\sqrt{2}\lambda_\alpha\kappa_\beta\lambda_\gamma\kappa_\zeta\sin(2k_y+2k_z)\Big),\\
V(k_z) &= \pm\sin(E)^{-1}\Big(\sqrt{2}\lambda_\alpha\kappa_\beta\kappa_\gamma\kappa_\zeta\cos(2k_x+2k_y+2k_z)+2\kappa_\alpha\kappa_\beta\lambda_\gamma\lambda_\zeta\sin(2k_x+2k_z)\\
&-2\kappa_\alpha\kappa_\beta\kappa_\gamma\kappa_\zeta\sin(2k_x+2k_y+2k_z)-\sqrt{2}\lambda_\alpha\kappa_\beta\lambda_\gamma\lambda_\zeta\cos(2k_x+2k_z)+\\
&\sqrt{2}\lambda_\alpha\kappa_\beta\lambda_\gamma\kappa_\zeta\sin(2k_y+2k_z)+\sqrt{2}\lambda_\alpha\kappa_\beta\kappa_\gamma\lambda_\zeta\sin(2k_z)\Big).
\end{aligned}
\tag{7.21}
$$

7.4 ANALYTICAL DESCRIPTION FOR QUANTUM WALKS WITH ENTANGLED QUBITS

For the quantum walk with two entangled qubits, we can rewrite its wave function at step T as $\left|\psi_j\right\rangle_{Fin} \equiv \Psi_T(x) = [\phi_T(x,1), \phi_T(x,2), \phi_T(x,3), \phi_T(x,4)]^t$ in which the four components correspond to the coin states $|\uparrow\uparrow\rangle$, $|\downarrow\downarrow\rangle$, $|\downarrow\uparrow\rangle$ and $|\uparrow\downarrow\rangle$. This indicates that initial state of the walker is $\Psi_0(0) = [\phi_0(0,1), \phi_0(0,2), \phi_0(0,3), \phi_0(0,4)]^t \equiv [\beta_1, \beta_2, \beta_3, \beta_4]^t$ where $\sum_{z=1}^{4} |\beta_z| = 1$.

The discrete Fourier transformation of $\Psi_T(x)$ gives us

$$\Psi_T(k) = \sum_{x\in\mathbb{Z}} \Psi_T(x) e^{ikx}, \tag{7.22}$$

which for the initial state, we would have

$$\Psi_0(k) = \Psi_0(0). \tag{7.23}$$

The quantum walk in momentum space is produced by $\Psi_T(k) = \widehat{U}^T(k)\Psi_0(k)$ in which

$$U(k) = \widehat{U}_1(k/2) \otimes \widehat{U}_2(k/2) = \begin{bmatrix} e^{ik/2} & 0 \\ 0 & e^{-ik/2} \end{bmatrix} \widehat{C}_1 \otimes \begin{bmatrix} e^{ik/2} & 0 \\ 0 & e^{-ik/2} \end{bmatrix} \widehat{C}_2. \tag{7.24}$$

In order to invoke the method of the stationary phases, we first find the eigenvalues of $\widehat{U}_1(k/2)$ and $\widehat{U}_2(k/2)$, as

$$\lambda_{1,\pm} = \pm\sqrt{1 - \cos^2\theta \sin^2(\frac{k}{2})} + i\cos\theta\sin(\frac{k}{2}), \tag{7.25}$$

$$\lambda_{2,\pm} = \pm\sqrt{1 - \cos^2\gamma \sin^2(\frac{k}{2})} + i\cos\gamma\sin(\frac{k}{2}), \tag{7.26}$$

which gives us the eigenvalues (Λ_i) and eigenvectors (V_i) of $\widehat{U}(k)$ as

$$\begin{cases} \Lambda_1 = \lambda_{1,+}\lambda_{2,+} \\ \Lambda_2 = \lambda_{1,+}\lambda_{2,-} \\ \Lambda_3 = \lambda_{1,-}\lambda_{2,+} \\ \Lambda_4 = \lambda_{1,-}\lambda_{2,-} \end{cases}, \quad \begin{cases} V_1(k) = \nu_{1,+} \otimes \nu_{2,+} \\ V_2(k) = \nu_{1,+} \otimes \nu_{2,-} \\ V_1(k) = \nu_{1,-} \otimes \nu_{2,+} \\ V_3(k) = \nu_{1,-} \otimes \nu_{2,-} \end{cases}, \tag{7.27}$$

in which $v_{1,\pm}$ and $v_{2,\pm}$ are eigenvectors of $\widehat{U}_1(k/2)$ and $\widehat{U}_1(k/2)$, respectively. This gives us the final state of $\Psi_T(k)$ in the form of

$$\Psi_T(k) = \widehat{U}(k)^T \Psi_0(k) = \sum_{z=1}^{4} \Lambda_z^T \langle V_z(k), \Psi_0(k)\rangle V_z(k). \tag{7.28}$$

Using the inverse Fourier transformation, we bring back the wave function into real spatial space as

$$\Psi_T(x) = \int_0^{2\pi} e^{-ikx} \sum_{z=1}^{4} \Lambda_z^T \langle V_z(k), \Psi_0(k)\rangle V_z(k) \frac{dk}{2\pi}, \tag{7.29}$$

If sub-coins are identical ($\theta = \gamma$) with $\theta \in (0, \pi/2)$, the eigenvalues would reduce to $\Lambda_1 = \lambda_{1,+}^2$, $\Lambda_2 = \Lambda_3 = 1$ and $\Lambda_4 = \lambda_{1,-}^2$. This gives us $\Psi_T(x) =$ as (Liu and Petulante, 2009; Liu, 2012)

$$\Psi_T(x) \approx \int_0^{2\pi} e^{-ikx} (-1)^T \sum_{z=2}^{3} \Lambda_z^T \langle V_z(k), \Psi_0(k)\rangle V_z(k) \frac{dk}{2\pi}, \tag{7.30}$$

One can find the limiting probability of finding the walker at each position as (Liu, 2012)

$$\begin{aligned}
p(0) &= \tan^2\theta \mu_1^2 (|\beta_1|^2 + |\beta_4|^2) + \sec\theta \mu_1 (|\beta_2|^2 + |\beta_3|^2) + \\
&\quad \tan\theta \mu_1^2 Re(\beta_2\bar{\beta}_4 + \beta_3\bar{\beta}_4 - \beta_1\bar{\beta}_2 - \beta_1\bar{\beta}_3) - \\
&\quad 2\tan\theta \mu_1 Re(\beta_2\bar{\beta}_3), \\
p(x)|_{x\geqslant 1} &= \mu_1^{4x} \tan^2\theta [\mu_2^2|\beta_1|^2 + |\beta_2|^2 + |\beta_3|^2 + \mu_1^2|\beta_4|^2 - \\
&\quad 2\mu_2 Re(\beta_1\bar{\beta}_2 + \beta_1\bar{\beta}_3) + 2Re(\beta_1\bar{\beta}_4 + \beta_2\bar{\beta}_3) - \\
&\quad 2\mu_1 Re(\beta_2\bar{\beta}_4 + \beta_3\bar{\beta}_4)], \\
p(x)|_{x\leqslant -1} &= \mu_1^{-4x} \tan^2\theta [\mu_1^2|\beta_1|^2 + |\beta_2|^2 + |\beta_3|^2 + \mu_2^2|\beta_4|^2 + \\
&\quad 2\mu_1 Re(\beta_1\bar{\beta}_2 + \beta_1\bar{\beta}_3) + 2Re(\beta_1\bar{\beta}_4 + \beta_2\bar{\beta}_3) + \\
&\quad 2\mu_2 Re(\beta_2\bar{\beta}_4 + \beta_3\bar{\beta}_4)],
\end{aligned} \tag{7.31}$$

where $\mu_1 = \sec\theta(1 - \sin\theta)$ and $\mu_2 = \sec\theta(1 + \sin\theta)$. In case of $\beta_2 = \beta_3 = 0$, the probability densities will be

$$\begin{aligned}
p(0) &= \tan^2\theta \mu_1^2 (|\beta_1|^2 + |\beta_4|^2), \\
p(x)|_{x\geqslant 1} &= \mu_1^{4x} \tan^2\theta [\mu_2^2|\alpha_1|^2 + \mu_1^2|\alpha_4|^2 + 2Re(\alpha_1\bar{\alpha}_4)], \\
p(x)|_{x\leqslant -1} &= \mu_1^{-4x} \tan^2\theta [\mu_1^2|\alpha_1|^2 + \mu_2^2|\alpha_4|^2 + 2Re(\alpha_1\bar{\alpha}_4)],
\end{aligned} \tag{7.32}$$

which shows that only in case of $|\beta_1|^2 = |\beta_4|^2$, we have $p(x)|_{x\geqslant 1} = p(x)|_{x\leqslant -1}$, hence symmetrical probability density distribution which is in agreement with our earlier results. Considering $\beta_1 = \cos\eta$ and $\beta_4 = e^{I\phi}\sin\eta$, we find that symmetrical probability density distribution is resulted if $\eta = \pi/4$. In case of $\beta_1 = \beta_4 = 0$, we find

$$\begin{aligned} p(0) &= \sec\theta\mu_1(|\beta_2|^2 + |\beta_3|^2) - 2\tan\theta\mu_1 Re(\beta_2\bar{\beta}_3), \\ p(x)|_{x\geqslant 1} &= \mu_1^{4x}\tan^2\theta[|\beta_2|^2 + |\beta_3|^2 + 2Re(\beta_2\bar{\beta}_3)], \\ p(x)|_{x\leqslant -1} &= \mu_1^{-4x}\tan^2\theta[|\beta_2|^2 + |\beta_3|^2 + 2Re(\beta_2\bar{\beta}_3)], \end{aligned} \tag{7.33}$$

which makes the symmetry of the probability density distribution independent of β_2 and β_3. This is in agreement with our findings when $\beta_2 = \cos\alpha$ and $\beta_3 = e^{I\phi}\sin\alpha$.

In the limit of $\theta \to 0$ with $\beta_2 = \beta_3 = 0$, the obtained probability density amplitudes will be

$$\begin{aligned} \lim_{\theta\to 0} p(0) &= O(\beta_1^2, \beta_4^2)\theta^2 - 2O(\beta_1^2, \beta_4^2)\theta^3 + \frac{8}{3}O(\beta_1^2, \beta_4^2)\theta^4 + ..., \\ \lim_{\theta\to 0} p(x)|_{x\geqslant 1} &= O'(\beta_1^2, \beta_4^2)\theta^2 - O''(\beta_1^2, \beta_4^2, x)\theta^3 + O'''(\beta_1^2, \beta_4^2, x^2)\theta^4 + ..., \\ \lim_{\theta\to 0} p(x)|_{x\leqslant -1} &= O'(\beta_1^2, \beta_4^2)\theta^2 + O''(\beta_1^2, \beta_4^2, x)\theta^3 + O'''(\beta_1^2, \beta_4^2, x^2)\theta^4 + ..., \end{aligned} \tag{7.34}$$

where O, O', O'', O''' are different terms containing different orders of β_i and x. Therefore, the probability at the origin almost vanishes while at the right- and left-hand sides positions, due to x as a factor, the probability would be non-zero, hence two peaks at right- and left-hand sides' positions. This is consistent with plotted diagrams in Fig. 5.1 for initial state of (5.6).

As for $\theta \to 0$ with $\beta_1 = \beta_4 = 0$, we have

$$\begin{aligned} \lim_{\theta\to 0} p(0) &= O(\beta_2^2, \beta_3^2) - O'(\beta_2^2, \beta_3^2)\theta + O'(\beta_2^2, \beta_3^2)\theta^2 + ..., \\ \lim_{\theta\to 0} p(x)|_{x\geqslant 1} &= O'(\beta_2^2, \beta_3^2)\theta^2 - O''(\beta_1^2, \beta_4^2, x)\theta^3 + O'''(\beta_1^2, \beta_4^2, x^2)\theta^4 + ..., \\ \lim_{\theta\to 0} p(x)|_{x\leqslant -1} &= O'(\beta_2^2, \beta_3^2)\theta^2 + O''(\beta_1^2, \beta_4^2, x)\theta^3 + O'''(\beta_1^2, \beta_4^2, x^2)\theta^4 + ..., \end{aligned} \tag{7.35}$$

which indicates a peak at the origin and almost zero the probability densities at right- and left-hand sides except for very large (small) positions (x). Therefore, a Three-peaks-zone in probability density distribution would be observed which is in agreement with plotted diagrams in Fig. 5.1 for the initial state of (5.7). The same can be applied to other limits such as $\theta \to \pi/2$ which confirms our numerical simulation.

EHRENWÖRTLICHE ERKLÄRUNG

Ich erkläre hiermit ehrenwörtlich, dass ich die vorliegende Arbeit selbstständing, ohne unzuässige Hilfe dritter und ohne Benutzung anderer als der angegebenen Hilfsmittel und Literatur angefertigt habe. Die aus anderen Quellen direkt oder indirekt übernommenen Daten und Konzepte sind unter Angabe der Quelle gekennzeichnet. Bei der Anfertigung dieser Arbeit haben mir meine Betreuer und die Koautoren oben genannter Publikationen geholfen.
Weitere Personen waren an der inhaltlich-materiellen Erstellung der vorliegenden Arbeit nicht beteiligt. Insbesondere habe ich hierfür nicht die entgeltliche Hilfe von Vermittlungs- bzw. Beratungsdiensten (Promotionsberater oder andere Personen) in Anspruch genommen.
Niemand hat von mir unmittelbar oder mittelbar geldwerte Leistungen für Arbeiten erhalten, die im Zusammenhang mit dem Inhalt der vorgelegten Dissertation stehen.
Die Arbeit wurde bisher weder im In- noch im Ausland in gleicher oder ähnlicher Form einer anderen Prüfungsbehörde vorgelegt. Die geltende Promotionsordnung der Physikalisch-Astronomischen Fakultät ist mir bekannt.
Ich versichere ehrenwörtlich, dass ich nach bestem Wissen die reine Wahrheit gesagt und nichts verschwiegen habe.

Jena,

Shahram Panahiyan